


<https://doi.org/10.15388/vu.thesis.318>
 <https://orcid.org/0000-0002-0599-6885>

VILNIUS UNIVERSITY
CENTER FOR PHYSICAL SCIENCES AND TECHNOLOGY

Giedrius Žlabys

Ultracold atom dynamics in quasi-one-dimensional optical lattices

DOCTORAL DISSERTATION

Natural Sciences,
Physics (N 002)

VILNIUS 2022

This dissertation was written between 2017 and 2021 at the Institute of Theoretical Physics and Astronomy of Vilnius University.

Academic supervisor:

Prof. Dr. Egidijus Anisimovas (Vilnius University, Natural Sciences, Physics, N 002)

Dissertation Defense Panel:

Chairman – Dr. Vidas Regelskis (Vilnius University, Natural Sciences, Physics, N 002)

Members:

Prof. Darius Abramavičius (Vilnius University, Natural Sciences, Physics, N 002)

Prof. Thomas Busch (Okinawa Institute of Science and Technology Graduate University, Natural Sciences, Physics, N 002)

Assoc. Prof. Dr. Andrius Gelžinis (Center for Physical Sciences and Technology, Natural Sciences, Physics, N 002)


Dr. Aleksejus Kononovičius (Vilnius University, Natural Sciences, Physics, N 002)

The dissertation shall be defended at a public meeting of the Dissertation Defense Panel at 10:00 on the 21st of June, 2022, in Room D401 of the Center for Physical Sciences and Technology.

Address: Saulėtekio av. 3, Vilnius, LT-10257, Lithuania.

The text of this dissertation can be accessed at the Vilnius University Library, as well as on the website of Vilnius University:

www.vu.lt/naujienos/ivykiu-kalendorius

<https://doi.org/10.15388/vu.thesis.318>
 <https://orcid.org/0000-0002-0599-6885>

VILNIAUS UNIVERSITETAS
FIZINIŲ IR TECHNOLOGIJOS MOKSLŲ CENTRAS

Giedrius Žlabys

Šaltųjų atomų dinamika kvazivienmatėse optinėse gardelėse

DAKTARO DISERTACIJA

Gamtos mokslai,
Fizika (N 002)

VILNIUS 2022

Disertacija rengta 2017–2021 metais Vilniaus universiteto Teorinės fizikos ir astronomijos institute.

Mokslinis vadovas:

prof. dr. Egidijus Anisimovas (Vilniaus universitetas, gamtos mokslai, fizika, N 002)

Gynimo taryba:

Pirmininkas – dr. Vidas Regelskis (Vilniaus universitetas, gamtos mokslai, fizika, N 002)

Nariai:

prof. Darius Abramavičius (Vilniaus universitetas, gamtos mokslai, fizika, N 002)

prof. Thomas Busch (Okinawa Institute of Science and Technology Graduate University, gamtos mokslai, fizika, N 002)

doc. dr. Andrius Gelžinis (Fizinių ir technologijos mokslų centras, gamtos mokslai, fizika, N 002)

dr. Aleksejus Kononovičius (Vilniaus universitetas, gamtos mokslai, fizika, N 002)

Disertacija ginama viešame Gynimo tarybos posėdyje 2022 m. birželio mėn. 21 d. 10:00 val. Nacionaliniame fizinių ir technologijos mokslų centre D401 auditorijoje. Adresas: Saulėtekio al. 3, Vilnius, LT-10257, Lietuva.

Disertaciją galima peržiūrėti Vilniaus universiteto bibliotekoje ir VU interneto svetainėje adresu: www.vu.lt/naujienos/ivykiu-kalendorius

CONTENTS

CONTENTS	5
INTRODUCTION	7
LIST OF PUBLICATIONS	13
1 MODELING OPTICAL LATTICES	15
1.1 Optical lattices	15
1.1.1 Atom-light interaction	15
1.1.2 Single-particle lattice Hamiltonian	17
1.1.3 Second quantization and the tight-binding approximation	19
1.2 Magnetic flux in a lattice of neutral atoms	22
1.2.1 Gauge field induced flux	22
1.2.2 Tight-binding model with flux	25
1.2.3 Topological properties	26
1.3 Floquet picture	28
2 TIME-SPACE CRYSTALLINE STRUCTURES	30
2.1 Classical analysis of a 1D driven potential	31
2.1.1 Phase space diagram	31
2.1.2 Action-angle picture	33
2.1.3 Classical secular approximation	35
2.2 Quantum analysis of a 1D driven potential	38
2.2.1 Floquet Hamiltonian	38
2.2.2 Time-independent Hamiltonian basis	40
2.2.3 Quantum secular approximation	41
2.2.4 Tight-binding model of a time-space crystal	42
2.2.5 Interactions	44
2.3 Higher dimensional time-space crystalline structures	44
2.4 Case study: driven sine-squared lattice at $s = 3$ resonance	46
2.4.1 Parameter selection	47
2.4.2 Validity of the quantum secular Hamiltonian	49
2.4.3 Quasi-one-dimensional time-space crystalline structure	52
2.4.4 Experimental scheme	55
2.5 Engineering artificial magnetic flux in a time-space lattice	56

2.5.1	Tilted potential in the time domain	57
2.5.2	Wannier functions of a tilted lattice	61
2.5.3	Laser-assisted tunneling	63
2.5.4	Topological properties of time-space crystalline structures	64
2.6	Summary	67
3	LEARNING THE GROUND STATE STRUCTURE WITH ARTIFICIAL NEURAL NETWORKS	68
3.1	Artificial neural network for ground state determination	69
3.1.1	Restricted Boltzmann machine	69
3.1.2	Reinforced learning	71
3.2	Learning ground state features of flat band lattices	73
3.2.1	Sawtooth lattice	74
3.2.2	Learning the density wave	76
3.2.3	Impact of hidden layer size	80
3.2.4	Role of interaction strength	82
3.2.5	Kagome lattice	85
3.2.6	Learning hexagonal density islands	86
3.2.7	Summary	88
3.3	Autoencoder-based ground state fidelity improvement	89
3.3.1	Approximate states via feedforward neural network	89
3.3.2	Feedforward autoencoder	91
3.3.3	Encoding the Bloch sphere	93
3.3.4	Sample set generation with dominant ground state	96
3.3.5	Encoding few-level systems	98
3.3.6	Decoding few-level systems	100
3.3.7	Application: square and sawtooth lattices	102
3.3.8	Summary	104
	CONCLUSIONS	106
	ACKNOWLEDGEMENTS	108
	SANTRAUKA LIETUVIŲ KALBA	109
	BIBLIOGRAPHY	137
	CURRICULUM VITAE	151

INTRODUCTION

Ultracold atom systems are composed of neutral atomic gases that are cooled to tens of microkelvin or even lower temperatures and trapped in an external potential. Exact engineering and control of the external potential allows exploring a large variety of quantum effects while avoiding problems arising from impurities and defects in condensed matter samples.

The advent of the experimental exploration of ultracold atom systems was the creation of Bose-Einstein condensate in 1995 [1,2]. A cloud of atomic gas was trapped in a magnetic trap and slowed down by using novel laser and evaporative cooling techniques to reach this exotic state of matter at extremely low temperatures where the quantum effects dominate. The experiments confirmed the theoretical predictions of Bose and Einstein [3,4] proposed in the early 20th century and paved the way for further research of superfluid states of matter (collective oscillations [5], quantized vortex formation [6], Josephson type effects [7]). In the following years, the condensates of fermions were explored as well: momentum distribution changes due to Pauli exclusion principle were observed in an ultracold gas of ^{40}K atoms in 1999 [8], superfluidity predicted by the Bardeen-Cooper-Schrieffer theory was realized experimentally [9]. An extensive review of Fermi gas experiments and theory can be found in Ref. [10].

A natural step from the study of a cloud of atomic gas is to investigate its behavior when trapped in periodic potentials. Such potentials can be created with the help of optical lattices. Optical lattices are interfering laser beams that form periodic spatial intensity patterns [11]. Atoms placed in the lattice interact with the light field via the electric field-dipole interaction and get trapped in the periodic minima or maxima of the field intensity depending on their polarizability. These light crystals are of particular interest since they can be used as many-body quantum simulators proposed by Feynman in 1982 [12,13]. Adjusting the laser beam configuration allows forming lattices of different geometries while tuning the intensity modifies the tunneling rate of particles between lattice sites and changes the interparticle interactions. The high controllability of the parameters describing the system and purity of the lattices provides the perfect conditions to straightforwardly implement and test theoretical models in experiments. Some prominent examples are Hubbard

type models [14–17] which allow to approximate the behavior of interacting fermions and bosons in a lattice. Fermi-Hubbard model offers insight to high- T_c superconductivity [18, 19] and probes quantum spin models [20]. Bose-Hubbard Hamiltonians can be used to explore quantum phase transitions in Bose gases [21–23]. The universality of optical traps and lattices offers a platform to realize new states of matter such as discrete time crystals [24, 25], phase space crystals [26] and supersolids [27, 28].

Additional complexity can be introduced by considering effects that typically appear in the presence of magnetic fields in condensed matter physics. Atoms trapped in optical lattices are neutral therefore to use these systems as models of lattices affected by magnetic forces some ingenuity is needed. One way to create an artificial magnetic field is to periodically drive the system [29, 30] to create a Coriolis-type force which simulates a gauge field equivalent to a magnetic field. Another way is to imprint a phase to the wavefunction of a particle hopping between the lattice sites through Raman [31, 32] or optical clock [33] transitions. Equipped with the tools necessary to realize an effective magnetic field one can probe quantum Hall effect [34, 35] and explore topological quantum matter [36–38] that is robust to external perturbations. The insight gained about the properties of such systems in a highly controllable environment is an important step towards realizing topological electronic devices [39] and for potential applications in quantum computing [40].

Optical lattices also provide the ability to access higher-dimensional physics by employing the internal degrees of freedom of the system as an additional synthetic dimension [41, 42]. The internal atomic states or spin degrees of freedom of particles composing the trapped gas can be interpreted as an extra spatial dimension. This allows one to look for the quantum Hall effect in four [43, 44] or even six [45] dimensions which is of particular interest when analyzing the topology of quasicrystals [46], time-reversal invariant insulators [47] and other exotic phenomena [48, 49].

The versatility of ultracold atom lattices pushes the boundaries of the numerical tools as well. On one hand, analytical and numerical calculations help to identify the parameter regimes that support interesting phases of matter and guide the experimental setups. On the other hand, the expanding experimental capabilities provide new control variables requiring increasing computational resources to benchmark the observed results. Due to the complexity arising from the interplay of a large number of particles, the analytical approximations have a limited range of validity [50, 51] necessitating the development and improvement of numerical methods [52]. The lowest energy states of small lattices containing few particles are successfully obtained by employing exact diagonalization [53]. For larger systems tensor network [54, 55], quantum Monte Carlo [56] or possibly even neural network methods [57–61] can be applied, although the precise method selection depends on the problem specifics and often

requires novel approaches.

The aim of this thesis is twofold and touches upon both analytical and numerical aspects of the vast field of ultracold atom physics. The first aim is to apply the ideas of discrete time crystals to driven optical lattices and derive effective higher-dimensional systems termed time-space crystalline structures that complement the currently known lattices with synthetic dimensions. The second aim is to numerically explore the application of neural networks to determine the properties of quasi-one-dimensional lattices (several coupled one-dimensional lattices that form a finite width ribbon) and open boundary segments of two-dimensional lattices.

The objective of the thesis

The first goal of this thesis is to propose a lattice model with a synthetic temporal dimension – a time-space crystalline structure which effectively allows probing physics in up to six dimensional lattice models and to show that such a system supports topological properties. To achieve this goal the following tasks are set:

- Analyze the origin of the periodic time domain structure in a single well of a resonantly driven sine-squared potential lattice using the classical Hamiltonian mechanics picture.
- Develop a quantum description that couples the temporal structure at each lattice well with the structures in the neighboring spatial wells to obtain an effective quasi-one-dimensional lattice.
- Generalize the resonantly driven potentials to create a lattice that supports higher dimensions.
- Employ laser-assisted tunneling together with a potential tilt to realize controllable magnetic fluxes piercing the lattice and check for topological properties in the time-space crystalline structure.

The second objective is to investigate an artificial neural network as a numerical tool to obtain the ground states of restricted geometry lattices. The tasks to be done are as follows:

- Choose the architecture of the artificial neural network and its weight optimization algorithm.
- Select the lattice models for the network to learn.
- Analyze the convergence of local and global features that define the density structure of the lattice ground state for various network and lattice model parameters.

- Check how the convergence of characteristic expectation values changes with the scale of the systems.

Practical and scientific novelty

- Time-space crystalline structure is a novel high-dimensional lattice created by utilizing periodic resonant driving of the periodic trapping spatial potentials. It provides an alternative to other proposed models that host synthetic dimensions [41, 42] and supplies a toolbox to probe topological properties such as the formation of localized edge states [62] or Thouless pumping in higher dimensions [45].
- The application of artificial neural networks for ground-state calculations of lattice Hamiltonians is a recently emerging field [57, 63] which offers a method that can potentially complement the typically used exact diagonalization and tensor network algorithms. Although analytical evidence suggests that artificial neural networks can accurately represent many-body states [64], optimizability of the networks is still an open issue – it is unclear if the network will manage to successfully learn the features of a given model. In the thesis we set out to investigate the ability of two distinct neural network architectures to determine or improve the ground-state estimate of restricted geometry lattices. In particular, a lot of attention will be given to flat band models which are interesting due to their flat spectral band highlighting the role of interactions while at the same time posing a reasonable challenge for the networks to overcome. If successfully applied, the neural networks could potentially probe larger systems than possible with other numerical tools.

Statements to be defended

1. A resonantly periodically driven lattice supports a parameter regime which realizes a time-space crystalline lattice – a spatial lattice equipped with periodic temporal structure at each site acting as a synthetic dimension.
2. Time-space crystalline structures offer a platform to probe topological properties in six dimensions.
3. Artificial neural networks with restricted Boltzmann machine architecture successfully encode the global structure of the ground state of dispersionless band lattice models while only guided by the energy minimization.
4. Artificial neural networks are prone to getting stuck at a density configuration corresponding to a local energy minima for large systems.

5. Autoencoder-aided analysis allows one to extract an improved ground-state estimate based on a set of noisy states with dominant ground-state contribution.

Layout of the dissertation

Chapter 1 introduces the main ideas used when modeling the behavior of trapped particles in optical lattices. Section 1.1 describes the physical origin of optical lattice trapping, the Hamiltonian formalism and the second quantization representation of such systems. Section 1.2 elucidates how effective magnetic fields can be engineered in a lattice with neutral particles by exploiting the inherently geometric nature of the effect and gives a short overview of the resulting topological properties. Section 1.3 presents the Floquet formalism which provides a convenient basis to solve time-periodic problems.

Chapter 2 establishes the theoretical description of a time-space crystalline structure. Section 2.1 concentrates on the classical motion of a particle in a periodically resonantly driven one-dimensional sine-squared potential, the emergence of a periodic structure in the stroboscopic phase-space picture of the system and its effective description. Section 2.2 extends the description to encompass the quantum case and develops a two-dimensional time-space crystalline lattice. Section 2.3 generalizes the model to six dimensions in the tight-binding approximation formalism. Section 2.4 gives a concrete example of a quasi-one-dimensional time-space crystalline structure and discusses the conditions required for it to form. Finally, in section 2.5 a scheme to create and control magnetic fluxes in the system is proposed which allows probing topological properties such as formation of topologically protected edge states.

Chapter 3 focuses on the ability of artificial neural networks to calculate the ground state and encode its features for lattice models with finite geometries. Section 3.1 introduces a network with restricted Boltzmann machine structure, the ansatz for the ground state in terms of the network parameters and the learning procedure. The established model is applied in section 3.2 to investigate the convergence of characteristic parameters of a flat band quasi-one-dimensional sawtooth lattice and a finite segment of a kagome lattice. The impact of lattice and network scaling to convergence rate is explored. In section 3.3, a different type of network structure is considered – a feedforward autoencoder, which tackles the problem of improving the ground-state estimate from a noisy set of states. Its encoding/decoding capabilities are analyzed for sample states that have a dominant ground-state contribution and the network is applied to find the improved estimates of ground-state densities of a finite two-dimensional square and sawtooth lattices.

Contribution of the author

The main results of this thesis are based on three publications [A1-A3]. The author contributed by performing analytical and numerical calculations, analyzed the results and together with coauthors prepared the publications [A1-A3].

LIST OF PUBLICATIONS

On the dissertation topic

- [A1] **G. Žlabys**, C.-h. Fan, E. Anisimovas, K. Sacha, Six-dimensional time-space crystalline structures, *Phys. Rev. B* **103**, L100301 (2021).
- [A2] **G. Žlabys**, M. Račiūnas, E. Anisimovas, Learning quantum structures in compact localized eigenstates, *J. Phys. A: Math. Theor.* **53**, 115302 (2020).
- [A3] **G. Žlabys**, M. Račiūnas, E. Anisimovas, Autoencoder-aided analysis of low-dimensional Hilbert spaces, *Lith. J. Phys.* **61**, 205–214 (2021).

Other publications

- [A4] V. Novičenko, **G. Žlabys**, E. Anisimovas, Flow-equation approach to quantum systems driven by an amplitude-modulated time-periodic force, *Phys. Rev. A* **105**, 012203 (2022).
- [A5] H. R. Hamed, E. Paspalakis, **G. Žlabys**, G. Juzeliūnas, J. Ruseckas, Complete energy conversion between light beams carrying orbital angular momentum using coherent population trapping for coherently driven double- Λ atom-light-coupling scheme, *Phys. Rev. A* **100**, 023811 (2019).
- [A6] M. Račiūnas, **G. Žlabys**, A. Eckardt, E. Anisimovas, Modified interactions in a Floquet topological system on a square lattice and their impact on a bosonic fractional Chern insulator state, *Phys. Rev. A* **93**, 043618 (2016).
- [A7] E. Anisimovas, **G. Žlabys**, B. M. Anderson, G. Juzeliūnas, A. Eckardt, Role of real-space micromotion for bosonic and fermionic Floquet fractional Chern insulators, *Phys. Rev. B* **91**, 245135 (2015).

Conference presentations

- [B1] **G. Žlabys**, E. Anisimovas, Optical Ladder Lattices With Tunable Flux, Synthetic Dimensions in Quantum Engineered Systems, Zürich, Switzerland, 2017.
- [B2] **G. Žlabys**, E. Anisimovas, Optical Ladder Lattices With Tunable Flux, Humboldt Kolleg, Vilnius, Lithuania, 2018.
- [B3] **G. Žlabys**, Optical Ladder Lattices With Tunable Flux, Ultracold Fermions, Les Houches, France, 2018.
- [B4] **G. Žlabys**, M. Račiūnas, E. Anisimovas, Learning quantum structures in compact localized eigenstates, Young Atom Opticians 2019, Hamburg, Germany, 2019.
- [B5] **G. Žlabys**, M. Račiūnas, E. Anisimovas, Learning quantum structures in compact localized eigenstates, Time Crystals and Related Phenomena, Krakow, Poland, 2019.
- [B6] **G. Žlabys**, C.-h. Fan, E. Anisimovas, K. Sacha, Engineering time-space crystalline structures, Conference on Time Crystals, virtual, 2021.
- [B7] **G. Žlabys**, C.-h. Fan, E. Anisimovas, K. Sacha, Engineering time-space crystalline structures, Open Readings 2021, virtual, 2021.

Chapter 1

MODELING OPTICAL LATTICES

The processes that occur in ultracold atoms trapped in optical lattices are modeled based on a variety of concepts that can be found in the fields of quantum optics, condensed matter and statistical physics. In this chapter, we will give a short introduction to the selected topics which cover the basic description of an optical lattice, the tight-binding model, artificial gauge fields, topological properties associated with such systems and Floquet theory.

1.1 Optical lattices

The key ingredient of exploring condensed matter physics in ultracold atom systems is an optical lattice that traps neutral atoms in clean periodic arrays with highly tunable parameters. In this section, we will overview the atom-light interaction that captures the atoms in a periodic potential and introduce the Hamiltonian formulation describing the behavior of particles in optical lattices following Refs. [65, 66].

1.1.1 Atom-light interaction

Optical lattices capture neutral atoms in the intensity maxima or minima of interfering laser beams. Let us analyze a semi-classical system that consists of a single atom placed in a classical electric field to elucidate the trapping mechanism.

Let an atom be placed in a position \vec{r} and time t dependent electric field $\vec{E}(\vec{r}, t)$ generated by a laser of frequency ω_L . If the laser frequency is detuned from the allowed transitions of the atom, then the light-induced electric dipole follows the oscillations of the electric field without creating an electronic excitation. The effect this has on the energy levels of the atom can be considered perturbatively.

We focus on a two-level system that consists of a zero-energy ground state $|g\rangle$ and a state $|e\rangle$ that has the energy $\hbar\omega_e$. Here ω_e is the transition frequency

and \hbar – the reduced Plank’s constant. The choice of state $|e\rangle$ is determined by its frequency ω_e being the closest one to the laser frequency out of all the frequencies of non-resonant transitions. The energy detuning between the laser field and state $|e\rangle$ is denoted by $\Delta \equiv \hbar(\omega_L - \omega_e)$. The two-level system is coupled to the electric field through the interaction Hamiltonian

$$\hat{H}_{\text{dip}} = -\vec{\hat{\mu}}\vec{E}(\vec{r}, t), \quad (1.1)$$

where $\vec{\hat{\mu}}$ is the electric dipole operator. If the natural linewidth Γ of the transition from the excited state to the ground state is much smaller than the detuning Δ , then the second-order perturbation theory can be applied to the interaction term. Assuming the rotating-wave approximation regime ($\omega_L/\omega_e \approx 1$) to cancel out time dependence, the perturbation theory gives a spatially dependent energy correction $\delta\varepsilon$ to the ground and excited states respectively [65]:

$$\delta\varepsilon_g(\vec{r}) = \frac{|\langle e|\vec{\hat{\mu}}|g\rangle\vec{E}(\vec{r})|^2}{\Delta} = \frac{3\pi c^2}{2\omega_e^3} \frac{\Gamma}{\Delta} I(\vec{r}), \quad (1.2)$$

$$\delta\varepsilon_e(\vec{r}) = -\frac{|\langle e|\vec{\hat{\mu}}|g\rangle\vec{E}(\vec{r})|^2}{\Delta} = -\frac{3\pi c^2}{2\omega_e^3} \frac{\Gamma}{\Delta} I(\vec{r}), \quad (1.3)$$

where the intensity is defined as $I(\vec{r}) = 2\epsilon_0 c |\vec{E}(\vec{r})|^2$ with ϵ_0 being vacuum permittivity and c – speed of light in vacuum. This light induced shift is known as AC Stark effect [67]. Ultracold atom gases are usually experimentally prepared in their ground state, therefore we focus on the ground state energy correction $\delta\varepsilon_g(\vec{r})$ that forms the potential pattern capturing the atoms in the minima. Two types of traps can be realized depending on the choice of detuning Δ . If the laser frequency is blue-detuned, i.e. larger than the resonance frequency between the two atom levels ($\Delta > 0$), then the energy minima where the atoms are trapped coincide with the intensity minima since all quantities in Eq. 1.2 are positive. On the other hand, if the light is red-detuned ($\Delta < 0$), then the energy minima form at the maxima of intensity to which the atoms are attracted.

The geometry of the trapping potential $V(\vec{r}) \propto \delta\varepsilon_g(\vec{r}) \propto I(\vec{r})$ is completely determined by the intensity of the electric field. In practice, a choice of interfering laser beam configurations allows to realize a variety of 1D, 2D and 3D lattice geometries [11]. Different phases of matter can be simulated by tuning the amplitude of the intensity [22]. A simple example of a 1D optical lattice formation is two interfering counter-propagating plane waves with wavevectors $\pm\vec{k}_L$ oriented parallel to the \vec{x} direction creating a cosine squared periodic potential $V(x) \propto |e^{ik_L x} + e^{-ik_L x}|^2 \propto \cos^2(k_L x)$ with the period equal to half of the wavelength of the waves.

So far we have introduced optical lattice potentials that induce conservative

forces trapping the particles. Another important aspect is the decoherence effects that cause particle losses to excited states. Decoherence can occur due to technical noise like optical lattice intensity fluctuations [68] or more fundamentally due to incoherent light scattering. The incoherent light scattering rate which is the electric field power absorbed/emitted by the system per electric field quantum

$$\Gamma_{\text{sc}}(\vec{r}) = \frac{3\pi c^2}{2\hbar\omega_e^3} \left(\frac{\Gamma}{\Delta}\right)^2 I(\vec{r}), \quad (1.4)$$

defines the timescale of the observed experiment, i.e. the observable event rate should be higher than the scattering rate. We see that it is related to the lattice potential by $\Gamma_{\text{sc}}(\vec{r}) = \frac{\Gamma}{\hbar\Delta} \delta\varepsilon_g(\vec{r})$. An immediate observation follows that to minimize dissipation, the detuning should be large.

Having briefly overviewed the basic underlying physics of an optical lattice we will proceed to simplified models that describe the behavior of particles trapped in such potentials.

1.1.2 Single-particle lattice Hamiltonian

Neutral atom gas trapped in an optical lattice can be treated in terms of the Hamiltonian formalism. Here we restrict the analysis to a 1D lattice but it is easily generalized for higher dimensions.

For non-interacting systems, the quantum description can be obtained by performing first quantization – promoting the classical canonical position x and momentum p_x coordinates to linear operators $\hat{x} = x$ and $\hat{p}_x = -i\hbar\frac{\partial}{\partial x}$ in the position basis satisfying the commutation relation $[\hat{x}, \hat{p}_x] = i\hbar$. These operators act on the single-particle complex Hilbert space \mathcal{H}_1 of physical states and map them onto other states of the same space. In this case, the Hamiltonian operator governing the dynamics of the system is

$$\hat{H} = \frac{\hat{p}_x^2}{2m} + V(\hat{x}), \quad (1.5)$$

where the first term describes the kinetic energy of a mass m particle and the second term – its potential energy due to the presence of an optical lattice. Solving the Schrödinger’s equation for such a system provides the eigenstates from which all of the expectation values of observables of interest can be calculated.

To simplify analytical derivations the lattices are usually modeled as either having infinite number of sites (potential minima) or satisfying the periodic boundary condition where the last site is coupled to the first site of a finite lattice forming a ring. These assumptions allow to accurately capture the bulk properties of the lattice by exploiting the discrete translational symmetry of the potential. Employing the Bloch’s theorem [69] which states that for

any periodic potential the time-independent Schrödinger's equation has Bloch wavefunction solutions of the form

$$\psi_{k,n}(x) = e^{ikx} u_{k,n}(x), \quad (1.6)$$

where $u_k(x)$ is a function that has the same periodicity as the potential, k is the quasi-momentum characterizing the translational symmetry of the lattice and n is the band index associated with energy eigenvalue of the given state. The quasi-momentum can take values $k = \frac{2\pi j}{L}$ with $j \in \mathbb{Z}$ for a lattice with L sites and the periodic boundary condition or it can take any continuous value if the number of sites is infinite. However, due to periodicity, all of the necessary information is contained in the first Brillouin zone (BZ) $-\frac{\pi}{d} \leq k < \frac{\pi}{d}$ where d is the spatial period of the potential. Acting on the Bloch wavefunction with the Hamiltonian (1.5) we get

$$\hat{H}\psi_{k,n}(x) = e^{ikx} \left[\frac{(\hat{p}_x + \hbar k)^2}{2m} + V(\hat{x}) \right] u_{k,n}(x). \quad (1.7)$$

Denoting the Hamiltonian with the modified momentum by

$$\hat{H}_k \equiv \frac{(\hat{p}_x + \hbar k)^2}{2m} + V(\hat{x}), \quad (1.8)$$

the time-independent Schrödinger's equation is simplified to independent eigenvalue problems for each k -mode

$$\hat{H}_k u_{k,n}(x) = E_{k,n} u_{k,n}(x), \quad (1.9)$$

with $E_{k,n}$ being the energy eigenvalue. The solutions $u_{k,n}(x)$ can be either calculated numerically or, in certain cases, analytically – e.g. in the weak potential limit or the tight-binding regime [70].

The obtained energy eigenspectrum contains information about the transport properties of the system. A narrow wavepacket corresponding to a particle's wavefunction centered around k_0 quasimomentum and placed in the n -th band has a group velocity $v_g(k_0) = \frac{1}{\hbar} \frac{\partial E_n(k)}{\partial k} \Big|_{k_0}$. Here, the function $E_n(k) = E_{k,n}$ maps the quasimomenta of the first Brillouin zone to the energy eigenvalues. Note that if the energy band is flat, i.e. $E_n(k) = \text{const.}$ for all k , the kinetics of the wavepacket are suppressed. Systems that support flat bands are good candidates to probe many-body effects where interactions dominate [71] and will be of main interest in section 3.2.

1.1.3 Second quantization and the tight-binding approximation

Using the first quantization formalism, many-body states describing interacting bosons (fermions) trapped in an optical lattice are the (anti-)symmetrized tensor products of their single-particle states. Each time a particle is spatially exchanged or removed/added to the system, the state symmetry has to be addressed, therefore it is often more convenient to work in an occupation number representation also known as second quantization. In this representation, instead of tracking the state of each particle, the many-body state lists how many particles occupy each single-particle state while the symmetry is taken care of implicitly by the construction of the space of states.

In second quantization, the many-body state is an element of Fock space \mathcal{F} which is the direct sum of all products of single-particle Hilbert spaces $\mathcal{F} = \bigoplus_{n=0}^{\infty} \mathcal{H}_1^{\otimes n}$ where the tensor product of single-particle spaces $\mathcal{H}_1^{\otimes n} = \underbrace{\mathcal{H}_1 \otimes \dots \otimes \mathcal{H}_1}_n$ is symmetrized (antisymmetrized) for bosons (fermions) and $\mathcal{H}_1^{\otimes 0} = \mathbb{C}$ is the 1D vector space spanned by the vacuum state. A state in Fock space can be represented in an orthonormal and complete occupation number basis where n_j particles occupy the j -th single-particle state. Such a many-body state can be denoted by an ordered list of occupation numbers $|n_1, n_2, \dots, n_j, \dots\rangle$. In order to include or remove a particle in the j -th mode, the creation \hat{a}_j^\dagger and annihilation \hat{a}_j operators are introduced. They satisfy the canonical commutation relations for bosons

$$[\hat{a}_i, \hat{a}_j^\dagger] = \hat{a}_i \hat{a}_j^\dagger - \hat{a}_j^\dagger \hat{a}_i = \delta_{ij}; \quad [\hat{a}_i, \hat{a}_j] = [\hat{a}_i^\dagger, \hat{a}_j^\dagger] = 0, \quad (1.10)$$

and anticommutation relations for fermions

$$\{\hat{a}_i, \hat{a}_j^\dagger\} = \hat{a}_i \hat{a}_j^\dagger + \hat{a}_j^\dagger \hat{a}_i = \delta_{ij}; \quad \{\hat{a}_i, \hat{a}_j\} = \{\hat{a}_i^\dagger, \hat{a}_j^\dagger\} = 0, \quad (1.11)$$

with δ_{ij} being the Kronecker delta. Creation and annihilation operators acting on the j -th mode of a bosonic system correspondingly add and subtract a particle from the targeted mode:

$$\hat{a}_j^\dagger |n_1, \dots, n_j, \dots\rangle = \sqrt{n_j + 1} |n_1, \dots, n_j + 1, \dots\rangle, \quad (1.12)$$

$$\hat{a}_j |n_1, \dots, n_j, \dots\rangle = \sqrt{n_j} |n_1, \dots, n_j - 1, \dots\rangle, \quad (1.13)$$

where for bosons n_j can be any number of particles. For fermions, due to the Pauli exclusion principle, we have that the number of particles per each mode

is restricted to $n_j \in \{0, 1\}$, thus the operators act as

$$\hat{a}_j^\dagger |n_1, \dots, n_j, \dots\rangle = (-1)^{\sum_{\ell=1}^{j-1} n_\ell} (1 - n_j) |n_1, \dots, 1 - n_j, \dots\rangle, \quad (1.14)$$

$$\hat{a}_j |n_1, \dots, n_j, \dots\rangle = (-1)^{\sum_{\ell=1}^{j-1} n_\ell} n_j |n_1, \dots, 1 - n_j, \dots\rangle. \quad (1.15)$$

Here the alternating sign that depends on the order of the single-particle state occupancy appears due to the anticommutation relations. An operator that counts the number of particles in the j -th mode can be defined in terms of the creation and annihilation operators $\hat{n}_j \equiv \hat{a}_j^\dagger \hat{a}_j$:

$$\hat{n}_j |n_1, \dots, n_j, \dots\rangle = n_j |n_1, \dots, n_j, \dots\rangle. \quad (1.16)$$

It is known as the particle number or density operator and is identical for both bosons and fermions.

Having introduced the creation and annihilation operators we define the quantum field operators

$$\hat{\Psi}^\dagger(x) = \sum_{j=1}^{\infty} \psi_j^*(x) \hat{a}_j^\dagger \quad \text{and} \quad \hat{\Psi}(x) = \sum_{j=1}^{\infty} \psi_j(x) \hat{a}_j, \quad (1.17)$$

that are expressed in terms of a complete orthonormal set of first quantization functions $\psi_j(x)$ in position representation. The operator $\hat{\Psi}^\dagger(x)$ creates and $\hat{\Psi}(x)$ destroys a particle at position x while accounting for all of the single-particle mode contributions. Bosonic field operators inherit the commutation relations for bosons

$$[\hat{\Psi}(x), \hat{\Psi}^\dagger(x')] = \delta(x - x'); \quad [\hat{\Psi}(x), \hat{\Psi}(x')] = [\hat{\Psi}^\dagger(x), \hat{\Psi}^\dagger(x')] = 0, \quad (1.18)$$

and fermionic field operators obey the anticommutation relations

$$\{\hat{\Psi}(x), \hat{\Psi}^\dagger(x')\} = \delta(x - x'); \quad \{\hat{\Psi}(x), \hat{\Psi}(x')\} = \{\hat{\Psi}^\dagger(x), \hat{\Psi}^\dagger(x')\} = 0, \quad (1.19)$$

where $\delta(x - x')$ is the Dirac delta function.

Let us generalize the Hamiltonian (1.5) for many trapped ultracold gas particles in an optical lattice and include an interaction term with an experimentally controllable [72] potential $U(x_i - x_j)$ that depends on the distance between two particles at positions x_i and x_j :

$$\hat{H} = \sum_i \left[-\frac{\hbar^2}{2m} \frac{\partial^2}{\partial x_i^2} + V(x_i) \right] + \frac{1}{2} \sum_i \sum_{j \neq i} U(x_i - x_j). \quad (1.20)$$

The sums run over all particles in the lattice. The same Hamiltonian can be

written in terms of field operators [73]

$$\begin{aligned} \hat{H} = & \int dx \hat{\Psi}^\dagger(x) \left[-\frac{\hbar^2}{2m} \frac{\partial^2}{\partial x^2} + V(x) \right] \hat{\Psi}(x) \\ & + \frac{1}{2} \int dx \int dx' \hat{\Psi}^\dagger(x) \hat{\Psi}^\dagger(x') U(x-x') \hat{\Psi}(x') \hat{\Psi}(x). \end{aligned} \quad (1.21)$$

Ultracold atom systems exist at extremely low temperatures and energies therefore we will employ the tight-binding approximation. It assumes that the particles are in the lowest energy band and localized around the lattice minima while the interaction energy is insufficient to excite the particles to a higher energy band. In this case the field operators can be expanded in terms of localized Wannier functions [74]

$$w_j(x) \equiv w(x-x_j) = \mathcal{N} \int_{\text{BZ}} dk e^{-ikx_j} \sum_n G_n(k) \psi_{k,n}(x), \quad (1.22)$$

where \mathcal{N} is the normalization constant, $\psi_{k,n}(x)$ is the Bloch function (1.6), x_j is the lattice site coordinate around which the Wannier function is centered and $G_n(k)$ is a gauge transformation coefficient. The Wannier functions are not uniquely defined due to the arbitrary phase of the Bloch functions therefore an ansatz is made that $G_m(k)$ coefficients are chosen to minimize the spatial spread of the Wannier function thus uniquely defining it. This can be done analytically for 1D periodic and symmetric potentials [75] and numerically for more complex systems [76]. Expanding the field operators in Wannier basis $\hat{\Psi}(x) = \sum_{j=1}^{\infty} w_j(x) \hat{a}_j$ and plugging them in to the Hamiltonian (1.21) we can express the result in terms of creation and annihilation operators

$$\hat{H} = - \sum_{\langle ij \rangle} J_{ij} \hat{a}_i^\dagger \hat{a}_j + \frac{1}{2} \sum_{i,j,l,n} U_{ijkl} \hat{a}_i^\dagger \hat{a}_j^\dagger \hat{a}_l \hat{a}_n, \quad (1.23)$$

with $\langle ij \rangle$ indicating the summation over directed links connecting adjacent sites (i.e. for fixed neighboring sites i and j , terms proportional to both J_{ij} and J_{ji} are included in the sum). Here the tunneling strength from site j to i is defined as

$$J_{ij} \equiv - \int dx w_i^*(x) \left[-\frac{\hbar^2}{2m} \frac{\partial^2}{\partial x^2} + V(x) \right] w_j(x) \quad (1.24)$$

and the interaction strength is

$$U_{ijkl} \equiv \int dx \int dx' w_i^*(x) w_j^*(x') U(x-x') w_l(x') w_n(x). \quad (1.25)$$

The first term of this Hamiltonian is known as the tight-binding model Hamiltonian which describes particle hopping between nearest neighboring lattice

sites

$$\hat{H}_{\text{TB}} = - \sum_{\langle ij \rangle} J_{ij} \hat{a}_i^\dagger \hat{a}_j \quad (1.26)$$

and $\langle ij \rangle$ indicates summation of all directed links connecting neighbors. The tight-binding Hamiltonian together with the interaction term form the so called Hubbard-type models [17] which are widely used in condensed matter physics to describe quantum phase transitions [21, 22], topological properties [77, 78] and phenomena such as many-body localization [79, 80] of ultracold gases trapped in periodic potentials.

This framework will be used for the construction of time-space crystalline structures in chapter 2. In chapter 3, the Hamiltonians of the flat band lattice systems will be assumed to have the form of Hubbard-type models of Eq. (1.23).

1.2 Magnetic flux in a lattice of neutral atoms

Atoms trapped in optical lattice experiments are neutral therefore they do not experience Lorentz force when placed in a magnetic field. This seems like an immediate drawback of such systems since phenomena like integer and fractional Hall effects which are hallmark examples of topological order would be barred from exploration. Fortunately, magnetic effects can be simulated by employing laser-induced gauge fields [81] or periodically driving the lattice [30].

In this section, we focus on the theoretical description of gauge fields that affect the transport properties of particles similarly to magnetic fields and show how they are accommodated in the lattice tight-binding Hamiltonian following Refs. [32, 82, 83]. Topological properties and the related effects that arise due to the presence of such gauge fields will be introduced as well.

1.2.1 Gauge field induced flux

Assume that a system is described by a Hamiltonian $\hat{H}(\lambda)$ that depends on a collection of parameters $\lambda = (\lambda^1, \dots, \lambda^M)$ where the superscript indicates the components of the MD parameter space. According to the adiabatic theorem, if the parameters $\lambda(t)$ vary slowly in time compared to the typical time scales determined by the gaps between the energy bands, a non-degenerate eigenstate of $\hat{H}(\lambda(t))$ remains in the same instantaneous eigenstate throughout the evolution up to a phase factor. In general, the global phase factor of the state does not impact the expectation values of measured observables, however in interference experiments the relative phase between the interfering states has physical significance, e.g. as seen from the Aharonov-Bohm effect [84]. In the following subsection, we adiabatically evolve the parameters $\lambda(t)$ in a closed loop in the parameter space and analyze why the accumulated phase arises in the system.

Let the system be initially prepared in an eigenstate $|\psi_i; \lambda(t=0)\rangle$. After adiabatically evolving the state for time t , the solution of the time-dependent Schrödinger equation will have the form

$$|\Psi(t)\rangle = e^{i\theta_i(t)} e^{i\gamma_i(t)} |\psi_i; \lambda(t)\rangle + \epsilon \sum_{j \neq i} c_j(\lambda(t)) |\psi_j; \lambda(t)\rangle. \quad (1.27)$$

The first term is the initial state that acquired the usual dynamical phase $\theta_i(t) \equiv -\frac{1}{\hbar} \int_0^t dt' E_i(\lambda(t'))$ and another phase factor $\gamma_i(t)$ that we will determine later. Here E_i is the eigenenergy of the i -th state. The second term is the sum over the remaining eigenstates with some complex coefficients $c_j(\lambda(t))$ that are weighed by small dimensionless factor ϵ characterizing adiabaticity which goes to zero in the adiabatic limit. To determine the phase $\gamma_i(t)$, we plug the solution in the time-dependent Schrödinger equation $i\hbar \frac{d|\Psi(t)\rangle}{dt} = \hat{H}(\lambda(t)) |\Psi(t)\rangle$ and arrive at

$$\left(i \frac{d\gamma_i}{dt} + \frac{d}{dt} \right) |\psi_i; \lambda(t)\rangle = -\epsilon e^{-i\theta_i} e^{-i\gamma_i} \sum_{j \neq i} \left(\frac{i}{\hbar} E_j c_j + \frac{dc_j}{dt} + c_j \frac{d}{dt} \right) |\psi_j; \lambda(t)\rangle, \quad (1.28)$$

where the time dependence of the coefficients and phases is omitted for brevity. The terms on the left-hand side (LHS) are of the same order as ϵ since they vanish if there is no change in the Hamiltonian parameters. The first two terms on the right-hand side (RHS) have the prefactor ϵ hence they match the order of the LHS. The third term is of second order in ϵ since it is a product of ϵ and $c_j \frac{d|\psi_j; \lambda(t)\rangle}{dt}$ which is of order ϵ . Neglecting this term and projecting the initial state on Eq. (1.28), we see that the RHS vanishes and we are left with equation

$$i \frac{d\gamma_i(t)}{dt} + \langle \psi_i; \lambda(t) | \frac{d}{dt} | \psi_i; \lambda(t) \rangle = 0. \quad (1.29)$$

Solving it allows us to determine the phase factor

$$\gamma_i(t) = i \int_0^t dt' \langle \psi_i; \lambda(t') | \frac{d}{dt'} | \psi_i; \lambda(t') \rangle = i \int_{\lambda(0)}^{\lambda(t)} d\lambda^\mu \langle \psi_i; \lambda | \frac{\partial}{\partial \lambda^\mu} | \psi_i; \lambda \rangle, \quad (1.30)$$

where we have used the chain rule in the last equality to obtain the derivative with respect to the parameter space variable λ^μ with the implicit summation over the repeating parameter index $\mu \in \{1, 2, \dots, M\}$. For a path $\partial\Gamma$ that forms a closed loop in parameter space (i.e. $\lambda(0) = \lambda(t)$) this phase cannot be gauged away (modulo 2π) by a choice of a global phase. This phase is known as Berry [85] or geometric phase

$$\gamma_i(\partial\Gamma) = i \oint_{\partial\Gamma} d\lambda^\mu \langle \psi_i; \lambda | \frac{\partial}{\partial \lambda^\mu} | \psi_i; \lambda \rangle, \quad (1.31)$$

due to its dependence only on the path taken in the parameter space. This

can be written more compactly by introducing Berry connection (also known as Berry potential)

$$\mathcal{A}_\mu \equiv i\langle\psi_i; \lambda| \frac{\partial}{\partial\lambda^\mu} |\psi_i; \lambda\rangle, \quad (1.32)$$

which is gauge-dependent since if a state is phase shifted by some parameter dependent phase $-\omega(\lambda)$, i.e. $|\psi_i; \lambda\rangle \rightarrow e^{-i\omega(\lambda)}|\psi_i; \lambda\rangle$, then the potential transforms as $\mathcal{A}_\mu \rightarrow \mathcal{A}_\mu + \frac{\partial\omega(\lambda)}{\partial\lambda^\mu}$. Berry connection describes the transport of the eigenstate through parameter space. An associated gauge-independent quantity that describes the curvature arising due to the potential is Berry curvature (or field)

$$\mathcal{F}_{\mu\nu} \equiv \frac{\partial\mathcal{A}_\nu}{\partial\lambda^\mu} - \frac{\partial\mathcal{A}_\mu}{\partial\lambda^\nu}. \quad (1.33)$$

Using these definitions we can rewrite Berry phase while applying Stoke's theorem

$$\gamma_i = \oint_{\partial\Gamma} d\lambda^\mu \mathcal{A}_\mu = \int_{\Gamma} dS^{\mu\nu} \mathcal{F}_{\mu\nu}. \quad (1.34)$$

In the last equality, we integrate over the surface Γ bounded by the curve $\partial\Gamma$. Here $dS^{\mu\nu}$ is the volume form of the surface and summation over repeating Greek indices is implied with the condition that $\mu < \nu$.

From Eq. (1.34) we see that the Berry phase acquired by an eigenstate transported along a closed loop in parameter space is equivalent to a flux, induced by the Berry curvature, integrated over the area enclosed by the taken path. An example of such a phenomenon is the Aharonov-Bohm effect, where two wave packets prepared in the same state at the same spatial point are propagated along different spatial routes in the presence of a magnetic vector potential $\vec{A}(\vec{x})$ and interfered at some final point [86–88]. The interference pattern shows a phase difference between the two states that depends on the magnetic flux enclosed by their paths. To elucidate the equivalence with the Berry phase, the effect can be formulated as transporting a single wave packet along a closed path and interfering it with a wave packet at the initial position. This leads to an Aharonov-Bohm phase

$$\varphi_{\text{AB}} = \frac{q}{\hbar} \oint_{\partial P} d\vec{x} \cdot \vec{A}(\vec{x}) = \frac{q}{\hbar} \int_P d\vec{S} \cdot \vec{B}(\vec{x}) = \frac{q}{\hbar} \Phi, \quad (1.35)$$

where q is charge, ∂P is the closed trajectory taken by the wave-packet, P is the area enclosed by the trajectory, Φ is the magnetic flux piercing this area, $d\vec{S}$ is an area element and $\vec{B}(\vec{x}) = \vec{\nabla} \times \vec{A}$ is the magnetic field. Since the Berry connection and the magnetic vector potential share the same gauge properties we can identify the Berry connection as $\vec{\mathcal{A}} = \frac{q}{\hbar} \vec{A}$ and the spatial coordinates of the system in this case act as parameters. Thus we see that the Aharonov-Bohm phase is just a particular manifestation of the Berry phase.

The geometric nature of the electromagnetic effects allows us to simulate their presence by engineering suitable gauge fields. This overcomes the inherent

problem of optical lattices filled with neutral atoms since the charge is no longer a crucial component to induce and observe magnetic phenomena. Note that the discussed Berry phase factor belongs to the unitary group $U(1)$ and the Berry connection is an element of the corresponding Lie algebra $\mathfrak{u}(1)$. The created gauge field is static since it is not affected by the motion of particles. Higher n -degree symmetries can be realized by applying non-Abelian artificial gauge potentials belonging to $\mathfrak{u}(n)$ or $\mathfrak{su}(n)$ and the dynamic gauge fields can be created by using different species of particles laying a path for exploration of lattice gauge theories in ultracold atom systems [89–91].

1.2.2 Tight-binding model with flux

Introduction of artificial gauge fields in the tight-binding lattice model is known as Peierls substitution [92, 93] which results in complex tunneling parameters that emulate magnetic effects. It states that the tunneling element of particle hopping from site j to site i in a presence of a sufficiently slow varying gauge field acquires a phase factor called the Peierls phase

$$\theta_{ij} = \int_{\vec{x}_j}^{\vec{x}_i} d\vec{x} \cdot \vec{\mathcal{A}}(\vec{x}), \quad (1.36)$$

where $\vec{\mathcal{A}}(\vec{x})$ is a gauge potential generating the field and the integral is performed along the line connecting the sites at \vec{x}_j and \vec{x}_i . The tight-binding Hamiltonian (1.26) can be straightforwardly updated to account for this phase as

$$\hat{H}_{\text{TB}} = - \sum_{\langle ij \rangle} J_{ij} e^{i\theta_{ij}} \hat{a}_i^\dagger \hat{a}_j, \quad (1.37)$$

assuming that J_{ij} parameters are real. The Peierls phase is a gauge-dependent quantity, however if the particle tunnels along a closed path it accumulates the Berry phase that can not be gauged away. For 2D lattices, the area enclosed by the path is called a plaquette, e.g. for a 2D square lattice affected by some gauge potential, the dimensionless flux (Berry phase) $\gamma = \theta_{14} + \theta_{43} + \theta_{32} + \theta_{21}$ piercing a lattice plaquette is shown in Fig. 1.1. One of the most prominent models that can be expressed as the tight-binding Hamiltonian with flux is the Hofstadter model [35, 94] which describes a 2D square lattice with homogeneous flux throughout each of the lattice plaquettes and features quantum Hall phases with topological order. Another important example is the Haldane model which showed that the essential component of the Hall effect is not the magnetic field but the time-reversal symmetry breaking [95, 96] – the explored system is a hexagonal lattice which in addition to the nearest-neighbor tunneling includes next-nearest neighbor hoppings that create a non-zero local magnetic flux while the total magnetic flux remains zero.

Experimentally the Peierls phase can be induced by using the laser-assisted

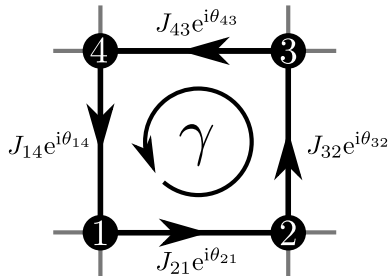


Figure 1.1: A single 2D lattice cell with four sites labeled 1 to 4. A particle hopping along the directed links indicated by arrows with appropriate weights $J_{ij}e^{i\theta_{ij}}$ completes a closed loop 1 – 2 – 3 – 4 – 1 and acquires a phase γ . It is equivalent to a dimensionless flux γ piercing the square lattice plaquette.

tunneling method [97,98] which relies on suppression of spontaneous tunneling between the neighboring sites and reestablishment of controllable hopping via external atom-light coupling lasers or lattice shaking. Comprehensive reviews can be found in Refs. [30,32]. A particular realization of a controllable phase using Raman laser beams will be introduced in subsection 2.5.3 for adjustment of flux in time-space crystalline structures.

1.2.3 Topological properties

Lattice systems with artificial gauge fields host a variety of topological phases of matter that are robust to perturbations such as quantum anomalous Hall insulators (Chern insulators) [99–101], topological Mott insulators [102–104], \mathbb{Z}_2 topological insulators [105,106] and topological superconductors [107]. Here we will briefly introduce the key characteristics that are prevalent in such systems – an invariant associated with the bulk properties of the lattice and the topological edge states.

The experimental observation of quantized Hall conductance in cold 2D electron gas in a strong perpendicular magnetic field [34] prompted the theoretical exploration of this effect which is known as integer quantum Hall effect and revealed its connection with topology [108]. It was shown that the transverse conductance σ_{xy} obtained from the linear response theory can be expressed in terms of a topological invariant $\nu_1^{(m)}$ classifying the m non-degenerate isolated energy bands of the 2D Hamiltonian describing the system

$$\sigma_{xy} = -\frac{e^2}{2\pi\hbar} \sum_m \nu_1^{(m)}. \quad (1.38)$$

Here the summation runs over the m occupied energy bands and e is the electron charge. The topological invariant $\nu_1^{(m)} \in \mathbb{Z}$ is known as the first Chern number [109] and it assigns an integer to a manifold of states defined over a

closed parameter surface. In this situation, it is related to the Berry curvature $\mathcal{F}^{(m)}$ associated with the m -th energy band through the following equality

$$\nu_1^{(m)} = \frac{1}{2\pi} \oint_{\text{BZ}} dk_1 dk_2 \mathcal{F}_{12}^{(m)}. \quad (1.39)$$

The integral is taken over the first Brillouin zone where the periodic quasi-momentum $\vec{k} = (k_1, k_2)$ forms a closed 2D manifold. The Berry curvature is defined in terms of the eigenstates $|u_m(\vec{k})\rangle$ of the reciprocal Hamiltonian $\hat{H}(\vec{k})$ describing the 2D system:

$$\mathcal{F}_{12}^{(m)} = \frac{\partial \mathcal{A}_2}{\partial k_1} - \frac{\partial \mathcal{A}_1}{\partial k_2}, \quad \text{with} \quad \mathcal{A}_\mu = i \langle u_m(\vec{k}) | \frac{\partial}{\partial k_\mu} | u_m(\vec{k}) \rangle, \quad \mu \in \{1, 2\}. \quad (1.40)$$

Since the Chern number can only take integer values, the Hall conductance (1.38) is robust against perturbations of the system's Hamiltonian that do not close the gaps between the energy bands. A non-zero Chern number implies that the wavefunctions exhibit a non-trivial topological structure in the Brillouin zone, i.e. there is no continuous and smooth global gauge choice for the wavefunctions thus multiple different phase conventions are needed for separate regions to cover the whole Brillouin zone.

The same formalism can be applied to calculate the Chern numbers of isolated energy bands of trapped ultracold atom gases in optical lattices where the artificial gauge field is engineered by some Peierls phase-inducing method. The eigenstates required to calculate the gauge potential in Eq. (1.40) are obtained by diagonalizing the tight-binding Hamiltonian (1.37) in quasimomentum representation. The presence of non-trivial Chern numbers in such systems gives rise to the quantum anomalous Hall effect where the conductance is quantized as in the quantum integer Hall effect and it is called anomalous because no external magnetic field is present. A lattice that supports this effect is termed a Chern insulator [36] with one of the most famous examples hosting such a phase being the Haldane model [95,110]. With the advancement of technology, higher-dimensional systems became experimentally accessible [44, 111] prompting interest in applying the generalized Chern number to describe higher-dimensional topological effects as well [45,112].

Another important characteristic of systems with non-trivial Chern number is the topological edge state. It appears at an interface where the topological invariant changes, e.g. where a lattice shares an open boundary with the vacuum. For the 2D integer quantum Hall effect, it can be understood semiclassically as describing the chiral motion of an electron bouncing in skipping orbits at the edge of the system. In the energy band structure it appears as a gapless mode connecting the otherwise gapped bulk bands [113,114]. An example of energy dispersion with edge states present will be shown in section 2.5.4 Fig. 2.11(b) for a quasi-one-dimensional square lattice with flux.

Although measuring transport properties like conductance in condensed matter systems is straightforward, for quantum gases it becomes challenging since it requires more complicated setups, e.g. connecting reservoirs of particles to the system and devising a way to observe the currents [115] or by inducing trap modulations to probe resistivity [116]. Fortunately, complementary methods can be introduced to measure the topological properties of the system: atom densities measured at different values of the artificial flux allow for calculating the sum of Chern numbers [117], a variety of time-of-flight measurements where the expansion of the atomic cloud is monitored after turning off the external trap also provides access to the Chern number [118–121] and semiclassical dynamics of quasimomentum wave-packets can map the Berry curvature of the Brillouin zone [96, 122]. The edge states can be detected by Bragg spectroscopy [123, 124] and observing the time evolution of the quantum gas after suddenly releasing constraining walls [125].

The introduced artificial gauge fields overcome the limitations of observing magnetic effects in neutral ultracold atom systems. The ability to measure topological quantities combined with the versatility of optical lattice trap schemes paves the way to exploring exotic phases of matter in low- and high-dimensional settings.

1.3 Floquet picture

Periodic driving of ultracold atom systems provides the means to explore and control novel dynamical behavior and phases of quantum matter. The most prominent effects induced by shaking are dynamic localization [126, 127], dynamic superfluid-Mott insulator phase transition [128], creation of artificial magnetic fields [30], topological phases [129] and new phases of matter such as phase space crystals [26] and time crystals [24, 25]. The theoretical description of time-periodic systems is covered by Floquet formalism which we briefly introduce following Refs. [25, 130].

The Floquet theorem states that for a time-periodic Hamiltonian $\hat{H}(t) = \hat{H}(t + T)$ with period $T = \frac{2\pi}{\omega}$ and associated angular frequency ω a general solutions of the time-dependent Schrödinger equation can be written as

$$\psi(x, t) = \sum_n c_n e^{-\frac{i}{\hbar} \varepsilon_n t} u_n(x, t), \quad (1.41)$$

with complex coefficients c_n and time-periodic functions $u_n(x, t) = u_n(x, t + T)$. Plugging the solutions in the time-dependent Schrödinger equation

$$\left(\hat{H}(t) - i\hbar \frac{\partial}{\partial t} \right) u_n(x, t) = \varepsilon_n u_n(x, t), \quad (1.42)$$

we see that $u_n(x, t)$ are eigenfunctions (also known as Floquet functions) of the Floquet Hamiltonian $\hat{\mathcal{H}} \equiv \hat{H}(t) - i\hbar \frac{\partial}{\partial t}$ and the eigenvalues are termed as quasienergies ε_n . Much like the quasimomentum in Bloch functions, the quasienergy is also periodic in its respective domain with energy shifts of $\hbar\omega$. This implies that shifting the quasienergies by some integer multiple $m \in \mathbb{Z}$ of $\hbar\omega$ provides a set of states related to the n -th Floquet state

$$e^{-\frac{i}{\hbar}\varepsilon_n t} u_n(x, t) = e^{-\frac{i}{\hbar}(\varepsilon_n + m\hbar\omega)t} e^{im\omega t} u_n(x, t) = e^{-\frac{i}{\hbar}\tilde{\varepsilon}_n t} \tilde{u}_n(x, t), \quad (1.43)$$

with $\tilde{u}_n(x, t) = \tilde{u}_n(x, t + T) = e^{im\omega t} u_n(x, t)$ being the associated Floquet functions with a class of quasienergies $\tilde{\varepsilon}_n = \varepsilon_n + m\hbar\omega$ that are equivalent. Due to this periodicity, it is enough to consider a single Floquet zone of width $\hbar\omega$ in the energy spectrum since it contains all the energies of the unique states describing the system.

The Floquet Hamiltonian eigenvalue problem (1.43) can be solved by treating time not as an evolution variable but as a degree of freedom representing the coordinate of time much the same as position. The Floquet function is Fourier expanded with respect to time

$$u(x, t) = \sum_{n,m} a_{n,m} \phi_n(x) e^{im \frac{\omega}{s} t}, \quad (1.44)$$

where $a_{n,m}$ are complex coefficients, s is an integer related to the choice of the periodicity, $\phi_n(x)$ are the basis functions of the Hilbert space describing the particle and $e^{im \frac{\omega}{s} t}$ are the Fourier basis functions. The Hilbert and Fourier bases together can be regarded as forming an extended Hilbert space, spanned by states $|n, m\rangle\rangle$ which when projected on the position and time coordinates give $\langle\langle x, t | n, m \rangle\rangle = \phi_n(x) e^{im \frac{\omega}{s} t}$. These states are orthonormal

$$\langle\langle n, m | n', m' \rangle\rangle = \frac{1}{sT} \int_0^{sT} dt \int dx \phi_n^*(x) e^{-im \frac{\omega}{s} t} \phi_{n'}(x) e^{im' \frac{\omega}{s} t} = \delta_{n,n'} \delta_{m,m'}. \quad (1.45)$$

Expressing the Floquet Hamiltonian matrix elements in this basis $\langle\langle n, m | \hat{\mathcal{H}} | n', m' \rangle\rangle$ and diagonalizing the resulting matrix yields the quasienergy spectrum (periodic with $\frac{\hbar\omega}{s}$ period) and the Floquet states (1.44) that we were looking for. Note that the choice of $s \in \mathbb{Z}$ arises from the periodicity of the Hamiltonian $H(t) = H(t + sT)$, thus all s are valid selections for the basis construction and the eigenstates expressed in any of the bases provide the same information, however, the periodicity of the resulting eigenspectrum is modified.

The introduced formalism will allow us to establish the Floquet Hamiltonian of resonantly driven lattice systems in chapter 2 and gain insight into the behavior of wave-packets formed by resonant Floquet states.

Chapter 2

TIME-SPACE CRYSTALLINE STRUCTURES

An ordinary crystal is a periodic array of atoms with a structure determined by inter-particle interactions. Such a crystal can be viewed as a stable quantum mechanical state that forms after spontaneous space translation symmetry breaking occurs due to an external perturbation, e.g. interaction with the environment or a measurement. The crystal state is symmetric under translations by an integer multiple of the lattice constant while the Hamiltonian describing the system possesses a higher, continuous translation symmetry which the eigenstates inherit. A time crystal [24, 25, 131–133], by analogy, is a system where the roles of time and space are interchanged. Either discrete or continuous time translation symmetry is spontaneously broken leading to a periodic behavior of the system in time that hosts a lower symmetry state than the initial Hamiltonian supported. While there are fundamental limitations of creating time crystals in equilibrium provided they do not exhibit long-range interactions [132, 134], periodically driven many-body systems allow to realize time crystals both in theory [135–138] and practice [139–144]. A hallmark example of a discrete time crystal is a Bose-Einstein condensate of ultracold atoms bouncing on a resonantly driven mirror [135], where the driving frequency is an integer multiple of the natural atom oscillation frequency, i.e. the period of the bouncing particles becomes larger than the driving period in the symmetry broken state.

Spontaneous symmetry breaking is not the only way to realize a periodic structure in the time domain. Much like in optical lattices, where the light field traps and arranges particles in a periodic potential, an effective periodic potential can be created in the temporal dimension by choosing a suitable resonant time-periodic driving [24, 25, 133, 145]. These engineered time crystalline structures provide a platform to explore condensed matter phenomena in the temporal domain. Phenomena such as Anderson localization [146–149], Mott insulating phase [150], topologically protected edge states [151, 152] and

flat-band lattices [153] are predicted.

In this chapter, we introduce time-space crystalline structures (TSCS) that exhibit both spatial and temporal periodicity. Employing the ideas of time crystalline structures we set out to construct a novel high-dimensional lattice where the time domain acts as a synthetic dimension attached to each spatial degree of freedom. The main results of this chapter are based on publication [A1]. Firstly, a time crystalline structure is engineered at each potential well of a spatially periodic lattice by employing a suitably chosen resonant periodic driving of the system. This effectively forms a 2D TSCS. Secondly, we show that the dimensionality can be extended by adding equivalent 1D spatial lattices that are mutually orthogonal with the initial spatial lattice and follow the same driving protocol. In this way, the temporal structure is exploited to effectively double the number of dimensions for each available spatial degree of freedom, leading to a TSCS with up to six dimensions given a 3D spatial lattice. Finally, artificial gauge fields are introduced in the TSCS, providing a toolbox for probing quantum Hall physics and topological properties of high-dimensional systems.

2.1 Classical analysis of a 1D driven potential

We will begin with a classical 1D potential periodically driven in time, move to a frame oscillating with the potential and then analyze the phase space diagram of such a system to gain intuition for the reason behind the appearance of the discrete localization of particles in time. A secular approximation will be introduced to simplify the description and provide a convenient way to compare quantized classical results with the quantum calculations encountered in section 2.2. A detailed overview of the underlying theory of driven systems used for the aforementioned derivations can be found in Refs. [154, 155].

2.1.1 Phase space diagram

The classical Hamiltonian of a 1D driven system with a sine-squared potential is given by

$$H(x, p_x, t) = \frac{p_x^2}{2m} + V_0 \sin^2(k_L [x - \lambda \cos(\omega t)]). \quad (2.1)$$

Here m is the mass of a test particle, V_0 – amplitude of the trapping potential, k_L – wavevector describing the spatial periodicity of the lattice, λ – maximum displacement of the lattice in the x direction due to the driving and ω is the shaking frequency. Next, we switch to the driven frame to decouple the coordinate and time-dependent term. This is done by applying a canonical transformation where we utilize the type 2 generating function G_2 to relate the old position and momentum coordinates (x, p_x) to the new ones denoted by

tilde (\tilde{x}, \tilde{p}_x) in the following way:

$$\tilde{H}(\tilde{x}, \tilde{p}_x, t) = H(x, p_x, t) + \frac{\partial G_2}{\partial t}, \quad p_x = \frac{\partial G_2}{\partial x}, \quad \tilde{x} = \frac{\partial G_2}{\partial \tilde{p}_x}.$$

Selecting $G_2 = \tilde{p}_x [x - \lambda \cos(\omega t)]$ leads to the Hamiltonian in the driven frame that has the form

$$\tilde{H}(\tilde{x}, \tilde{p}_x, t) = \frac{\tilde{p}_x^2}{2m} + V_0 \sin^2(k_L \tilde{x}) + \tilde{p}_x \lambda \omega \sin(\omega t). \quad (2.2)$$

Finally, we express this equation in recoil energy units $E_R = \frac{\hbar^2 k_L^2}{2m}$ to minimize the number of interdependent parameters. This is done by introducing primed dimensionless quantities $p'_x = \tilde{p}_x / (\hbar k_L)$, $x' = k_L \tilde{x}$, $H' = \tilde{H} / E_R$, $V'_0 = V_0 / E_R$, $\lambda' = \lambda k_L$, $\omega' = \hbar \omega / E_R$ and $t' = E_R t / \hbar$. Re-expressing the Hamiltonian in dimensionless quantities and dropping the primes to reduce notational clutter we arrive at the dimensionless Hamiltonian periodic in time and space with separated spatial and temporal terms:

$$H(x, p_x, t) = p_x^2 + V_0 \sin^2(x) + p_x \lambda \omega \sin(\omega t). \quad (2.3)$$

The equations of motion of the Hamiltonian (2.3) completely determine the properties of the classical system:

$$\frac{dp_x}{dt} = -\frac{\partial H(x, p_x, t)}{\partial x} = -V_0 \sin(2x), \quad (2.4)$$

$$\frac{dx}{dt} = \frac{\partial H(x, p_x, t)}{\partial p_x} = 2p_x + \lambda \omega \sin(\omega t). \quad (2.5)$$

To obtain an understanding of what kind of motion can be seen in this periodically driven system, it is useful to calculate the stroboscopic evolution of its phase space points at times equal to integer multiples of the driving period $T = \frac{2\pi}{\omega}$. Assuming small driving λ , a typical result for a single potential well is shown in Fig. 2.1. It encodes the three key features: regular trajectories, chaotic regions and resonant islands. Regular trajectories are quasi-periodic trajectories that follow an invariant curve in phase space. An example of such a curve can be seen for small momenta where we have circular trajectories around the origin which correspond to the system maintaining harmonic oscillations as in the undriven case. Chaotic regions become apparent at the edges of the phase space picture depicted in Fig. 2.1, their typical characteristic is that a small change of distance between two neighboring phase space points leads to on average exponentially increasing separation between their generated trajectories during stroboscopic evolution. Increasing the driving amplitude λ leads to larger chaotic regions because the regularity of the high energy trajectories gets destroyed, i.e. the perturbation is strong enough to drive the system

away from the regular undriven trajectories. Finally, we have resonant islands – closed regular trajectories that do not enclose the origin point. These islands correspond to the case when the external driving frequency is resonant to an integer multiple of a particle’s frequency Ω in the unperturbed potential, i.e. $\omega = s\Omega$, where $s \in \mathbb{N}$ (e.g. $s = 3$ for gray loops and $s = 5$ for red loops in Fig. 2.1).

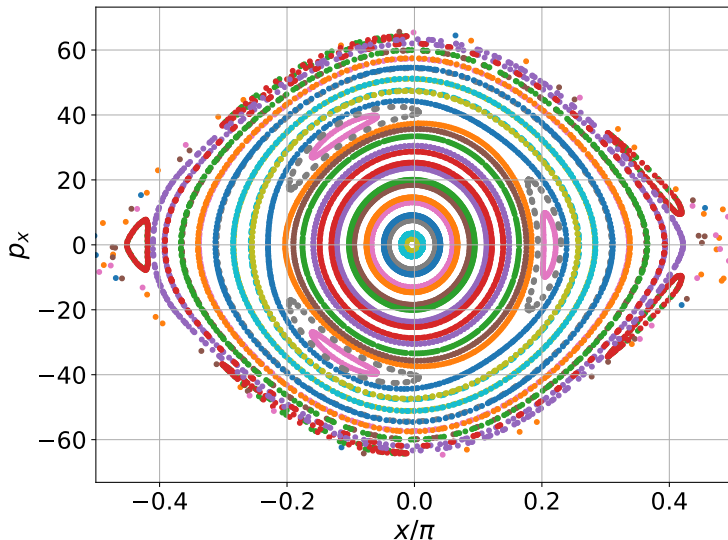


Figure 2.1: Stroboscopic phase space picture of a 1D driven system described by (2.3). The parameters used here are $\omega = 350$, $V_0 = 4320$ and $\lambda = 0.01$.

Concentrating on the $s = 3$ case in Fig. 2.1, the particle initially present at one of the three resonance islands will appear at the second one after a period T , at the third one after $2T$ and return to the initial island after $3T$. This gives the localized behavior that we set out to find, since on average, after each period the particle is localized at one of the three islands.

The resonant islands at each spatial potential well provide a localized structure needed for the construction of the lattice in the time domain.

2.1.2 Action-angle picture

Before we can apply the secular approximation which gives an effective description in the resonant region we are interested in, an intermediate step is required. A canonical change of variables will be applied to transform the x - p_x phase space into the so-called action-angle phase space that will lend itself to a more convenient description for the secular approximation.

The new canonical variables – action I and angle θ are introduced for the

stationary part of the Hamiltonian (2.3) denoted by

$$H_0(x, p_x) = p_x^2 + V_0 \sin^2(x). \quad (2.6)$$

Since we are interested in the periodic motion at a single potential well, we will concentrate on the case when the dimensionless energy $E = p_x^2 + V_0 \sin^2(x)$ of a particle is smaller than the potential amplitude V_0 , i.e. $E < V_0$. The action is defined to be proportional to the phase space area enclosed by a trajectory of energy E :

$$I(E) = \frac{1}{2\pi} \oint p_x(E) dx = \frac{2}{\pi} \int_0^{x_0} \sqrt{E - V_0 \sin^2(x)} dx, \quad (2.7)$$

where the second equality uses the fact that H_0 is symmetric with respect to both x and p_x , thus it is enough to integrate the first quadrant of the phase space and multiply it by four to obtain the whole area. $x_0 = \arcsin \sqrt{\frac{E}{V_0}}$ is the right classical turning point at which the momentum changes sign.

Angle θ is the conjugate coordinate to the action. It can be calculated using the generating function

$$S(x, I) = \int_{x_0}^x p_x(x', I) dx', \quad (2.8)$$

since it allows us to use the canonical relation

$$\theta(x, I) = \frac{\partial S(x, I)}{\partial I} = \frac{1}{2} \left(\frac{\partial I(E)}{\partial E} \right)^{-1} \int_{x_0}^x p_x^{-1}(x', I) dx'. \quad (2.9)$$

It is straightforward to obtain the equations of motions of the unperturbed Hamiltonian in the action-angle variables:

$$\begin{aligned} \frac{dI}{dt} &= -\frac{\partial H_0(I)}{\partial \theta} = 0, \\ \frac{d\theta}{dt} &= \frac{\partial H_0(I)}{\partial I}. \end{aligned}$$

Action is by definition a constant of motion thus it has no angle dependence. The angle evolution at some constant action I_1 is linear in time

$$\theta(t) = \left. \frac{\partial H_0(I)}{\partial I} \right|_{I_1} t + \theta(0), \quad (2.10)$$

where $\Omega(I_1) \equiv \left. \frac{\partial H_0(I)}{\partial I} \right|_{I_1}$ defines the natural frequency of an oscillating particle that has the energy $E(I_1)$. This will be useful during the derivation of the Hamiltonian under the secular approximation.

Finally, we can use the action-angle variables of the unperturbed problem

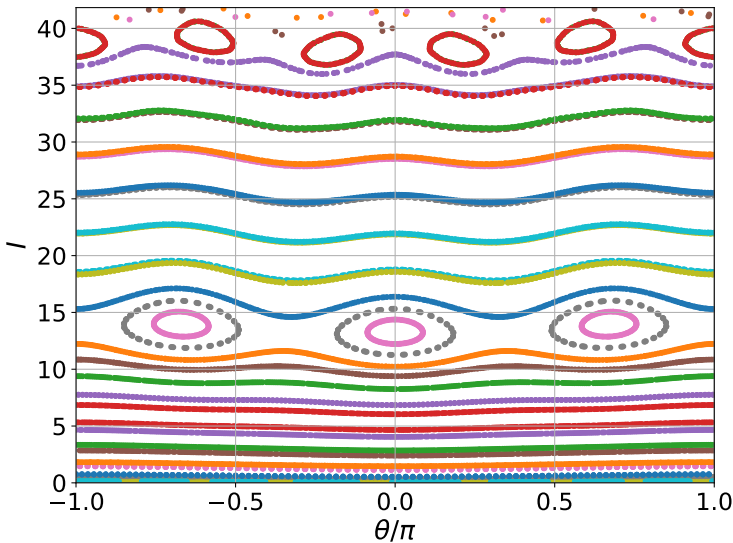


Figure 2.2: Stroboscopic phase space in action-angle variables of the same driven system as depicted in Fig. 2.1.

to map the solutions of the driven Hamiltonian to the action-angle phase space. This is done by taking the values of the $x - p_x$ phase space evaluated at integer multiples of the driving period T (as shown in Fig. 2.1) and associating each point to $\theta - I$ space by the equations (2.7) and (2.9). The resulting phase space is depicted in Fig. 2.2. What the transformation did is it "unwrapped" the angular part and rescaled the radial part of the $x - p_x$ space. The advantages that this representation offers are the improved discernibility of resonance islands as can be seen for the $s = 5$ case where the red islands became more prominent and it is easier to determine the resonant action values by inspection which will be needed to select the working point of the secular approximation.

Having introduced the action-angle variables we now have the complete set of tools necessary to build an effective description of a resonantly driven system around a particular high-order resonance by employing the secular approximation.

2.1.3 Classical secular approximation

Quantum mechanical calculations are usually computationally demanding and if we have a large parameter space that we want to probe it is often convenient to find an effective model of a system that would allow estimating the interesting parameter regions. To this end, the secular classical approximation will be introduced here. The main idea behind the secular approximation is that for a system driven close to the $s \in \mathbb{N}$ resonance, the dynamics are captured by

an effective time-independent (secular) Hamiltonian. This is done by taking the driven Hamiltonian (2.3) written in the action-angle coordinates, moving to a frame rotating at the resonant frequency and time averaging over the fast oscillating terms. These steps will be shown in detail in the following subsection.

The driven Hamiltonian in the action-angle variables is

$$H(\theta, I, t) = H_0(I) + p_x(\theta, I)\lambda\omega \sin(\omega t). \quad (2.11)$$

Moving to a rotating frame oscillating at natural frequency $\Omega = \frac{\omega}{s}$ can be done by performing a canonical transformation with the generating function $G_2 = I\left(\theta - \frac{\omega t}{s}\right)$. Then the new variables are $\Theta = \theta - \frac{\omega t}{s}$ and $\tilde{I} = I$ (the actions are identical thus we immediately drop the tilde from the notation) with the Hamiltonian in the rotating frame being

$$\tilde{H}(\Theta, I, t) = H_0(I) - \frac{\omega}{s}I + p_x\left(\Theta + \frac{\omega t}{s}, I\right)\lambda\omega \sin(\omega t). \quad (2.12)$$

Since momentum is a periodic quantity with respect to angle, it can be expanded into a Fourier series

$$p_x\left(\Theta + \frac{\omega t}{s}, I\right) = \sum_{n=-\infty}^{+\infty} p_n(I)e^{in\left(\Theta + \frac{\omega t}{s}\right)}. \quad (2.13)$$

The momentum expression is plugged into (2.12) and the Hamiltonian is averaged over a single driving period. The off-resonant modes get canceled out and we arrive at the secular Hamiltonian

$$H_{\text{sec}}(\Theta, I) = H_0(I) - \frac{\omega}{s}I - \lambda\omega|p_s(I)|\cos(s\Theta). \quad (2.14)$$

Our interest lies in the region around the resonance islands thus we expand the unperturbed Hamiltonian $H_0(I)$ around the resonant action I_s of the s resonance, where we expect to find the fixed points of the secular Hamiltonian. $H_0(I)$ is expanded up to the second order:

$$H_0(I) = H_0(I_s) + \frac{\partial H_0(I)}{\partial I}\Big|_{I_s}(I - I_s) + \frac{1}{2}\frac{\partial^2 H_0(I)}{\partial I^2}\Big|_{I_s}(I - I_s)^2 + O(I^3). \quad (2.15)$$

From the previous subsection we have that $\frac{\partial H_0(I)}{\partial I}\Big|_{I_s} = \Omega(I_s) = \frac{\omega}{s}$. Applying this to (2.14) we can finally write down the effective time-independent Hamiltonian

$$H_{\text{sec}}(\Theta, I) \approx H_{\text{eff}}(\Theta, I) \equiv \left[H_0(I_s) - \frac{\omega}{s}I_s\right] + \frac{P^2}{2m_{\text{eff}}} - V_{\text{eff}}\cos(s\Theta). \quad (2.16)$$

Here we defined the effective mass $m_{\text{eff}} \equiv \left(\frac{\partial^2 H_0(I)}{\partial I^2} \Big|_{I_s} \right)^{-1}$, potential $V_{\text{eff}} \equiv \lambda \omega |p_s(I)|$ and momentum $P \equiv I - I_s$. The first term in the brackets of Eq. (2.16) is constant and does not affect the dynamics therefore it is sometimes omitted.

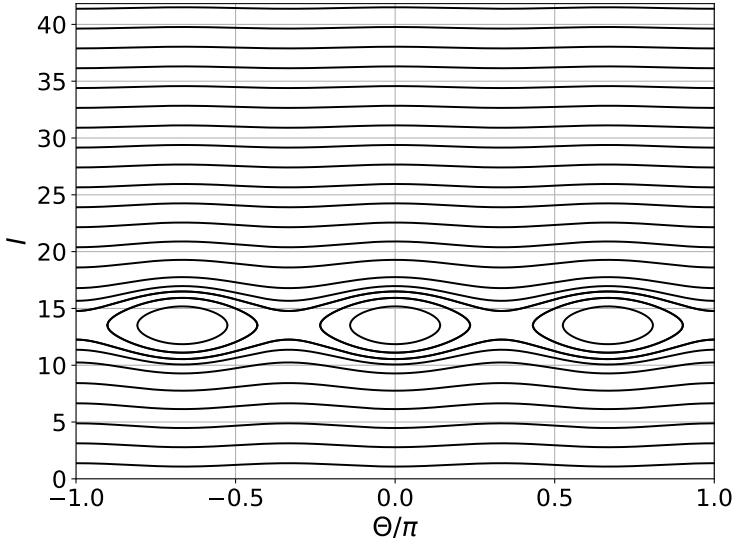


Figure 2.3: Phase space region of the effective secular Hamiltonian (2.16). The effective parameters are $m_{\text{eff}} = -0.83$ and $V_{\text{eff}} = 2.2$.

The effective secular Hamiltonian shows that the particles moving in a rotating frame act just like particles in an s -site lattice with a periodic boundary condition with respect to Θ . Each spatial site of the 1D driven lattice comes equipped with such a Θ periodic structure which acts as the discrete time dimension. This temporal part together with the spatially periodic potential wells form the 2D TSCS.

Let us put this effective Hamiltonian in action by considering the previously analyzed example in Fig. 2.1 and Fig. 2.2. Solving the equations of motion for the effective Hamiltonian near the $s = 3$ resonance we get the phase space diagram shown in Fig. 2.3 where the three resonant islands are reproduced. To ensure that the effective Hamiltonian provides a quantitatively correct description of the system, the obtained picture should be compared with Fig. 2.2. If the driving amplitude is sufficiently small, the stroboscopic phase space region is not distorted and the effective Hamiltonian approximation is valid.

This concludes the classical analysis of a periodically and resonantly driven 1D sine-squared potential. Driving at resonant frequencies creates a phase space structure that supports particle localization in the rotating frame of the

corresponding frequency. It is described by the effective secular Hamiltonian. This classical model will aid to estimate the parameters of a system needed to realize TSCS in the quantum regime and its quantized version will provide validity tests for the quantum computations which will be the topic of section 2.4.

2.2 Quantum analysis of a 1D driven potential

In this section, we turn to the quantum problem of the 1D driven sine-squared potential. The ideas of the previous section are utilized to derive the quantum secular Hamiltonian for this system. A 2D tight-binding model is obtained by using Wannier states constructed from the eigenstates of the driven Hamiltonian. The resulting tight-binding model will correspond to the 2D TSCS.

2.2.1 Floquet Hamiltonian

We begin with the canonically quantized version of the initial classical Hamiltonian (2.1). The Hamiltonian operator \hat{H} is given by:

$$\hat{H}(t) = \frac{\hat{p}_x^2}{2m} + V_0 \sin^2(k_L [\hat{x} - \lambda \cos(\omega t)]). \quad (2.17)$$

The position \hat{x} and momentum \hat{p}_x operators satisfy the canonical commutation relation $[\hat{x}, \hat{p}_x] = i\hbar$. A reminder that m is the mass of a particle, V_0 – trapping potential amplitude, k_L – lattice wavevector, λ – maximum displacement of the lattice in the x direction due to the driving and ω – shaking frequency. We can move to the oscillating frame by applying a unitary transformation $\hat{U}(t)$:

$$\tilde{\hat{H}}(t) = \hat{U}(t)\hat{H}(t)\hat{U}^\dagger(t) - i\hbar\hat{U}(t)\frac{d}{dt}\hat{U}^\dagger(t), \quad (2.18)$$

with $\hat{U}(t) = e^{i\frac{\lambda}{\hbar} \cos(\omega t)\hat{p}_x}$. It is equivalent to the canonical transformation we did in the classical case to separate the time and position dependent term. Plugging $\hat{U}(t)$ into (2.18) gives us

$$\tilde{\hat{H}}(t) = \frac{\hat{p}_x^2}{2m} + V_0 \sin^2(k_L \hat{x}) + \lambda\omega \sin(\omega t)\hat{p}_x. \quad (2.19)$$

The obtained Hamiltonian preserves both time and space periodicity. Expressing the equation in recoil energy units $E_R = \frac{\hbar^2 k_L^2}{2m}$ we get primed dimensionless quantities $\hat{p}'_x = \hat{p}_x/(\hbar k_L)$, $\hat{x}' = k_L \hat{x}$, $\hat{H}' = \tilde{\hat{H}}/E_R$, $V'_0 = V_0/E_R$, $\lambda' = \lambda k_L$, $\omega' = \hbar\omega/E_R$ and $t' = E_R t/\hbar$. Thus the dimensionless Hamiltonian is

$$\hat{H}(t) = \hat{p}'_x{}^2 + V_0 \sin^2(\hat{x}') + \lambda\omega \sin(\omega t)\hat{p}'_x, \quad (2.20)$$

where the primes have been dropped. This is the form of the Hamiltonian we will be working with.

It is convenient to define the Floquet Hamiltonian since the system is periodic in time:

$$\hat{\mathcal{H}}(t) = \hat{H}(t) - i\frac{\partial}{\partial t}.$$

The Floquet Hamiltonian has discrete coordinate translational symmetry therefore the eigenfunctions of the Floquet Hamiltonian are Bloch waves $\Phi_{k,\alpha}(x, t) = e^{ikx}u_{k,\alpha}(x, t)$, with functions $u_{k,\alpha}(x, t) = u_{k,\alpha}(x + \pi, t) = u_{k,\alpha}(x, t + \frac{2\pi}{\omega})$ periodic both in time and space. Here k is the dimensionless quasimomentum of the Bloch wave and α is a quantum number labeling the energy eigenvalue.

The eigenvalue problem consists of solving

$$\hat{\mathcal{H}}(t)\Phi_{k,\alpha}(x, t) = E_{k,\alpha}\Phi_{k,\alpha}(x, t), \quad (2.21)$$

where $E_{k,\alpha}$ are the eigenenergies. Finding $\Phi_{k,\alpha}(x, t)$ will provide the complete information about the single-particle system. Before attempting to solve the problem we simplify the equation by introducing a few eigenstate basis transformations. We start by inserting the explicit form of the Floquet Hamiltonian and Bloch functions into the eigenvalue equation and multiplying both sides by e^{-ikx} from the left

$$e^{-ikx} \left(\hat{p}_x^2 + V_0 \sin^2(\hat{x}) + \lambda\omega \sin(\omega t)\hat{p}_x - i\frac{\partial}{\partial t} \right) e^{ikx}u_{k,\alpha}(x, t) = E_{k,\alpha}u_{k,\alpha}(x, t). \quad (2.22)$$

The first and third terms can be simplified to

$$e^{-ikx}\hat{p}_x^2(e^{ikx}u_{k,\alpha}(x, t)) = (\hat{p}_x + k)^2 u_{k,\alpha}(x, t), \quad (2.23)$$

$$e^{-ikx}\lambda\omega \sin(\omega t)\hat{p}_x(e^{ikx}u_{k,\alpha}(x, t)) = \lambda\omega \sin(\omega t)(\hat{p}_x + k)u_{k,\alpha}(x, t). \quad (2.24)$$

This leads to the eigenvalue problem

$$\begin{aligned} & \left((\hat{p}_x + k)^2 + V_0 \sin^2(\hat{x}) + \lambda\omega \sin(\omega t)(\hat{p}_x + k) - i\frac{\partial}{\partial t} \right) u_{k,\alpha}(x, t) \\ & = E_{k,\alpha}u_{k,\alpha}(x, t). \end{aligned} \quad (2.25)$$

Applying the unitary transformation $\hat{U}_k(t) = e^{-i\lambda \cos(\omega t)k}$ on the left and inserting an identity element $\hat{U}_k^\dagger \hat{U}_k = 1$ into the equation

$$\begin{aligned} & \hat{U}_k \left((\hat{p}_x + k)^2 + V_0 \sin^2(\hat{x}) + \lambda\omega \sin(\omega t)(\hat{p}_x + k) - i\frac{\partial}{\partial t} \right) \hat{U}_k^\dagger \hat{U}_k u_{k,\alpha}(x, t) \\ & = E_{k,\alpha} \hat{U}_k u_{k,\alpha}(x, t), \end{aligned} \quad (2.26)$$

eliminates the oscillating term proportional to k . This is the way we arrive to the final form of the eigenvalue problem

$$\hat{\mathcal{H}}' u'_{k,\alpha}(x, t) = E_{k,\alpha} u'_{k,\alpha}(x, t), \quad (2.27)$$

where

$$\hat{\mathcal{H}}' = (\hat{p}_x + k)^2 + V_0 \sin^2(\hat{x}) + \lambda\omega \sin(\omega t) \hat{p}_x - i \frac{\partial}{\partial t} \quad (2.28)$$

and $u'_{k,\alpha}(x, t) = \hat{U}_k u_{k,\alpha}(x, t)$. Calculating $u'_{k,\alpha}(x, t)$ with the associated eigenenergies will provide all the necessary information because backtracking through the definitions we see that it relates to the eigenstate of the Floquet Hamiltonian by

$$\Phi_{k,\alpha}(x, t) = e^{ikx} u_{k,\alpha}(x, t) = e^{ikx} \hat{U}_k^\dagger(t) u'_{k,\alpha}(x, t) = e^{ikx} e^{i\lambda \cos(\omega t)k} u'_{k,\alpha}(x, t). \quad (2.29)$$

In this subsection we established the form of the quantum problem that describes the 1D driven system. In the following subsections we will proceed to solve it by employing the quantum secular approximation.

2.2.2 Time-independent Hamiltonian basis

We will solve the driven Hamiltonian problem in the stationary Hamiltonian $\hat{H}^{(0)}$ basis therefore we dedicate this subsection to finding the unperturbed eigenvectors of the eigenvalue problem $\hat{H}^{(0)} \psi_{k,n}(x) = E_{k,n}^{(0)} \psi_{k,n}(x)$. Here we will assume that the eigenbasis of $\hat{H}^{(0)}$ has the plane wave form $\psi_{k,n}(x) = \frac{1}{\sqrt{\pi}} \sum_{j=-\infty}^{+\infty} c_{k,j}^{(n)} e^{ig(j)x}$ where $g(j) = \frac{2\pi}{a_0} j$ is the 1D reciprocal lattice vector projection with $j \in \mathbb{Z}$ and the lattice constant is chosen to be $a_0 = \pi$. n labels the eigenstates and k is the quasimomentum. The complex coefficients $c_{k,j}$ are calculated numerically.

Given the unperturbed Hamiltonian

$$\hat{H}^{(0)} = (\hat{p}_x + k)^2 + V_0 \sin^2(\hat{x}), \quad (2.30)$$

the matrix elements of this operator in the exponential basis can be written as

$$H_{j',j}^{(0)} \equiv \int_{-\frac{\pi}{2}}^{\frac{\pi}{2}} e^{-i2j'x} \hat{H}^{(0)} e^{i2jx} dx. \quad (2.31)$$

Integrating over the lattice site we get

$$H_{j',j}^{(0)} = \left[(2j + k)^2 + \frac{V_0}{2} \right] \delta_{j,j'} - \frac{V_0}{4} [\delta_{j,j'-1} + \delta_{j,j'+1}], \quad (2.32)$$

where we have used the orthogonality of the basis $\int_{-\frac{\pi}{2}}^{\frac{\pi}{2}} e^{i2(j'-j)x} dx = \pi \delta_{j',j}$, $\delta_{j',j}$ being the Kronecker delta for $j', j \in \mathbb{Z}$. By diagonalizing the matrix com-

prised of elements of (2.32) we obtain the eigenvalues $E_{k,n}^{(0)}$ and the associated wavefunction coefficients $c_{k,j}^{(n)}$. Note that to diagonalize the Hamiltonian numerically, the number of basis elements $c_{k,j}^{(n)}$ needs to be truncated to a finite range of $j = -j_{\text{cutoff}}, \dots, j_{\text{cutoff}}$, $j_{\text{cutoff}} \in \mathbb{N}$. It is important to pick a large enough j_{cutoff} so that the description of the system in the resonant energy vicinity would be valid.

Now that we can numerically calculate the eigenstates of the time-independent Hamiltonian $\psi_{k,n}(x) = \frac{1}{\sqrt{\pi}} \sum_{j=-j_{\text{cutoff}}}^{j_{\text{cutoff}}} c_{k,j}^{(n)} e^{i2jx}$, we return to tackling the eigenproblem of the driven system.

2.2.3 Quantum secular approximation

The quantum secular approximation applied to the driven Hamiltonian will complete the description of the 1D driven system. Much like the classical secular approximation, the quantum version averages the Hamiltonian over a single driving period which neglects rapidly oscillating terms. The solution to the eigenvalue problem of the quantum secular Hamiltonian will provide the means to calculate the tunneling probabilities of particle densities between time-like and space-like lattice sites.

As in the classical case, we begin by moving to a frame rotating with the resonant frequency. This is done by applying the time-dependent unitary transformation on the unperturbed eigenfunctions derived in the previous subsection

$$\psi'_{k,n}(x, t) = e^{-in\frac{\omega}{s}t} \psi_{k,n}(x), \quad (2.33)$$

ω is the driving frequency and s is an integer labeling the $s : 1$ resonance. Using these functions as a basis for the Floquet Hamiltonian, the operator is written in matrix form with elements

$$\hat{\mathcal{H}}'_{n',n} \equiv \int_{-\frac{\pi}{2}}^{\frac{\pi}{2}} \psi'^*_{k,n'}(x, t) \hat{\mathcal{H}}' \psi'_{k,n}(x, t) dx. \quad (2.34)$$

We write out the elements explicitly

$$\hat{\mathcal{H}}'_{n',n} = \left(E_{k,n}^{(0)} - n\frac{\omega}{s} \right) \delta_{n',n} + \lambda\omega \sin(\omega t) e^{i(n'-n)\frac{\omega}{s}t} \int_{-\frac{\pi}{2}}^{\frac{\pi}{2}} \psi'^*_{k,n'}(x) \hat{p}_x \psi_{k,n}(x) dx \quad (2.35)$$

where the integral term can be expressed in the unperturbed Hamiltonian's wavefunction coefficients

$$\langle \psi_{k,n'} | \hat{p}_x | \psi_{k,n} \rangle \equiv \int_{-\frac{\pi}{2}}^{\frac{\pi}{2}} \psi^*_{k,n'}(x) \hat{p}_x \psi_{k,n}(x) dx = 2 \sum_{j=-j_{\text{cutoff}}}^{j_{\text{cutoff}}} j c_{k,j}^{(n')*} c_{k,j}^{(n)}. \quad (2.36)$$

Finally, we arrive at the quantum secular Hamiltonian by averaging (2.35) over

time, thus neglecting the fast oscillating terms:

$$\bar{\mathcal{H}}'_{n',n} = \left(E_{k,n}^{(0)} - n \frac{\omega}{s} \right) \delta_{n',n} + \frac{i\lambda\omega}{2} (\delta_{n',n+s} - \delta_{n',n-s}) \langle \psi_{k,n'} | \hat{p}_x | \psi_{k,n} \rangle. \quad (2.37)$$

The eigenvalue problem for this Hamiltonian $\bar{\mathcal{H}}' \bar{u}'_{k,\alpha} = \bar{E}_{k,\alpha} \bar{u}'_{k,\alpha}$ is solved numerically. The eigenstates of the quantum secular Hamiltonian $\bar{u}'_{k,\alpha}$ approximate the eigenstates of the Floquet Hamiltonian around the s resonance $u'_{k,\alpha} \approx \bar{u}'_{k,\alpha}$ with $E_{k,\alpha} \approx \bar{E}_{k,\alpha}$. The validity of this approximation is checked by computing the analogous quantized classical effective Hamiltonian and affirming that the energy spectrum is reproduced. This will be explicitly shown in subsection 2.4 when analyzing a specific example for the $s = 3$ case.

The periodic part of the Bloch-Floquet function $u'_{k,\alpha} \approx \bar{u}'_{k,\alpha}$ is the solution of the eigenvalue problem (2.27) we set out to find. It will be used to obtain localized Wannier functions which are the basis of the 2D TSCS tight-binding model.

2.2.4 Tight-binding model of a time-space crystal

The periodically driven 1D lattice considered in the previous sections can be described by a 2D tight-binding model which captures the essence of the 2D TSCS. We will obtain the hopping parameters that completely determine the dynamics of the system.

The first step is to construct localized Wannier functions that describe the system at the s resonance. This is done by diagonalizing the position operator \hat{x} with respect to the resonant Bloch-Floquet functions $\Phi_{k,\alpha}(x,t)$ (2.29), where the quantum number $\alpha^{(l)} = 1, \dots, s$ corresponds to the s resonant states. The matrix elements of this operator are

$$(\hat{x})_{k',\alpha';k,\alpha} = \int_{-\frac{\pi}{2}L}^{\frac{\pi}{2}L} \Phi_{k',\alpha'}^*(x,t) \hat{x} \Phi_{k,\alpha}(x,t) dx, \quad (2.38)$$

here L is the number of lattice sites. Note that (2.38) parametrically depends on the choice of time t and if at t the wavefunctions strongly overlap, the eigenvalues of the position operator might be degenerate which leads to eigenstates that are linear combinations of the Wannier functions. If this happens to be the case, an addition of a small time shift compared to the driving period should be enough to lift the degeneracy and resolve the orthogonal Wannier functions. Assuming the time t was chosen properly, diagonalization of the position operator allows us to obtain the Wannier functions [76]

$$w_{j,\alpha}(x,t) = \sum_{k,\beta} b_{k,\beta}^{j,\alpha} \Phi_{k,\beta}(x,t), \quad (2.39)$$

where the summation runs over all the quasi-momenta k and $\beta = 1, \dots, s$. Index $j = 1, \dots, L$ labels the spatial site on which the Wannier function is localized and α is the time-like dimension that indicates which temporal site is considered. The coefficients $b_{k,\beta}^{j,\alpha}$ are obtained from the numerical diagonalization of the position operator.

Using the tight-binding approximation we can construct a field operator $\hat{\phi}(x, t)$ in the orthogonal Wannier function basis

$$\hat{\phi}(x, t) = \sum_{j,\alpha} w_{j,\alpha}(x, t) \hat{a}_{j,\alpha}, \quad (2.40)$$

with $\hat{a}_{j,\alpha}$ being the particle annihilation operator for the indexed site. Then we get the tight-binding Hamiltonian in the second quantization form from the Floquet Hamiltonian of the system

$$\hat{H}_{\text{TB}} = \frac{1}{sT} \int_0^{sT} dt \int_{-\frac{\pi}{2}L}^{\frac{\pi}{2}L} \hat{\phi}^\dagger(x, t) \hat{\mathcal{H}}(t) \hat{\phi}(x, t) dx = -\frac{1}{2} \sum_{j',\alpha',j,\alpha} J_{j,\alpha}^{j',\alpha'} \hat{a}_{j',\alpha'}^\dagger \hat{a}_{j,\alpha}, \quad (2.41)$$

where the complex hopping parameter $J_{j,\alpha}^{j',\alpha'}$ here is defined as

$$J_{j,\alpha}^{j',\alpha'} = -\frac{2}{sT} \int_0^{sT} dt \int_{-\frac{\pi}{2}L}^{\frac{\pi}{2}L} w_{j',\alpha'}^*(x, t) \hat{\mathcal{H}}(t) w_{j,\alpha}(x, t) dx. \quad (2.42)$$

It can be simplified by using (2.21) and (2.39):

$$J_{j,\alpha}^{j',\alpha'} = -2 \sum_{k,\beta} E_{k,\beta} \left(b_{k,\beta}^{j',\alpha'} \right)^* b_{k,\beta}^{j,\alpha}, \quad (2.43)$$

$E_{k,\beta}$ are the quasi-energies of the initial Floquet Hamiltonian. The hopping parameter describes the tunneling of a particle from the temporal site α of spatial site j to a temporal site α' of spatial site j' . If all of the indices coincide, the term represents an on-site energy shift. This completes the description of the tight-binding model which corresponds to the 2D TSCS.

To summarize, we started with the Hamiltonian of a 1D driven lattice, applied the quantum secular approximation and used the obtained resonant eigenstates to build Wannier-like states that are localized spatially. This localization coupled together with the localization of states in the time dimension as seen from the resonant islands of the classical picture forms a 2D time-space crystalline structure. Due to the localized nature of these states, a tight-binding model derived in this subsection accurately captures the physics of the system. So far only single-particle physics was addressed in the preceding discussion, the next subsection will provide a brief look at how interactions can be included in this description.

2.2.5 Interactions

Although we will only consider the single-particle analysis of time-space crystalline structures throughout this chapter, it is worth mentioning that interactions can be easily described by the current framework as well.

To provide an example how interactions can be included, let us focus on a system that consists of bosons with contact interactions governed by a Dirac delta potential of strength g_0 proportional to the s-wave scattering length. We assume that the interactions are not strong enough to couple the resonant states to the rest of the states in the Hilbert space. This interaction term can be written as

$$\begin{aligned}\hat{H}_{\text{int}} &= \int_0^{sT} \frac{dt}{sT} \int dx \frac{g_0}{2} \hat{\phi}^\dagger(x, t) \hat{\phi}^\dagger(x, t) \hat{\phi}(x, t) \hat{\phi}(x, t) \\ &= \frac{1}{2} \sum_{j', \alpha', l', \beta'} \sum_{j, \alpha, l, \beta} U_{j, \alpha, l, \beta}^{j', \alpha', l', \beta'} \hat{a}_{j', \alpha'}^\dagger \hat{a}_{l', \beta'}^\dagger \hat{a}_{j, \alpha} \hat{a}_{l, \beta},\end{aligned}\quad (2.44)$$

with the interaction coefficient

$$U_{j, \alpha, l, \beta}^{j', \alpha', l', \beta'} = \int_0^{sT} \frac{dt}{sT} \int dx g_0 w_{j', \alpha'}^*(x, t) w_{l', \beta'}^*(x, t) w_{j, \alpha}(x, t) w_{l, \beta}(x, t), \quad (2.45)$$

where the introduced dummy indices $l^{(\prime)}$ and $\beta^{(\prime)}$ label spatial and temporal sites respectively. Typically the on-site interactions $U_{j, \alpha, j, \alpha}^{j, \alpha, j, \alpha}$ dominate for particles in the same wavepacket but long range interactions can be introduced as well by periodically modulating s-wave scattering length described by the term $g_0(t) = g_0(t + sT)$ in such a way that the interactions are increased when neighboring wavepackets on the same spatial site overlap. This would lead to a significant contribution of the interaction term $U_{j, \alpha, j, \beta}^{j, \alpha, j, \beta}$.

The interaction term together with the tight-bind Hamiltonian form a Hubbard-type model as discussed in subsection 1.1.3. Being able to formulate the description of time-space crystalline structures in this framework provides the tools to probe well-known many-body condensed matter phenomena in the time domain [24, 150, 156].

We have established the construction of time-space crystalline structures and now with the inclusion of interactions we conclude the basic theoretical description of a 2D TSCS.

2.3 Higher dimensional time-space crystalline structures

A straightforward way to generalize a 2D time-space crystalline structure to higher dimensions is to consider a system that consists of two or three reso-

nantly driven 1D sine-squared potentials that are orthogonal to each other in terms of spatial directions. Each of these 1D potentials comes equipped with a temporal degree of freedom, therefore a 2D (3D) spatial potential would allow the creation of a 4D (6D) TSCS. Let us proceed by explicitly constructing the tight-binding model of a 6D time-space crystalline structure.

Recall that the system with a driven 1D sine-squared potential is described by the Hamiltonian (2.20) in the oscillating frame:

$$\hat{H}_q(t) = \hat{p}_q^2 + V_0 \sin^2(\hat{q}) + \lambda\omega \sin(\omega t)\hat{p}_q. \quad (2.46)$$

We have introduced $q \in \{x, y, z\}$ to distinguish the spatial directions x , y and z along which the driving is conducted in the lab frame. This allows us to write the Hamiltonian corresponding to a 3D spatial lattice as

$$\hat{H}^{3D}(t) = \hat{H}_x(t) + \hat{H}_y(t) + \hat{H}_z(t). \quad (2.47)$$

It is a separable Hamiltonian therefore we can obtain the Wannier functions $w_{j_q, \alpha_q}(q, t)$ for each direction q independently. The product of these functions is a Wannier function of the spatially 3D system:

$$W_{\vec{j}, \vec{\alpha}}(\vec{r}, t) = w_{j_x, \alpha_x}(x, t)w_{j_y, \alpha_y}(y, t)w_{j_z, \alpha_z}(z, t). \quad (2.48)$$

Here the vector quantities are defined as $\vec{r} = (x, y, z)$, $\vec{j} = (j_x, j_y, j_z)$ and $\vec{\alpha} = (\alpha_x, \alpha_y, \alpha_z)$. The 3D spatial lattice sites are labeled by \vec{j} and the time domain sites are indexed by $\vec{\alpha}$ with components $a_q \in \{1, \dots, s\}$ for all q , s being the resonance number. We see that the Wannier function $W_{\vec{j}, \vec{\alpha}}(\vec{r}, t)$ has six degrees of freedom corresponding to each of the component of \vec{j} and $\vec{\alpha}$. It forms the basis of the 6D time-space crystalline structure which can be visualized as a 3D spatial lattice where each individual site hosts an additional $s \times s \times s$ temporal lattice.

Once the Wannier functions are obtained, the same procedure as in subsection 2.2.4 can be followed to construct the tight-binding model. For a resonantly driven system, the field operator $\hat{\phi}(\vec{r}, t)$ can be expressed in the Wannier basis as

$$\hat{\phi}(\vec{r}, t) = \sum_{\vec{j}, \vec{\alpha}} W_{\vec{j}, \vec{\alpha}}(\vec{r}, t) \hat{a}_{\vec{j}, \vec{\alpha}}. \quad (2.49)$$

The tight-binding Hamiltonian in second quantization is then derived to be

$$\begin{aligned} \hat{H}_{\text{TB}} &= \frac{1}{sT} \int_0^{sT} dt \int dx \int dy \int dz \phi^*(\vec{r}, t) \left(\hat{H}^{3D}(t) - i \frac{\partial}{\partial t} \right) \phi(\vec{r}, t) \\ &= -\frac{1}{2} \sum_{\vec{j}', \vec{\alpha}', \vec{j}, \vec{\alpha}} J_{\vec{j}, \vec{\alpha}}^{\vec{j}', \vec{\alpha}'} \hat{a}_{\vec{j}', \vec{\alpha}'}^\dagger \hat{a}_{\vec{j}, \vec{\alpha}}, \end{aligned} \quad (2.50)$$

where the spatial integrals are integrated over a single site. We see that the form of the Hamiltonian remains the same as in Eq. (2.41), except now we have to sum over all the components of vectors \vec{j} and $\vec{\alpha}$ indexing the sites. The hopping parameters in this case are

$$J_{\vec{j},\vec{\alpha}}^{\vec{j}',\vec{\alpha}'} = -\frac{2}{sT} \int_0^{sT} dt \int dx \int dy \int dz W_{\vec{j}',\vec{\alpha}'}^*(\vec{r},t) \left(\hat{H}^{3D}(t) - i\frac{\partial}{\partial t} \right) W_{\vec{j},\vec{\alpha}}(\vec{r},t). \quad (2.51)$$

This expression can be simplified by using the orthogonality of the Wannier functions at each moment of time, that is

$$\int dx' w_{j_i,\alpha_i}^*(x',t) w_{j'_i,\alpha'_i}(x',t) = \delta_{j'_i,j_i} \delta_{\alpha'_i,\alpha_i}, \quad (2.52)$$

when integrating along the i direction. Employing the aforementioned orthogonality and the notation of 1D tunneling parameters (2.42) for the three orthogonal spatial dimensions, the 6D time-space lattice hopping parameters are expressed as

$$\begin{aligned} J_{\vec{j},\vec{\alpha}}^{\vec{j}',\vec{\alpha}'} &= J_{j_x,\alpha_x}^{j'_x,\alpha'_x} \delta_{j'_y,j_y} \delta_{\alpha'_y,\alpha_y} \delta_{j'_z,j_z} \delta_{\alpha'_z,\alpha_z} + J_{j_y,\alpha_y}^{j'_y,\alpha'_y} \delta_{j'_z,j_z} \delta_{\alpha'_z,\alpha_z} \delta_{j'_x,j_x} \delta_{\alpha'_x,\alpha_x} \\ &+ J_{j_z,\alpha_z}^{j'_z,\alpha'_z} \delta_{j'_x,j_x} \delta_{\alpha'_x,\alpha_x} \delta_{j'_y,j_y} \delta_{\alpha'_y,\alpha_y}. \end{aligned} \quad (2.53)$$

We see that tunneling occurs independently in each direction as expected for a system with a separable Hamiltonian. So if the 2D TSCS tight-binding problem is solved, the higher dimensional tight-binding model is readily available in this considered case. The interactions can also be included in the same manner as in subsection 2.2.5 to construct Hubbard-type models for 6D time-space crystalline structures.

The simple setup of driving three spatially orthogonal potentials described in this section creates a system that is up to six-dimensional. Thus time-space crystalline structures can be an alternative to systems with synthetic dimensions [41, 42] which utilize the internal degrees of the constituents (e.g. spin degree of freedom of atoms) to probe higher-dimensional physics.

2.4 Case study: driven sine-squared lattice at $s = 3$ resonance

The developed theoretical tools that describe a 2D TSCS are applied to a periodically driven 1D sine-squared lattice of $L = 5$ spatial sites at the $s = 3$ resonance. We select a working point by fixing a set of parameters that describe the system and analyze the validity of the secular approximation. After asserting that the results are valid within the approximation, the tight-

binding model is used to determine the geometry of the system and a plausible experimental scheme is suggested.

2.4.1 Parameter selection

Let us start with the classical Hamiltonian (2.3):

$$H(x, p_x, t) = p_x^2 + V_0 \sin^2(x) + p_x \lambda \omega \sin(\omega t),$$

the parameters that we are free to choose are the potential amplitude V_0 , angular driving frequency ω and spatial driving amplitude λ (reminder that dimensionless units are used here). Since our interest lies in the $s = 3$ resonance we scan the parameter space to find the single spatial site phase-space portraits with three resonant islands present (e.g. the islands shown by grey points in Fig. 2.1 or Fig. 2.2). If the classical secular Hamiltonian is used to scan the parameters, one needs to check if the final choice satisfies the assumptions of the secular approximation by comparing the obtained result to the exact solution of the equations of motion.

Once the s resonance islands are located, further parameter tuning is done to adjust the position and the area of the islands in the phase space. In the quantum problem, we want to induce tunneling between neighboring spatial lattice sites for some resonant states therefore it is reasonable to choose such parameters that maximize the overlap of their Wannier functions. Classically this corresponds to a system where the s resonance energy is located near the top of the driven potential. Such a selection minimizes the distance between the classical turning points of neighboring sites which allows favorable tunneling in the quantum case. The other important condition is that the area of an individual resonant island has to be larger or at least comparable to the quanta of the analyzed quantum system in order to observe quantum effects. In the driven lattice case with dimensionless units, we had the canonical commutation relation given by $[\hat{x}, \hat{p}_x] = i$, which means the area of the island in x - p_x phase space has to be larger than one.

It is often useful to employ the scaling relations for the variables of the system to reduce the number of parameters which need to be varied to scan the parameter space. For our driven system, one of the parameters can be fixed while others are tuned until the resonance islands are obtained. After selecting the working point, scaling allows us to adjust the size of the islands while maintaining the equations of motion the same up to a constant. To state this explicitly, let η be a scaling parameter, then the scaled values of the classical Hamiltonian can be written as

$$\begin{aligned} \bar{x} &= \eta^a x, & \bar{p}_x &= \eta^b p_x, & \bar{V}_0 &= \eta^c V_0, & \bar{\omega} &= \eta^d \omega, \\ \bar{\lambda} &= \eta^e \lambda, & \bar{t} &= \eta^f t, & \bar{H} &= \eta^g H. \end{aligned} \tag{2.54}$$

Here the exponents denoted by Latin letters a to g define the scaling law of each parameter. To determine these laws we plug in the scaled parameters into the Hamilton equations of Hamiltonian (2.3)

$$\begin{aligned}\eta^{b-f} \frac{dp_x}{dt} &= -\eta^c V_0 \sin(2\eta^a x), \\ \eta^{a-f} \frac{dx}{dt} &= 2\eta^b p_x + \eta^{e+d} \lambda \omega \sin(\eta^{d+f} \omega t),\end{aligned}$$

and the Hamiltonian itself

$$\eta^g H = \eta^{2b} p_x^2 + \eta^c V_0 \sin^2(\eta^a x) + \eta^{b+e+d} p_x \lambda \omega \sin(\eta^{d+f} \omega t).$$

The requirement for the equations of motion to remain the same up to a scalar multiplier implies that the exponents obey the following relations: $a = e = 0$, $c = g = 2b$, $d = b$ and $f = -b$, as seen from the equations above. The exponent b is set to $b = 1$ since its choice is arbitrary and it can be absorbed into the definition of η , then the final scaling relations are

$$\begin{aligned}\bar{x} &= x, & \bar{p}_x &= \eta p_x, & \bar{V}_0 &= \eta^2 V_0, & \bar{\omega} &= \eta \omega, \\ \bar{\lambda} &= \lambda, & \bar{t} &= \eta^{-1} t, & \bar{H} &= \eta^2 H.\end{aligned}\tag{2.55}$$

An important point to note here is that the scaling applied to the classical case does not respect the scaling of the canonical quantization commutator. When the commutator given in the scaled operators $[\hat{\bar{x}}, \hat{\bar{p}}_x] = i$ is re-expressed in terms of the original operators $[\hat{x}, \hat{p}_x] = \eta^{-1} i$ we see that scaling changes the effective quanta of the system. The effective dimensionless Planck constant becomes η^{-1} instead of the unit value it had before, thus for large η it becomes easier to attain big enough resonant islands that support quantum effects.

Having described the guidelines of parameter selection, we follow the discussion above and choose the values that provide an illustrative example of a system with three resonant islands. After scanning the parameter region we set the potential to $V_0 = 4320$ and the driving frequency to $\omega = 240$. To select the driving amplitude one has to keep in mind that it has to be sufficiently small to ensure the validity of the secular approximation. Let us look at the phase space pictures of the system in Fig. 2.4 for two choices of the driving amplitude – $\lambda = 0.01$ and $\lambda = 0.025$. In the first row of the figure we have the action-angle phase space picture of the effective classical Hamiltonian (2.16) for both of the amplitudes (left – $\lambda = 0.01$, right – $\lambda = 0.025$). Looking at these solutions obtained from the effective Hamiltonian one could assume that amplitude $\lambda = 0.025$ is the favorable choice since it provides larger resonant islands and smaller distances between turning points of neighboring sites. However, if the classical equations of motion are solved exactly we see that this is not the case. The bottom row of Fig. 2.4 depicts the phase space of

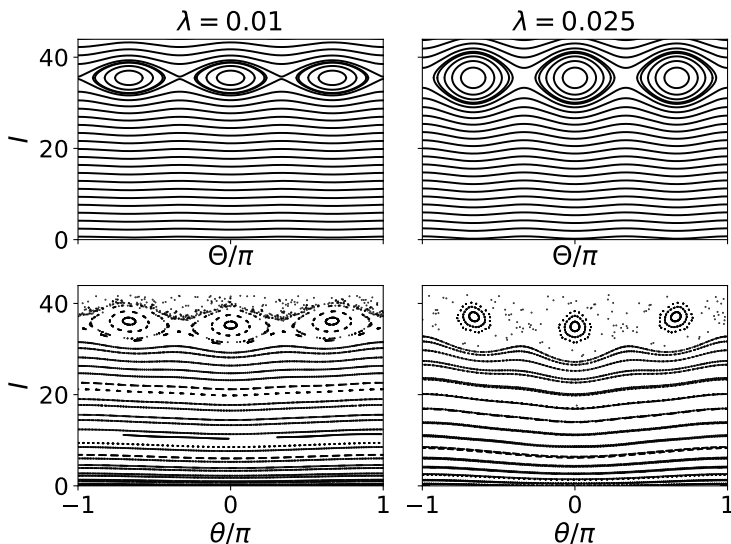


Figure 2.4: Top panels: Action-angle phase space picture of a single spatial lattice site calculated from the equations of motion of the effective classical Hamiltonian (2.16) for $V_0 = 4320$ and $\omega = 240$ with $\lambda = 0.01$ (left) and $\lambda = 0.025$ (right). Bottom panels: stroboscopic phase space pictures obtained by numerically integrating the exact equations of motion of the classical Hamiltonian (2.3). The parameters used for the bottom pictures are the same as the ones used for the pictures directly above them.

the exact solutions of the equations of motion for the same parameters as the plots above them. We see that the exact results and the approximate solution match qualitatively well for $\lambda = 0.01$. For $\lambda = 0.025$ the exact solution reveals that the amplitude is too large and the approximation is invalid – most of the area of the resonance islands predicted by the effective classical Hamiltonian is actually in the chaotic region of the exact solution space and the islands are too small to support quantum states. Therefore for further calculations the driving amplitude $\lambda = 0.01$ is chosen.

The classical framework provides a useful tool to efficiently probe the parameter space for time-space crystalline structure candidates. In this subsection the general ideas of the selection process have been walked through and illustrated by an example that shows the selection of a working point for a system with three resonant islands. In the following subsections, we will calculate the properties of such a system in the quantum case using the selected parameters.

2.4.2 Validity of the quantum secular Hamiltonian

In subsection 2.2.3 we have derived the quantum secular Hamiltonian that captures the properties of a resonantly driven system in the vicinity of $s : 1$

resonance. Before using this description to obtain the relevant information about the system one needs to assert the validity of the quantum secular approximation. Since the classical effective Hamiltonian reproduces the correct phase space trajectories of the analyzed system at the chosen working point, we expect that the correct energy spectra will be observed for the quantized version of the classical effective Hamiltonian. Therefore the validity is checked by comparing the eigenenergies obtained from the quantum secular Hamiltonian (2.37) with the energy spectrum calculated from the quantized effective classical Hamiltonian (2.16).

Let us begin by quantizing the effective classical Hamiltonian. The canonical quantization is performed by promoting the canonical coordinates of momentum $P \equiv (I - I_s)$ which is proportional to action and coordinate Θ – the angle into corresponding operators \hat{P} and $\hat{\Theta}$ that satisfy the commutation relation $[\hat{\Theta}, \hat{P}] = i$. Then the quantized classical Hamiltonian can be written as

$$\hat{H}_{\text{eff}} = \frac{\hat{P}^2}{2m_{\text{eff}}} - V_{\text{eff}} \cos(s\hat{\Theta}) + \text{const.}, \quad (2.56)$$

where the constants are defined as in subsection 2.1.3.

We now consider the system discussed in the previous subsection described by this Hamiltonian. For the chosen working point at $s = 3$ we use the definitions of the effective parameters to get the effective mass $m_{\text{eff}} = -0.368$ and effective potential $V_{\text{eff}} = 10.1$ at resonant action $I_s = 35.5$. Negative effective mass implies that the energy spectrum will be bounded from above as seen from the first term of the Hamiltonian – the negative sign flips the spectrum obtained from the square of the momentum which is bounded from below by zero. The consequence of this is that the ground state of the system corresponds to the highest energy of the spectrum, the first excited state – the second-highest energy value, and so on. It is straightforward to calculate the energy spectrum by diagonalizing \hat{H}_{eff} written in the plane wave basis as it was done in section 2.2.2 for a Hamiltonian of similar form. The calculated energies $E_{\text{classical}}$ (red dashed lines) are plotted for a range of driving amplitudes λ in Fig. 2.5.

To establish a comparison between the spectra, we proceed to calculate the eigenenergies of the quantum secular Hamiltonian with matrix elements written in the plane wave basis (2.37):

$$\bar{\mathcal{H}}'_{n',n} = \left(E_{0,n}^{(0)} - n \frac{\omega}{s} \right) \delta_{n',n} - \frac{i\lambda\omega}{2} (\delta_{n',n-s} - \delta_{n',n+s}) \langle \psi_{0,n'} | \hat{p}_x | \psi_{0,n} \rangle.$$

Here the quasimomentum is set to $k = 0$ since we compare the single spatial site results of both descriptions. The resulting energies $E_{0,\alpha}$ are shown as black lines in Fig. 2.5 as functions of driving amplitude λ .

Inspecting Fig. 2.5 we focus on the three highest energy levels which cor-

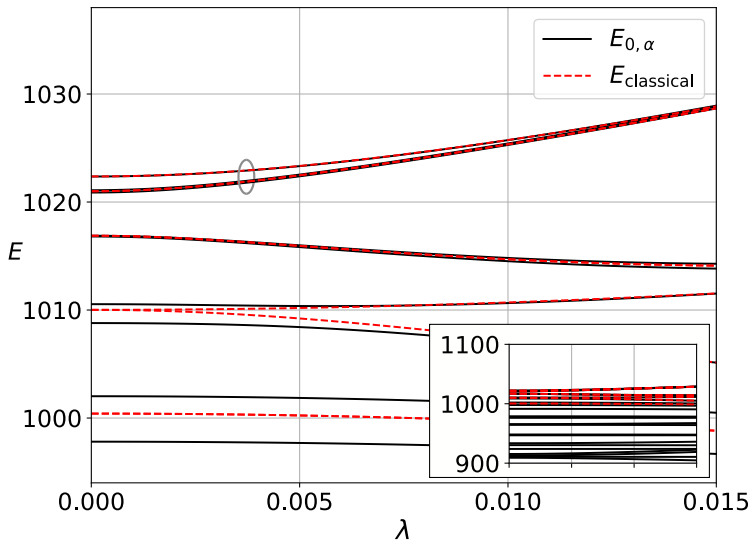


Figure 2.5: Energy levels of the quantized effective classical Hamiltonian (red dashed lines) and the quantum secular Hamiltonian (black lines) over a range of driving amplitudes λ . The parameters used for the quantum secular approximation case are $V_0 = 4320$ and $\omega = 240$; for the quantized effective classical case – $m_{\text{eff}} = -0.368$, $V_{\text{eff}} = 10.1$ and $I_s = 35.5$. The grey loop encircles the energy levels corresponding to the resonant eigenstates. Inset depicts a zoomed out picture of the spectra for the same interval of driving amplitudes.

respond to the $s = 3$ resonant states we are interested in. These three energy levels are indicated by a grey loop that encloses them. The first two excited levels are nearly degenerate thus visually it appears that there are only two curves encircled instead of three. The inset shows a wider range of energies and the same range of driving amplitudes to emphasize that we are indeed looking at the upper bound of the spectrum.

Comparing the energies obtained from the quantized effective classical Hamiltonian and quantum secular Hamiltonian we see that the encircled energy levels of interest match perfectly in a wide range of driving amplitudes, therefore we can assert that the quantum secular description is valid.

The quantum secular description reproduces the eigenenergies corresponding to the quantized effective classical results for a single site. Using this as validation that the quantum secular approximation gives the correct physical description we will proceed by building the Wannier functions and determining the hopping parameters in this framework.

2.4.3 Quasi-one-dimensional time-space crystalline structure

We are finally ready to construct an example of a time-space crystalline structure described by the quantum secular approximation. Let us consider a quasi-one-dimensional system with L spatial sites (labeled $j = 1, \dots, L$) and three temporal sites (indexed $\alpha = 1, 2, 3$) at each spatial site created by periodic resonant driving. The system is described by the quantum secular Hamiltonian (2.37) with parameters $V_0 = 4320$, $\omega = 240$ and $\lambda = 0.01$. Imposing the periodic boundary condition in the spatial direction we get the quasimomentum values $k \in \{\frac{m}{L} - \frac{1}{2} \mid m \in \{1, \dots, L\}\}$, where the assumption that the lattice constant is $a_0 = \pi$ is used.

Recalling the results derived in subsections 2.2.3 and 2.2.4, we numerically solve the eigenvalue problem to obtain the resonant Bloch-Floquet states $\Phi_{k,\beta}(x, t) = e^{ikx}u_{k,\beta}(x, t) = e^{ikx}e^{i\lambda \cos(\omega t)k}u'_{k,\beta}(x, t)$ of the driven lattice. The highest energy eigenstates are labeled by $\beta \in \{1, 2, 3\}$. They are used to construct the Wannier states $w_{j,\alpha}(x, t)$ – wavepackets that correspond to temporal sites at each spatial site.

Let us concentrate on three out of L spatial sites in the lattice and observe how the densities of some of these states behave when evolved in time in the lab frame (Fig. 2.6). Panels (a) to (c) depict the system at three different times. The initial time for panel (a) corresponding to the phase $\omega t = \pi/5$ is chosen in such a way to ensure that no Bloch-Floquet states overlap identically thus the Wannier functions are constructed correctly (see discussion in subsection 2.2.4). Panel (b) shows how the densities of the states have evolved after half of the driving period ($\omega t = \pi/5 + \pi$) and (c) depicts the density after the full driving period ($\omega t = \pi/5 + 2\pi$). The density of one of the periodic Floquet states $|e^{ikx}u_{k,\beta}(x, t)|^2$ is plotted at $k = 0$ as a function of position x (black curve). It illustrates that the Floquet states respect the periodicity of the driven Hamiltonian – after a single driving period T the state has completed a single oscillation and the final density of the state in panel (c) matches the density of the initial state of panel (a). The colored dashed curves are the densities of Wannier states localized on each of the spatial sites. Only one out of three Wannier states per site is plotted, the remaining two are omitted to not clutter the plot. We see that the Wannier states do not return to the initial position after a single period, in fact, it takes three periods for the localized packets to complete the oscillation and return to their initial distribution. This is consistent with the classical description in 2.1.1 where we have seen from the stroboscopic picture of the x - p_x phase-space that if the system is initially in one of the s resonance islands, it takes sT to return to its initial island.

The obtained Wannier states act as a basis for an effectively 2D lattice which consists of L spatial and s temporal sites. If $s \ll L$ we can claim that

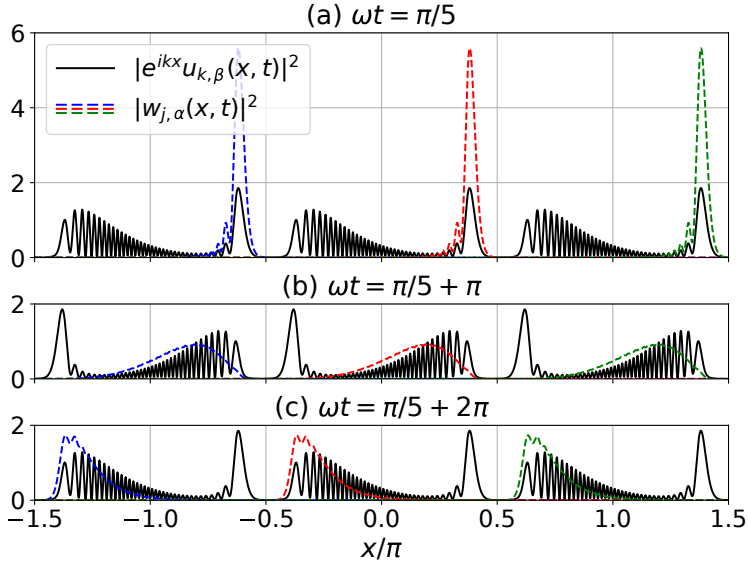


Figure 2.6: Probability density of the highest energy resonant Bloch-Floquet state at $k = 0$ (black curve) and probability densities of Wannier states (dashed colored lines) as functions of coordinate. The functions are depicted at three instances of time which correspond to phases: (a) $\omega t = \pi/5$, (b) $\omega t = \pi/5 + \pi$ and (c) $\omega t = \pi/5 + 2\pi$. Three spatial lattice sites are shown. Only one out of three Wannier states per site is plotted.

a lattice is quasi-one-dimensional. This is our case, since $s = 3$, meaning that we only have three resonant states available per spatial site. To determine the exact geometry of the lattice the tunneling parameters must be computed – the tunneling amplitude between the sites will show which hoppings are relevant for the description of the system and which can be neglected. Since we have already calculated the Wannier states, it is straightforward to calculate the hopping parameters $J_{j,\alpha}^{j',\alpha'}$ of our lattice using the previously derived result (2.42):

$$J_{j,\alpha}^{j',\alpha'} = -\frac{2}{sT} \int_0^{sT} dt \int_{-\frac{\pi}{2}L}^{\frac{\pi}{2}L} w_{j',\alpha'}^*(x, t) \hat{\mathcal{H}}(t) w_{j,\alpha}(x, t) dx,$$

where $\hat{\mathcal{H}}(t)$ is the Floquet Hamiltonian of the system. $J_{j,\alpha}^{j',\alpha'}$ describes the tunneling amplitude of a particle hopping from site indexed by spatial and temporal labels (j, α) to a site (j', α') .

Numerical calculations reveal that for the current choice of parameters we have the triangular geometry of the lattice as shown in Fig. 2.7. The lattice sites are depicted by colored circles, the x -axis corresponds to spatial dimension sites and y -axis – to the time domain sites i.e. the wavepackets moving in a single

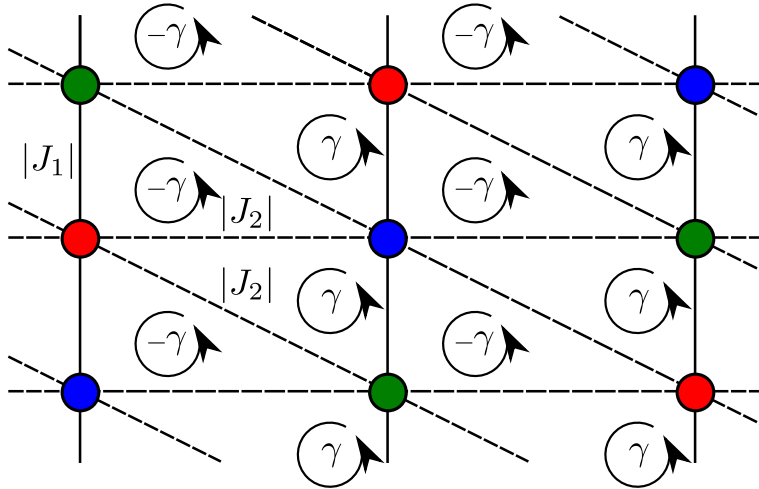


Figure 2.7: A lattice depiction of the quasi-one-dimensional time-space crystalline structure with parameters $V_0 = 4320$, $\omega = 240$ and $\lambda = 0.01$. x axis corresponds to the spatial dimension and time domain sites are index in the y direction. Colors indicate which time domain wavepackets have matching phase before time averaging. $|J_1|$ and $|J_2|$ are absolute values of hopping parameters between sites connected by corresponding solid and dashed links. γ is the flux piercing the plaquettes.

spatial lattice site. There is no implicit ordering of the time domain sites thus we take an arbitrary time point t and in Fig. 2.7 assign a color to each wavepacket that has matching phase. E.g. the red sites of Fig. 2.7 could correspond to the three Wannier functions of Fig. 2.6(a) which have the same phase. Once the color is assigned at time t , we assume that the labeling α of Wannier function $w_{j,\alpha}(x, t)$ by that color is inherited for all times t . The lattice sites are linked by lines that represent tunneling between the connected sites. There are two sets of dominant hoppings: $|J_1| \approx 0.25$ – tunneling purely between time domain sites (solid lines) and $|J_2| \approx 0.015$ – tunneling between spatial lattice sites (dashed lines). Tunneling terms of order 10^{-3} and smaller are neglected. From the calculated hopping parameters we learn that the lattice is periodic in the temporal direction – this is no surprise because the three wavepackets on each spatial site oscillate periodically and the particles can tunnel between them when the Wannier functions overlap. Since these oscillating wavepackets are a property of time-space crystalline structures, these periodic boundaries are a general result for any s resonance system described by a Hamiltonian of the form (2.20). The periodicity is depicted by open-ended vertical solid and diagonal dashed lines at the top and bottom of the lattice in Fig. 2.7. The open-ended lines to the right and left of the lattice indicate that we are looking only at a portion of a lattice that extends for L sites. The final information that is shown in the picture is the flux γ piercing the triangular lattice plaquettes.

It is the phase accumulated by the wavefunction after it traveled around the closed plaquette counterclockwise and returned to its origin (shown by circular arrows). We see that the sign of γ alternates from plaquette to plaquette forming a so-called staggered flux. An additional flux forms if we loop around the periodic dimension of the system, i.e. a non-zero flux forms when the wavefunction is dragged around the three time domain sites on a single spatial site (not shown in the figure). It is important to stress that the staggered flux is not a general result but a consequence of the choice of our current working point. In general, tuning the parameters will modify both the flux and the geometry of the hoppings of the system. To introduce flux in a more controlled fashion an additional potential driving term has to be introduced, this will be discussed in section 2.5.

Here we have constructed an example of a quasi-one-dimensional time-space crystalline structure. After discussing the general strategy of parameter selection and choosing a working point, we applied the ideas of sections 2.1 and 2.2 to check the validity of the quantum secular description. Finally, we discussed how to determine the geometry of a given system and provided an explicit example for a particular choice of parameters.

2.4.4 Experimental scheme

Having obtained the hopping parameters for the time-space crystalline structure we can evaluate the viability of creating it experimentally and propose a loading scheme to prepare the resonant wavepackets which make up the time-space lattice.

Typically the numerically obtained tunneling amplitudes in the spatial direction are of the orders $|J_{j,\alpha}^{j+1,\alpha}| \sim 10^{-3} \div 10^{-2}$. If we consider that our system consists of Rubidium ^{87}Rb atoms and a $10.6 \mu\text{m}$ CO_2 lattice laser [157] then we get that the calculated hoppings are larger than the incoherent scattering rate ($J > \hbar\Gamma_{\text{sc}}/E_{\text{R}}$) by one or two orders of magnitude [65]. This ensures that there is sufficient time to observe the relevant dynamics of the system in an experimental run.

The preparation of the resonant wavepackets is schematically depicted in Fig. 2.8. The idea is to prepare ground states of an auxiliary superlattice that would resemble the structure of desired resonant states, then release them into a shaken lattice where they should follow the predicted resonant behavior. Similar approaches were considered and evaluated in Refs. [147, 158]. Initially, in Fig. 2.8(a) a superlattice (black curve) is constructed to host ground state densities (colored curves) at each of the narrow potential wells. The potential is chosen so that the width of these densities matches the width of the Wannier function densities $|w_{j,\alpha}|^2$ at the turning point of the wavepackets. The next step shown in Fig. 2.8(b) consists of turning off the superlattice (dashed black

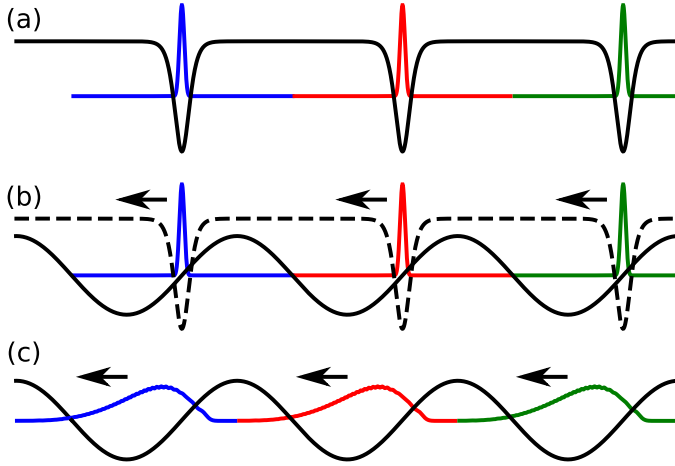


Figure 2.8: Time-space lattice loading procedure. (a) Auxiliary lattice (black curve) used to prepare ground states (colored lines) corresponding to resonant states at each well. (b) Driven lattice is turned on (solid black curve) and auxiliary lattice is turned off (dashed black curve) allowing the ground states to propagate from the turning point at $\omega t = \frac{\pi}{5}$. (c) States after evolving to $\omega t = \frac{\pi}{5} + \pi$. Arrows indicate the direction of wavepacket propagation.

curve) and turning on the periodically driven lattice (solid black curve) whose minima are offset from the initial positions of the prepared ground state. At this point, the ground states can be identified with the Wannier states depicted in Fig. 2.6(a) at $\omega t = \frac{\pi}{5}$. The arrows indicate the propagation direction of the released ground states. Fig. 2.8(c) presents that released ground states follow the path of the predicted resonant states at the time $\omega t = \frac{\pi}{5} + \pi$ as in Fig. 2.6(b). This procedure populates one of the time-like branches of the time-space crystalline lattice. To populate all of the branches the procedure needs to be repeated every driving period T until the lattice is filled.

Following the provided loading protocol should allow in principle to realize a time-space crystalline structure. The typical hopping parameters are sufficiently large to overcome the loss effects due to the incoherent scattering during an experiment's time frame.

2.5 Engineering artificial magnetic flux in a time-space lattice

Controlling the flux piercing the plaquettes of the time-space crystalline lattice is important for realizing topological effects such as quantum Hall effect. The typical experimental scheme for creating artificial magnetic fluxes in 2D optical

lattices first of all involves creating a lattice potential gradient that suppresses particle hopping along one of the spatial directions. Secondly, the tunneling is restored by laser-induced Raman transitions that imprint a certain phase which contributes to the creation of the flux. Such a scheme was utilized in simulating Harper–Hofstadter type Hamiltonians which realize quantum Hall effect [35, 159]. In this section we will consider a similar scheme – the potential tilt will be introduced in the time domain by choosing a proper driving of the system and the phase will be controlled by the wavevector difference of the laser beams that restore the hoppings. Once again we will focus on the 2D TSCS since the ideas can be straightforwardly generalized to higher dimensions as it will be shown by exploring higher dimensional topological properties of a time-space crystalline structure.

2.5.1 Tilted potential in the time domain

First, let us concentrate on the potential tilt that suppresses the tunneling between the time domain sites. The easiest way to introduce this energy detuning between the s resonant states is to require that the previously discussed classical effective Hamiltonian $H_{\text{eff}}(\Theta, I)$ describing temporal structure in a single spatial site has an additional sawtooth potential term $v(\Theta)$:

$$\bar{H}_{\text{eff}}(\Theta, I) \equiv H_{\text{eff}}(\Theta, I) + v(\Theta), \quad (2.57)$$

where the sawtooth potential is defined by $v(\Theta) = U_x(\Theta - \beta)$ on the interval $\Theta \in [-\pi + \beta, \pi + \beta)$ and the values for the remaining Θ domain are obtained through the periodicity condition $v(\Theta + 2\pi m) = v(\Theta)$ with $m \in \mathbb{Z}$. Here U_x describes the tilt of the sawtooth function and β is a parameter that allows to control the shift of the function along Θ .

In the ideal case the schematic representation of the new potential would look like the one depicted in Fig. 2.9 with the original potential $-V_{\text{eff}} \cos(s\Theta)$ taken from subsection 2.1.3. The tilt U_x is chosen in such a way that the gaps between the minima of neighboring potentials Δ_1 and Δ_2 are much larger than the natural hopping parameter $|J|$ between the neighboring temporal sites.

Having the target effective Hamiltonian (2.57) in mind, we can engineer the initial time-dependent Hamiltonian that creates the sawtooth potential after time averaging. To this end, we include a general time-dependent signal $f(t)$ to the driving protocol which can be later tailored to produce the needed energy offsets between the time-domain sites. We start with a modified Hamiltonian (2.1) in the lab frame

$$H'_{\text{tilt}}(x, p_x, t) = \frac{p_x^2}{2m} + V_0 \sin^2(k_L [x - \lambda \cos(\omega t) - f(t)]) + V_1 \sin^2(2k_L [x - \lambda \cos(\omega t) - f(t)] + \varphi_x), \quad (2.58)$$

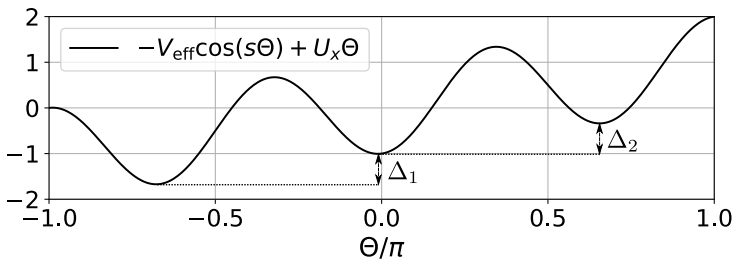


Figure 2.9: A schematic representation of a tilted potential in the temporal direction for a single spatial lattice site with $s = 3$ resonant states. The plot is shown in V_{eff} units, $\beta = 0$.

where an additional potential of strength V_1 and a new time-dependent driving signal $f(t)$ have been introduced. The new potential has a spatial period twice as short as the original potential and its position can be adjusted by tuning the relative phase φ_x . The purpose of this potential is to allow the creation of a slight asymmetry in the system which will be needed and justified when relating $f(t)$ to the final sawtooth potential. We assume that the signal $f(t)$ is periodic in time with the system's natural period $T = \frac{2\pi s}{\omega}$ and can in general be Fourier expanded as $f(t) = \frac{is}{\omega} \sum_{n \neq 0} \frac{f_n}{n} e^{in \frac{\omega}{s} t}$. Next, to obtain the correspondence between the driven Hamiltonian (2.58) and the tilted effective Hamiltonian (2.57), the secular approximation will be applied for the driven Hamiltonian expressed in action-angle coordinates around the resonant action.

Firstly, following the methods of subsection 2.1.1, the Hamiltonian can be transformed to the co-moving frame via a canonical transformation and written in dimensionless units as

$$H_{\text{tilt}}(x, p_x, t) = H_0(x) + p_x \left[\lambda \omega \sin(\omega t) + \sum_{n \neq 0} f_n e^{in \frac{\omega}{s} t} \right], \quad (2.59)$$

with H_0 denoting the static part

$$H_0(x) \equiv p_x^2 + V_0 \sin^2(x) + V_1 \sin^2(2x + \varphi_x). \quad (2.60)$$

Secondly, in the vein of subsection 2.1.3, the Hamiltonian is expressed in action-angle variables in the frame rotating at the natural frequency $\Omega = \frac{\omega}{s}$:

$$H_{\text{tilt}}(\Theta, I) = H_0(I) - \frac{\omega}{s} I + p_x \left(\Theta + \frac{\omega t}{s}, I \right) \left[\lambda \omega \sin(\omega t) + \sum_{n \neq 0} f_n e^{in \frac{\omega}{s} t} \right], \quad (2.61)$$

Finally, employing the secular approximation around the resonant action value

I_s one arrives at the effective Hamiltonian

$$\bar{H}_{\text{eff}}(\Theta, I) = H_{\text{eff}}(\Theta, I) + \sum_{n \neq 0} p_{-n}(I) f_n e^{-in\Theta}. \quad (2.62)$$

The part that does not depend on the new driving signal is denoted by

$$H_{\text{eff}}(\Theta, I) \equiv H_0(I_s) - \frac{\omega}{s} I_s + \frac{P^2}{2m_{\text{eff}}} - V_{\text{eff}} \sin[s\Theta + \arg(p_s(I))], \quad (2.63)$$

with effective momentum $P \equiv I - I_s$, effective mass $m_{\text{eff}} \equiv \left(\frac{\partial^2 H_0(I)}{\partial I^2} \Big|_{I_s} \right)^{-1}$ and effective potential $V_{\text{eff}} \equiv \lambda\omega|p_s(I)|$. The function $\arg(p_s(I))$ takes the argument of the Fourier component $p_s = |p_s|e^{i\arg(p_s(I))}$ which in general can be complex, depending on the shape of the static potential.

The obtained effective Hamiltonian (2.62) can now be directly compared to the target Hamiltonian (2.57). We see that in order to create the potential tilt the Fourier components of the driving signal $f(t)$ have to be chosen to satisfy the following equality

$$v(\Theta) = \sum_{n \neq 0} p_{-n}(I) f_n e^{-in\Theta}. \quad (2.64)$$

The components f_k can be expressed explicitly if the sawtooth potential is expanded as a Fourier series. Let the expansion be

$$v(\Theta) = \sum_{n \neq 0} v_n e^{-in\Theta}, \quad (2.65)$$

with the components

$$v_n = \frac{U_x}{2\pi} \int_{-\pi+\beta}^{\pi+\beta} (\Theta - \beta) [\cos(n\Theta) + i \sin(n\Theta)] d\Theta = iU_x \frac{(-1)^{n+1}}{n} e^{in\beta}, \quad (2.66)$$

for $n > 0$ and $v_n = v_{|n|}^*$ for $n < 0$. The index $n = 0$ is omitted in the sum since $v_0 = 0$. Plugging this expansion into the equality (2.64) gives the f_n components

$$f_n = iU_x \frac{(-1)^{n+1}}{np_{-n}(I)} e^{in\beta}. \quad (2.67)$$

At this point it becomes apparent why the potential proportional to V_1 is needed. If $V_1 = 0$, the even momentum components vanish ($p_{2n} = 0$, $n \in \mathbb{Z}$) due to the symmetry of the Hamiltonian thus the condition (2.67) cannot be satisfied. Setting $V_1 \neq 0$ and $\varphi_x \neq 0$ breaks the symmetry allowing for non-zero even momentum components to appear and the sawtooth potential can then be realized. In practice, we only consider around $|n| < 10$ components which

are enough to construct a sufficiently straight sawtooth potential, this is done to avoid f_n divergence for large n , when p_{-n} goes to zero.

Having derived the form of the components f_n , we only need to determine the proper set of parameters for the tilted potential. The main conditions that the potential has to satisfy are:

- The energy gaps Δ_i (for $i \in \{1, \dots, s-1\}$) between neighboring minima of the tilted lattice have to be much larger than the natural hoppings $|J|$ between the neighboring sites to restrict the tunneling, i.e. $|J| \ll \Delta_i$ for all i .
- The energy gaps Δ_i should be smaller than the energy needed to excite the resonant states to a higher energy band.
- The parameters should be chosen in such a way that all energy gaps Δ_i would have roughly the same energy Δ . This ensures that a single pair of counter-propagating laser beams is enough to restore the tunnelings with an imprinted phase.

Keeping these requirements in mind one can numerically scan the parameter space of U_x and β to find the optimal choice.

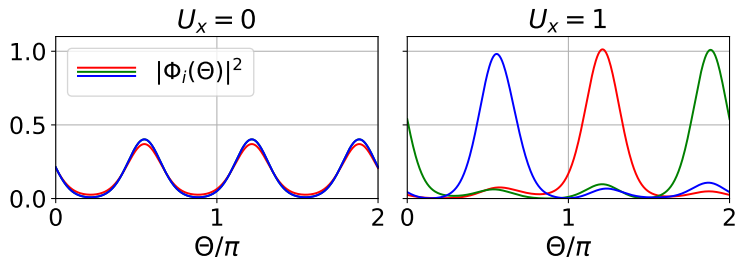


Figure 2.10: Left panel: Delocalized densities of the resonant states $|\Phi_i(\Theta)|^2$ on a single spatial lattice site when the tilt potential is turned off i.e. $U_x = 0$. Right panel: Localized densities when the tilt potential is turned on: $U_x = 1$, $\beta = 0.987$. The system parameters in both cases are $V_0 = 4320$, $\omega = 240$, $\lambda = 0.01$, $V_1 = 0.1V_0$ and $\varphi_x = \pi/8$.

The introduced tilt localizes the probability densities at each of the time domain sites thus suppressing the tunneling. This can be qualitatively checked by looking at the probability density of the resonant states $|\Phi_i(\Theta)|^2$ ($i = 1, \dots, s$) given by the quantized version of the classical effective Hamiltonian (2.62) with the same quantization procedure applied as in the beginning of subsection 2.4.2. Let us look at a concrete implementation of a system with and without the tilted potential for parameters $V_0 = 4320$, $\omega = 240$, $\lambda = 0.01$, $V_1 = 0.1V_0$ and $\varphi_x = \pi/8$ in both untilted and tilted cases. Note that $V_1 \ll V_0$ is chosen to maintain the main resonant state structure similar to what we had in the

previous section. For the tilted case we set the tilt coefficient to $U_x = 1$ and the phase to $\beta = 0.987$. Without the tilt we see that the resonant state densities are delocalized over the $s = 3$ sites in the time domain (Fig. 2.10 (left)), here two of the states have nearly degenerate energies hence their densities overlap. When the tilt is turned on each resonant state localizes at each of the time domain sites shown in Fig. 2.10 (right) indicating the suppression of hoppings.

So far we have applied the classical secular approximation and shown that it is possible to create a potential tilt in the time domain lattice by introducing an additional periodic driving with a particular choice of its Fourier components. In the next subsection, we will use the same ideas to extend the description to the quantum case.

2.5.2 Wannier functions of a tilted lattice

Our goal is to write down the Floquet Hamiltonian of the periodically driven system with the time-domain tilt inducing driving signal $f(t)$ and to find its resonant eigenfunctions. With the eigenfunctions at hand, we will acquire the localized Wannier functions of the resonant wavepackets which will be subsequently required to calculate the laser-restored tunneling parameters.

We start by canonically quantizing the lab frame Hamiltonian (2.58) which we considered in the previous subsection

$$\begin{aligned} \hat{H}'_{\text{tilt}}(x, p_x, t) &= \frac{\hat{p}_x^2}{2m} + V_0 \sin^2(k_L [\hat{x} - \lambda \cos(\omega t) - f(t)]) \\ &\quad + V_1 \sin^2(2k_L [\hat{x} - \lambda \cos(\omega t) - f(t)] + \varphi_x). \end{aligned} \quad (2.68)$$

Conceptually following section 2.2, we proceed by rotating the Hamiltonian to the oscillating frame via a unitary transformation $\hat{U}(t) = e^{\frac{i}{\hbar}[\lambda \cos(\omega t) + f(t)]\hat{p}_x}$ and writing it in dimensionless units

$$\hat{H}_{\text{tilt}}(t) = \hat{H}_0 + \left[\lambda \omega \sin(\omega t) + \sum_{n \neq 0} f_n e^{in \frac{\omega}{s} t} \right] \hat{p}_x, \quad (2.69)$$

where we have denoted the static part as $\hat{H}_0 \equiv \hat{p}_x^2 + V_0 \sin^2(\hat{x}) + V_1 \sin^2(2\hat{x} + \varphi_x)$. The Floquet Hamiltonian of such a system is $\hat{\mathcal{H}}_{\text{tilt}}(t) = \hat{H}_{\text{tilt}}(t) - i \frac{\partial}{\partial t}$ with solutions of its eigenvalue problem being Floquet-Bloch waves $\Phi_{k,\alpha}(x, t) = e^{ikx} u_{k,\alpha}(x, t)$ written in terms of periodic functions $u_{k,\alpha}(x, t) = u_{k,\alpha}(x + \pi, t) = u_{k,\alpha}(x, t + \frac{2\pi s}{\omega})$. For numerical calculations it is convenient to perform another unitary transformation $\hat{U}_k = e^{-i[\lambda \cos(\omega t) + f(t)]k}$ which allows us to represent the eigensolutions of the transformed Floquet Hamiltonian $\hat{\mathcal{H}}'_{\text{tilt}}(t) = \hat{U}_k \hat{\mathcal{H}}_{\text{tilt}}(t) \hat{U}_k^\dagger$ as a purely spatially periodic function denoted by

$u'_{k,\alpha}(x,t) = \hat{U}_k u_{k,\alpha}(x,t)$. The transformed Hamiltonian $\hat{\mathcal{H}}'_{\text{tilt}}(t)$ has the form

$$\hat{\mathcal{H}}'_{\text{tilt}}(t) = \hat{H}_0(k) + \left[\lambda\omega \sin(\omega t) + \sum_{n \neq 0} f_n e^{in\frac{\omega}{s}t} \right] \hat{p}_x - i\frac{\partial}{\partial t}, \quad (2.70)$$

with the static part

$$\hat{H}_0(k) \equiv (\hat{p}_x + k)^2 + V_0 \sin^2(\hat{x}) + V_1 \sin^2(2\hat{x} + \varphi_x) \quad (2.71)$$

now dependent on the wavevector k . If we solve the eigenvalue problem $\hat{\mathcal{H}}'_{\text{tilt}}(t)u'_{k,\alpha}(x,t) = E_{k,\alpha}u'_{k,\alpha}(x,t)$ we can relate its solutions $u'_{k,\alpha}(x,t)$ to the wavefunctions $\Phi_{k,\alpha}(x,t)$ of the original Floquet Hamiltonian $\hat{\mathcal{H}}_{\text{tilt}}(t)$:

$$\Phi_{k,\alpha}(x,t) = e^{ik[x+\lambda \cos(\omega t)+f(t)]} u'_{k,\alpha}(x,t). \quad (2.72)$$

Since our interest lies in the s resonant states of the system, the quantum secular approximation will be employed to obtain the states $u'_{k,\alpha}(x,t)$, $\alpha = 1, \dots, s$, from Hamiltonian $\hat{\mathcal{H}}'_{\text{tilt}}(t)$. The approximation was explicitly introduced in subsection 2.2.3 and verified in subsection 2.4.2, therefore here we straightforwardly calculate the resulting time averaged Hamiltonian matrix elements $\tilde{\mathcal{H}}'_{n',n}(k)$:

$$\tilde{\mathcal{H}}'_{n',n}(k) = \frac{1}{sT} \int_0^{sT} dt \langle \psi_{k,n'} | e^{in'\frac{\omega}{s}t} \hat{\mathcal{H}}'_{\text{tilt}}(t) e^{-in\frac{\omega}{s}t} | \psi_{k,n} \rangle, \quad (2.73)$$

where the time is averaged over s natural periods T of the system. The elements are written in the stationary Hamiltonian $\hat{H}_0(k)$ basis $\psi_{k,n}(x)$ with the time-dependent unitary transformation $e^{in\frac{\omega}{s}t}$ applied to move into a frame that rotates with the resonant frequency $\frac{\omega}{s}$. Here n is the quantum number labeling the states of the stationary Hamiltonian. After time averaging we get the final form of the quantum secular Hamiltonian matrix elements

$$\begin{aligned} \tilde{\mathcal{H}}'_{n',n}(k) &= \left(E_{k,n}^{(0)} - n\frac{\omega}{s} \right) \delta_{n',n} \\ &+ \left(\frac{i\lambda\omega}{2} [\delta_{n',n+s} - \delta_{n',n-s}] + f_{n-n' \neq 0} \right) \langle \psi_{k,n'} | \hat{p}_x | \psi_{k,n} \rangle, \end{aligned} \quad (2.74)$$

with $E_{k,n}^{(0)}$ being the n -th eigenenergy of the stationary Hamiltonian and $f_{n-n' \neq 0}$ is the $n - n'$ Fourier component of the new driving signal, provided that $n - n' \neq 0$. If $n = n'$, the term $f_{n-n' \neq 0}$ vanishes.

The resonant eigenfunctions $\tilde{u}'_{k,\alpha}$ and eigenenergies $\tilde{E}'_{k,\alpha}$ of the quantum secular Hamiltonian $\tilde{\mathcal{H}}'(k)$ approximate the solutions of the Hamiltonian $\hat{\mathcal{H}}'_{\text{tilt}}(t)$ for $\alpha \in \{1, \dots, s\}$. In turn, by diagonalizing (2.74) we already obtain the solutions

of the Floquet Hamiltonian:

$$\Phi_{k,\alpha}(x,t) \approx e^{ik[x+\lambda \cos(\omega t)+f(t)]} \bar{u}'_{k,\alpha}(x,t). \quad (2.75)$$

These solutions allows us to calculate the localized Wannier functions $w_{j,\alpha}(x,t)$ at spatial site j (determined by the eigenvalue of position operator) and time domain site α by diagonalizing the position operator:

$$(\hat{x})_{k',k}^{(\alpha)} = \int_{-\frac{\pi}{2}L}^{\frac{\pi}{2}L} \Phi_{k',\alpha}^*(x,t) \hat{x} \Phi_{k,\alpha}(x,t) dx. \quad (2.76)$$

Note that now the position operator matrix is block-diagonal since the different resonances $\alpha \in \{1, \dots, s\}$ do not couple due to the tilt in the time domain.

We have constructed the Floquet Hamiltonian for a system with a time-domain tilt and applied the secular approximation to obtain its eigenfunctions. This allowed us to construct the localized wavepackets which will be used to determine the hopping parameters restored with the Raman laser beams.

2.5.3 Laser-assisted tunneling

After applying the new driving protocol $f(t)$ we now effectively have a 2D TSCS with natural hoppings along the spatial direction and no hoppings between time-domain sites. The driving introduced energy shifts Δ between neighboring time-domain sites which suppress the tunneling. We will use a well-known approach that employs a two-photon transition [32] to restore these hoppings with a controllable phase.

Let us start with two Raman laser beams with frequencies ω_1 and ω_2 traveling in directions defined by their wavevectors \vec{k}_1 and \vec{k}_2 . Assume that the superposition of these beams creates a traveling wave described by the dimensionless coupling potential $V_c(\vec{x}, t) = \Omega_{\text{ph}} \cos(\Delta \vec{k}_{\text{ph}} \vec{x} - (\omega_1 - \omega_2)t)$ which couples two energy levels that differ by energy $|\omega_1 - \omega_2|$, with Rabi frequency Ω_{ph} describing the coupling strength. The potential in general depends on the position vector \vec{x} and the difference of the beam wavevectors $\Delta \vec{k}_{\text{ph}} = \vec{k}_2 - \vec{k}_1$. Choosing the frequencies of the lasers to be such that $\omega_1 - \omega_2 \approx \Delta$ is satisfied allows us to couple the neighboring time-domain sites precisely. This can be seen in the interaction picture where the coupling potential cancels out the energy offsets Δ between the sites and introduces a position-dependent complex phase in the tunneling elements. Explicitly, the restored hopping parameters between time-domain sites α and $\alpha + 1$ on a single spatial site j have the form

$$J_{j,\alpha}^{j,\alpha+1} = \int_0^{sT} \frac{dt}{sT} \int_{-\frac{\pi}{2}L}^{\frac{\pi}{2}L} dx w_{j,\alpha+1}^*(x,t) \Omega_{\text{ph}} e^{i\Delta k_{\text{ph}} x} w_{j,\alpha}(x,t), \quad (2.77)$$

where $w_{j,\alpha}(x,t)$ are the Wannier functions of the tilted lattice. We have as-

sumed that the spatial lattice is aligned with the x direction thus we only take the projection of the product $(\Delta\vec{k}_{\text{ph}}\vec{x})_x \equiv \Delta k_{\text{ph}}x$ onto x . Changing the wavevector difference Δk_{ph} provides us with a way to control the complex phase of $J_{j,\alpha}^{j,\alpha+1}$ and in turn the artificial magnetic fluxes e.g. the fluxes that appeared in Fig. 2.7. There is also a possibility to tune tunneling amplitudes by introducing a time-dependent coupling strength $\Omega_{\text{ph}}(t)$ which can be engineered to enhance or diminish the tunneling when the wavepackets overlap in space.

One noteworthy consequence of the potential tilt in the time-domain is that the periodicity of the time-domain lattice is broken, unlike the case we had with a simply driven system in Fig. 2.7. The restored hopping parameter $J_{j,s}^{j,1}$ between the s -th and the first resonant wave-packet is zero since laser-assisted tunneling does not provide sufficient energy to compensate for multiple energy offsets Δ required for the levels to couple. This is true for all spatial sites j , therefore we end up with a system that has open boundaries in the time direction. The appearance of hard edges can be used to probe edge localization and edge currents as will be seen in the next subsection.

To summarize, we have completed the mathematical toolbox required to engineer controllable complex hopping parameters in a TSCS by using the ideas of laser-assisted tunneling. This allows us to tune the fluxes that appear in our system by adjusting the wavevector difference of the Raman laser beams and probe topological effects in a TSCS.

2.5.4 Topological properties of time-space crystalline structures

The ability to create and control magnetic-like fluxes opens up the possibility to explore the quantum Hall effect in time-space crystalline structures. In this subsection, we will express the Chern number characterizing the topology of the TSCS and numerically show the emergence of topologically protected edge states for a finite time-space lattice, following the ideas presented in section 1.2.

The hallmark signature of the integer quantum Hall effect is the quantization of Hall conductance in a 2D system pierced by magnetic fluxes perpendicular to the surface. A direct way to evaluate if the quantization is present is to calculate the so-called first Chern number ν_1 . It is an integer topological invariant proportional to Hall conductance – its non-zero value implies the presence of topologically protected edge currents and in turn the integer quantum Hall effect. The first Chern number is obtained from the bulk properties of the system, therefore to calculate it we first extend the size of our system so that the number of spatial and time-domain sites approaches infinity. Then we Fourier expand the creation and annihilation operators of the infinite 2D time-space crystalline lattice tight-binding Hamiltonian (2.41) with modified flux-adjusting hoppings in terms of spatial quasi-momentum k and temporal

quasi-momentum \mathcal{K} . Assuming that the solutions for the n -th energy band of the Hamiltonian have the form of Bloch waves $e^{i(kj+\mathcal{K}\alpha)}|n_{k,\mathcal{K}}\rangle$ with j and α indexing spatial and time-like sites respectively, the first Chern number can be explicitly expressed as

$$\nu_1^{(x)} = \frac{1}{2\pi} \int_{\text{BZ}} dk d\mathcal{K} \mathcal{F}^{xt}. \quad (2.78)$$

Here we integrate the Berry curvature $\mathcal{F}^{xt} \equiv \frac{\partial}{\partial k} \mathcal{A}_{\mathcal{K}} - \frac{\partial}{\partial \mathcal{K}} \mathcal{A}_k$ over the first Brillouin zone (BZ) with the Berry connection components $\mathcal{A}_{\mathcal{K}} = i\langle n_{k,\mathcal{K}} | \frac{\partial}{\partial \mathcal{K}} | n_{k,\mathcal{K}} \rangle$ and $\mathcal{A}_k = i\langle n_{k,\mathcal{K}} | \frac{\partial}{\partial k} | n_{k,\mathcal{K}} \rangle$ completely determined by the eigenvectors $|n_{k,\mathcal{K}}\rangle$ of the system. The superscript (x) indicates that the considered Chern number is associated with the 1D spatial lattice aligned along the x direction.

Similarly, the quantization of Hall conductance can be evaluated in a higher-dimensional lattice. Let us start with a 6D time-space crystalline structure described in section 2.3. Introducing additional driving signals for each spatial direction according to subsection 2.5.1 creates adjustable energy offsets between time-domain sites for each orthogonal direction separately. The hoppings suppressed by the added potential tilt are then restored with a controllable phase by employing laser-assisted tunneling of subsection 2.5.3. This requires three pairs of Raman laser beams that are tuned to compensate for the energy offsets between time-like sites in each spatial direction. After applying all the preceding steps we obtain a 6D lattice where spatial lattices in each orthogonal direction are accompanied by their time-domain sites and come equipped with controllable fluxes. These fluxes pierce each of the 2D surfaces formed by a lattice in one of the directions and its corresponding time-domain sites. Since our Hamiltonian is separable its solution in quasi-momentum space is a product of three 2D Bloch waves $e^{i(\vec{k}\vec{j}+\vec{\mathcal{K}}\vec{\alpha})}|n_{k_x,\mathcal{K}_x}\rangle|n_{k_y,\mathcal{K}_y}\rangle|n_{k_z,\mathcal{K}_z}\rangle$, where the vectorized quantities are associated with each spatial direction, i.e. $\vec{v} = (v_x, v_y, v_z)$ for any \vec{v} . For a 6D system the third-order response due to the appearing fluxes is characterized by the third Chern number ν_3 which in our case is just a product of the three first Chern numbers in each of the directions $\nu_3 = \nu_1^{(x)}\nu_1^{(y)}\nu_1^{(z)}$ due to the separability of the eigenstate of the n -th band [45]. The present calculations of Chern number provide a numerical way to detect the integer quantum Hall in the multidimensional time-space crystalline structures.

A non-trivial topology can also be identified by the presence of topologically protected edge states. Let us take a 6D time-space crystalline structure that is periodic in the spatial directions but has a finite number of sites s in the time-like directions. The open boundaries in the time-domain appear naturally when we introduce the tilted lattice and the phase-inducing laser-assisted hoppings as discussed in the last subsection. The complex hoppings are engineered to produce a square lattice with a ribbon geometry for each pair of spatial and temporal directions with a flux $\frac{\pi}{2}$ piercing each square plaquette.

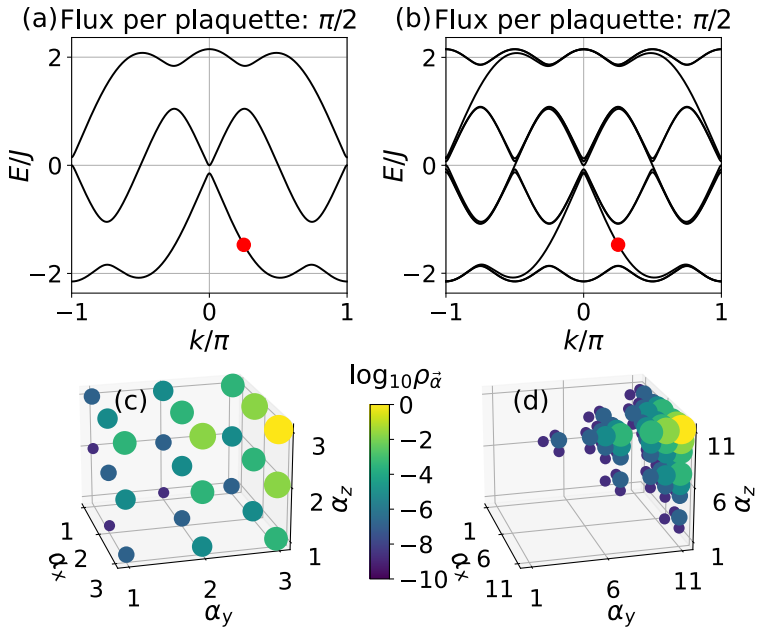


Figure 2.11: Top panels: Energy dispersion relation of one of the three 2D time-space ribbons that compose the 6D time-space lattice. The square plaquettes of the ribbons are pierced by a flux of $\frac{\pi}{2}$. Number of sites in the time-like direction considered: (a) $s = 3$ and (b) $s = 11$. Red circles indicate the selected edge states for the projected density results shown below. Bottom panels: Edge state probability density projected onto the time-domain sites for (c) $s = 3$ and (d) $s = 11$ time-domain sites. Parameters for the $s = 3$ case are $V_0 = 4320$, $\omega = 240$, $\lambda = 0.01$, $V_1 = 0.1V_0$, $\varphi_x = \pi/8$ and $U_x = 1$, ten components of the driving signal $f(t)$ were used. For $s = 11$, the tight-binding model was artificially extended in the time-domain by using the hopping parameters obtained from $s = 3$ case.

Fig. 2.11 depicts the energy dispersion of one of these 2D ribbons that consist of $s = 3$ (a) and $s = 11$ (b) time-domain sites. The topological edge states are the states whose energies cross the gap between the energy bands in the dispersion relation. These states correspond to the chiral edge modes at the open boundaries of the ribbon related to the non-zero Chern number. Topological edge states are clearly present in the energy dispersion Fig. 2.11(b) of the broad ribbon and the onset of their formation can be already seen for the narrow ribbon in Fig. 2.11(a) as well. To further exemplify the localization of the edge state $|\psi\rangle$ at the edge of the 6D time-space lattice we define the on-site probability density as $\rho_{\vec{j},\vec{\alpha}} = \langle \psi | \hat{a}_{\vec{j},\vec{\alpha}}^\dagger \hat{a}_{\vec{j},\vec{\alpha}} | \psi \rangle$ and calculate the density projected on the time-like dimension $\rho_{\vec{\alpha}} = \sum_{\vec{j}} \rho_{\vec{j},\vec{\alpha}}$. As a working point we select an edge state at quasi-momentum $k_x = k_y = k_z = \frac{\pi}{4}$ denoted by red circles on the dispersion plots of Fig. 2.11(a,b). The logarithm of the projected density onto

time-domain sites of the chosen states is shown in Fig. 2.11(c) for $s = 3$ and Fig. 2.11(d) for $s = 11$. Here the magnitude of the projected density is encoded by both color and size of the circles. The size changes linearly with color. We see that in both projected density plots the density is localized at a single coordinate point ($\alpha_x = \alpha_y = \alpha_z = 3$ in Fig. 2.11(c) and $\alpha_x = \alpha_y = \alpha_z = 11$ in Fig. 2.11(d)). This means that when the densities are summed over the spatial sites for each temporal site branch, the 1D branch at the edge of the lattice has the largest total density for all of the time-like directions α_i which is the expected result for the edge state. Thus we have shown that the non-trivial topology of a time-space lattice can be indicated by the presence of gap crossing energies in dispersion relations and confirmed that the states corresponding to those energies are indeed localized at the edge.

We have shown that topological properties can be probed in higher dimensional time-space crystalline structures with artificial gauge fields present and provided the expression to evaluate the topological invariant characterizing these systems. We asserted the presence of topological edge states by calculating the dispersion of finite systems along the temporal direction and checked that their probability densities are localized at the open boundaries of the system.

2.6 Summary

Starting with the classical analysis of a periodically and resonantly driven lattice we have shown that additional periodic structure emerges at the potential wells in a reference frame rotating with the natural resonance frequency. This structure can be exploited as a synthetic dimension which we refer to as time-like or temporal. The quantum description of such a system allowed us to construct an effectively 2D lattice from a 1D resonantly driven spatial potential. The 2D system consists of a spatial and a temporal dimension and is termed a time-space crystalline structure. We have analyzed a concrete realization of a quasi-1D time-space lattice: explored its parameter selection regime, asserted the validity of the theoretical description, determined the geometry of the lattice and proposed an experimental scheme. Since each orthogonal spatial direction of a driven lattice comes equipped with the time-like dimension, we extended the description to include 4D and 6D time-space crystalline structures for 2D and 3D spatial lattices respectively. Having a general description of time-space lattices we employed a laser-assisted tunneling scheme to introduce controllable complex tunnelings in the lattice. The complex tunnelings provided a way to create artificial gauge fields within the lattice and allowed us to probe the topological properties of the system. This completed the theoretical toolbox of a time-space crystalline structure which will hopefully prove to be a versatile system to explore higher-dimensional electronics.

Chapter 3

LEARNING THE GROUND STATE STRUCTURE WITH ARTIFICIAL NEURAL NETWORKS

Many-body phenomena observed in ultracold atom gases trapped in optical lattices pose a significant computational challenge due to the vast number of interacting particles present in such systems. While the current numerical tools are capable of obtaining the ground-state of lattices that consist of tens to hundreds of sites with varying success depending on the particular problem [52], novel methods are developed that target the relevant low-energy subspace potentially allowing to increase accuracy or address larger systems [160]. Machine learning has proven its worth in high-dimensional data analysis in language processing, classification problems and image recognition [161, 162]. Recently it has found increasing success in condensed matter physics as well – it was applied to classify phases of matter [163, 164], extrapolate phase transitions [165], classify experimental data [166, 167] and perform quantum tomography [168]. Of particular interest for quantum computations is a general ansatz that allows representing a lowest-energy state as an artificial neural network [57, 60]. Neural network quantum states can encode ground states that are highly entangled [64, 169] and have been used to analyze strongly correlated quantum matter [170–176], providing comparable or even higher accuracy results than well-established methods.

Our goal is to apply the neural network state formalism to flat-band lattice systems and analyze the accuracy of the obtained results, as well as explore the possibility to improve the ground state given a set of noisy superpositions of states. In this chapter, we will introduce two types of artificial neural networks – a restricted Boltzmann machine and a feedforward autoencoder. Following [A2] in sections 3.1 and 3.2, the restricted Boltzmann machine will be applied to obtain lattice ground states and probe their structure while being guided by energy minimization. In particular, two lattice geometries that support com-

pact localized eigenstates will be analyzed – a quasi-one-dimensional sawtooth lattice and a 2D kagome lattice. The application of the autoencoder takes a different approach. In section 3.3, it will be used as a secondary analysis tool that takes the approximate ground state solutions obtained by other numerical methods and attempts to produce an improved ground state estimate, based on [A3]. Its capabilities will be explored by recovering the ground state densities of a square and sawtooth lattice from a noisy initial sample set.

3.1 Artificial neural network for ground state determination

We start by defining the artificial neural network model used for ground-state structure determination. Firstly we discuss the restricted Boltzmann machine architecture that encodes the wavefunction. Secondly, the reinforced learning procedure is described. It utilizes the variational Monte Carlo method to minimize the energy of the lattice Hamiltonian and hence encodes the lowest energy wavefunction in the network weights. After setting up the general machinery of the network we will apply it to concrete physical systems.

3.1.1 Restricted Boltzmann machine

The choice of the architecture of the artificial neural network is highly dependent on the task at hand. The most prominent networks for solving quantum problems aimed at obtaining the ground state are restricted Boltzmann machines [57–59] and feedforward neural networks [60]. Some work is being done with convolutional neural networks as well [61, 171]. Motivated by the success of ground state energy estimations of the restricted Boltzmann machines we select this network architecture to probe the structure of ground states. In the following, we show how the wavefunction is encoded in the chosen representation.

The information about the quantum system is stored in its state $|\psi\rangle$. For lattice Hamiltonians it is convenient to express the state $|\psi\rangle$ in occupation number basis $|\gamma\rangle \equiv |n_0, n_1, \dots, n_L\rangle$ where n_ℓ is the particle number on site $\ell \in \{0, 1, \dots, L\}$ with $L + 1$ being the total number of lattice sites. We have denoted a particular particle configuration in the lattice by γ . Then a general state can be expressed as

$$|\psi\rangle = \sum_{\gamma} |\gamma\rangle \langle \gamma | \psi \rangle = \sum_{\gamma} \psi(\gamma) |\gamma\rangle, \quad (3.1)$$

where $\psi(\gamma)$ are complex probability amplitudes.

The restricted Boltzmann machine is a generative neural network based

on variational energy minimization. Its main ansatz is that the probability amplitudes $\psi(\gamma)$ can be modeled as marginalized Boltzmann distributions

$$\psi(\gamma) = \psi(n_0, n_1, \dots, n_L) = \sum_{\{h_j\}} e^{\sum_{\ell=0}^L a_\ell n_\ell + \sum_{\ell=0}^L \sum_{j=1}^M W_{\ell j} n_\ell h_j + \sum_{j=1}^M b_j h_j}, \quad (3.2)$$

where h_j is the hidden node parameter, n_ℓ is the visible node parameter which in our case corresponds to the occupation number of site ℓ , $W_{\ell j}$ is the coupling of the ℓ -th visible node to the j -th hidden node, finally a_j and b_j are respectively visible and hidden node biases. We denote the collection of the weights that define the network as a set $\vec{w} = \{W_{\ell j}, a_\ell, b_j\}$ for all ℓ and j . The sums are performed over all hidden node values $\{h_j\}$, the $L+1$ visible nodes and M hidden nodes. Schematically the model is depicted in Fig. 3.1 as a fully connected two layer artificial neural network. This Boltzmann machine is called restricted

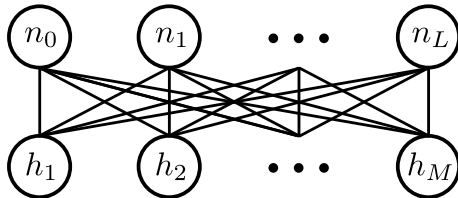


Figure 3.1: Restricted Boltzmann machine as a two layer neural network. All $L+1$ visible nodes n_ℓ are connected with all M hidden nodes h_j by straight lines which correspond to the couplings $W_{\ell j}$.

because there are no intra-layer connections, i.e. the visible/hidden nodes are not connected between each other. It simplifies the learning procedure of the network [160]. Setting the hidden node parameters to be $h_j \in \{-1, 1\}$ the hidden node values are straightforwardly traced out in the expression of the probability amplitude giving

$$\psi(\gamma) = e^{\sum_{\ell=0}^L a_\ell n_\ell} \prod_{j=1}^M 2 \cosh \left(\sum_{\ell=0}^L W_{\ell j} n_\ell + b_j \right). \quad (3.3)$$

This representation encodes the wavefunction in $\mathcal{N} = LM + 2M + L + 1$ complex parameters that are elements of the weights \vec{w} . L is determined by the size of the considered lattice and M is the number of hidden nodes that can be adjusted to control the representational power. It can be compared to the exact number of complex coefficients required to describe the state. Assuming that the lattice of size $L+1$ is occupied by a fixed number of particles $N_p = \sum_{\ell=0}^L n_\ell$ then the configuration space consists of

$$\mathcal{C} = \frac{(N_p + L)!}{N_p! L!} \quad (3.4)$$

elements that define the state. For the calculations to be efficient we expect that only a small subspace of the Hilbert space is sufficient to describe the system, i.e. a network with $\mathcal{N} \ll \mathcal{C}$ weights captures the physics of the ground state. This is satisfied for the lattices analyzed in this work. The efficiency and limitations of restricted Boltzmann machines for a larger class of states are explored in detail in Ref. [177].

We have introduced the artificial neural network structure that encodes the probability amplitudes of a wavefunction in its weights. The next section provides the methods required to update the weights to obtain the ground state.

3.1.2 Reinforced learning

A reinforced learning scheme can be outlined as the adjustment of weights of a neural network guided by the minimization of a cost function. The cost function in our case is the energy. The minimization procedure consists of two steps. First, we use the variational Monte Carlo method which samples the configuration space and provides average energy estimates. Then the network weights get updated using a gradient-based optimization algorithm.

Let \hat{H} be a Hamiltonian describing a lattice. The goal is to minimize the energy

$$E = \frac{\langle \psi | \hat{H} | \psi \rangle}{\langle \psi | \psi \rangle} \quad (3.5)$$

by varying the neural network weights \vec{w} that define $|\psi\rangle$. Since we will use a gradient-based minimization algorithm, we start by evaluating the energy derivatives with respect to each weight $w \in \vec{w}$:

$$\frac{\partial E}{\partial w} = \langle E_{\text{loc}} \mathcal{O}_w \rangle - \langle E_{\text{loc}} \rangle \langle \mathcal{O}_w \rangle + \text{c.c.}, \quad (3.6)$$

where $E_{\text{loc}} \equiv \frac{\langle \gamma | \hat{H} | \psi \rangle}{\langle \gamma | \psi \rangle}$ is the so-called local energy, $\mathcal{O}_w \equiv \frac{\partial \ln \psi(\gamma)}{\partial w}$ and c.c. denotes the complex conjugated part. The key idea here is that instead of calculating the expectation values in the derivative (3.6) which involve a sum over all of the configurations $|\gamma\rangle$ of the system, the expectation values are replaced by statistical averages of a finite set of samples of the configuration space. The sampling is based on a Monte-Carlo procedure where each newly generated configuration $|\gamma'\rangle$ is connected to the previous state $|\gamma\rangle$ by a transition permitted by the single-particle lattice Hamiltonian. The new state $|\gamma'\rangle$ is accepted with the probability $\min \left\{ 1, \frac{|\langle \gamma' | \psi \rangle|^2}{|\langle \gamma | \psi \rangle|^2} \right\}$ to ensure detailed balance. After performing N_{MC} Monte Carlo moves, we calculate the averages of E_{loc} , \mathcal{O}_w and their product over the generated Markov chain of sampled states. This allows us to evaluate the energy gradient (3.6) and update the weights. Note that the stochasticity of the estimated averages due to Monte Carlo sampling

in this case is useful since it helps escaping local energy minima. The variance of these fluctuations is inversely proportional to the number of samples taken, thus it can be decreased by performing more N_{MC} steps as needed.

At this point, we can choose a preferred gradient-based optimization algorithm to perform minimization. The simplest method is the gradient descent where the updated weights are calculated as

$$w_{t+1} = w_t - \eta \frac{\partial E}{\partial w_t}. \quad (3.7)$$

Here η is the learning rate and the index $t \in \mathbb{N}$ denotes the t -th iteration of weight updates. Gradient descent has a problem that it easily gets stuck to a local energy minima while scanning the weight space due to the learning rate being constant. One solution to this problem is to use stochastic gradient descent which replaces the exact derivative over the parameters by an estimator that takes the derivative obtained from only a few random samples [178, 179]. This allows it to escape the local energy minima but the convergence to the target energy is slow due to the high variance of each weight update. Alternatively, one of the optimizers that can be used is an adaptive moment estimation method (Adam) which computes adaptive learning rates for all of the parameters from estimates of first and second moments of the gradients [180]. The first and second moment of the gradient updates can be written respectively as

$$\mu_t = \beta_1 \mu_{t-1} + (1 - \beta_1) \frac{\partial E}{\partial w_t}, \quad (3.8)$$

$$\sigma_t = \beta_2 \sigma_{t-1} + (1 - \beta_2) \left(\frac{\partial E}{\partial w_t} \right)^2, \quad (3.9)$$

where $\beta_1 = 0.9$ and $\beta_2 = 0.999$ are meta-parameters of the method with the typical suggested values. The initial moments are set to zero ($\mu_0 = 0, \sigma_0 = 0$). Then the weights are updated using the Adam method's expression:

$$w_{t+1} = w_t - \frac{\eta}{\sqrt{\frac{\sigma_t}{1-\beta_2^t} + \epsilon}} \cdot \frac{\mu_t}{1 - \beta_1^t}, \quad (3.10)$$

here a regularization parameter $\epsilon = 10^{-8}$ is introduced to prevent the gradient term from diverging if $\sigma_t = 0$. For the lattice ground state estimation we use a variation of Adam algorithm called AdaMax. It implements one main change in Adam – instead of damping the learning rate by the 2-norm of the energy gradient i.e. $\sqrt{\sigma_t}$, it uses the ∞ -norm of a p -power gradient update $v_t = \beta_2^p v_{t-1} + (1 - \beta_2^p) |\partial E / \partial w_t|^p$ with $v_0 = 0$, which also provides stable numerical results. Writing ∞ -norm u_t explicitly

$$u_t = \lim_{p \rightarrow \infty} (v_t)^{\frac{1}{p}} = \max \left(\beta_2 u_{t-1}, \left| \frac{\partial E}{\partial w_t} \right| \right), \quad (3.11)$$

gives a numerically simple update law. The weight optimization by AdaMax is then defined as

$$w_{t+1} = w_t - \frac{\eta}{u_t} \cdot \frac{\mu_t}{1 - \beta_1^t}, \quad (3.12)$$

with learning rate $\eta = 0.002$ and $u_0 = 0$.

Having discussed the components of reinforced learning we provide the protocol of our calculations:

1. Initiate the neural network with random small weights \vec{w} and choose a random initial configuration of the system $|\gamma\rangle$.
2. Perform N_{MC} Monte Carlo moves sampling the configuration space to evaluate the energy of the network with the current weights.
3. Update weights using Adam/AdaMax methods.
4. Repeat from 2. for a fixed amount of updates N_{update} or until the desired convergence of the observed parameters is reached.

After the network has been optimized to represent the ground state we can use it to estimate the expectation value of an arbitrary operator \hat{A} . It is obtained by performing Monte Carlo sampling one last time and calculating the statistical average of $\frac{\langle \gamma | \hat{A} | \psi \rangle}{\langle \gamma | \psi \rangle}$ over the generated samples.

We have covered the basic ideas of ground state representation as a restricted Boltzmann machine and looked at the reinforced learning procedure which employs variational Monte Carlo and gradient-based optimization to obtain the state with minimal energy. We are now ready to tackle the problem of calculating ground-state features of a lattice system within the described artificial neural network framework.

3.2 Learning ground state features of flat band lattices

Lattices that support flat dispersionless energy bands give rise to a lot of interesting phenomena such as fractional quantum Hall effect [100,181,182], correlations in superconductivity [183,184], flat band magnetism in spin systems [185] and other, see review Ref. [71]. We will consider a particular class of ground states that can be expressed as compact localized eigenstates [186,187] which are associated with the lowest energy flat band of a lattice. These states are superpositions of Bloch waves localized at several neighboring sites while being separated from each other by at least one empty site due to destructive quantum interference of the wavefunctions. They provide sufficiently complex density patterns for the neural network to learn while being guided by the energy of a non-trivial many-body Hamiltonian. In this section, we will analyze

the performance of the artificial neural network for two flat band lattices that have a quasi-1D sawtooth and 2D kagome geometries.

3.2.1 Sawtooth lattice

One of the simplest flat band systems is the sawtooth lattice. There have been proposals [188, 189] and experimental realizations of such models in photonic lattices [190] and ultracold atom systems [191]. We will introduce a particular parameter regime of this lattice that establishes the ground state features used for neural network testing.

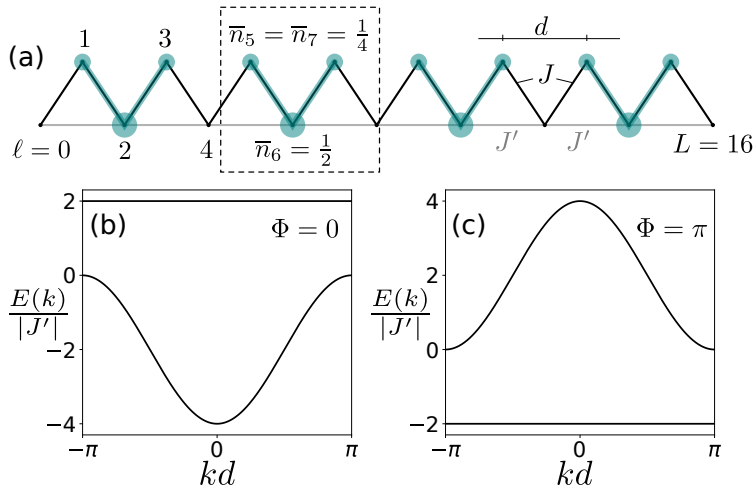


Figure 3.2: (a) Sawtooth lattice of $L + 1 = 17$ sites with lattice constant d . Hoppings J and J' are depicted by black and grey lines respectively. Dashed box marks the second density island with a single particle localized over three sites with corresponding teal-colored on-site occupations $\bar{n}_5 = \bar{n}_7 = \frac{1}{4}$ and $\bar{n}_6 = \frac{1}{2}$. (b) Energy dispersion relation for $J' > 0$ with no flux $\Phi = 0$ piercing the triangular plaquettes. (c) Dispersion relation for $J' < 0$ with flux $\Phi = \pi$ piercing the plaquettes.

The single-particle physics of a sawtooth lattice of $L + 1$ sites (Fig. 3.2(a)) is described by the tight-binding Hamiltonian

$$\hat{H}_0 = -J \sum_{\ell=1}^L \hat{a}_{\ell}^{\dagger} \hat{a}_{\ell-1} - J' \sum_{j=1}^{L/2} \hat{a}_{2j}^{\dagger} \hat{a}_{2j-2} + \text{h.c.}, \quad (3.13)$$

with annihilation (creation) operators $\hat{a}_{\ell}^{(\dagger)}$ at site ℓ and the hermitian conjugate part of both terms denoted by h.c.. Hopping parameter J is the tunneling amplitude between neighboring lattice sites (solid black diagonal and off-diagonal links in Fig. 3.2(a)) and J' is the tunneling between next-neighbor sites labeled by even numbers in Fig. 3.2(a) (grey links).

The band structure of this model can be straightforwardly calculated by assuming the periodic boundary condition for the lattice and diagonalizing the Hamiltonian in quasi-momentum k representation [192]. The obtained energy dispersion relation reads

$$E(k) = -J' \cos(kd) \pm \sqrt{J'^2 \cos^2(kd) + 2J^2 \cos(kd) + 2J^2}, \quad (3.14)$$

with d being the lattice constant. The flat band regime is achieved by setting $J = \sqrt{2}|J'|$ in Eq. (3.14). This gives the two solutions for the energy bands

$$E(k) = \begin{cases} 2J' \\ -2J' [\cos(kd) + 1] \end{cases}. \quad (3.15)$$

From this relation we see that there are two distinct cases: $J' > 0$ where the dispersionless band has the highest energy (Fig. 3.2(b)) and $J' < 0$ with a flat band having the lowest energy $\frac{E(k)}{|J'|} = -2$ (Fig. 3.2(c)). We will only consider $J' < 0$ case onward since it not only has the flat band at the bottom of the energy spectrum but it also has π -flux Φ piercing each triangle plaquette. I.e. the wavefunction of a particle that hops around the closed triangular plaquette accumulates a π Peierls phase each loop due to the presence of a negative hopping parameter. This adds a level of complexity for the neural network to learn. For $J' > 0$ all of the hopping parameters are positive thus we have the trivial case $\Phi = 0$.

The richness of flat band models usually reveals itself with the inclusion of interactions. We will consider bosonic on-site interactions

$$\hat{H}_{\text{int}} = \frac{U}{2} \sum_{\ell=0}^L \hat{n}_{\ell}(\hat{n}_{\ell} - 1), \quad (3.16)$$

where $\hat{n}_{\ell} = \hat{a}_{\ell}^{\dagger} \hat{a}_{\ell}$ is the occupation number operator for site ℓ and U is the interaction strength. The interaction term is positive therefore it costs energy to place two or more particles at the same site.

The features of the groundstate of the complete system $\hat{H}_0 + \hat{H}_{\text{int}}$ highly depend on the filling of the lattice defined as $\frac{N_p}{L}$. For filling less than or equal to $\frac{1}{4}$ the particles try and succeed to avoid each other. This can be seen from the densities of the so-called compact localized states. They are linear combinations of Bloch states with various quasi-momenta that localize the particle density in the presence of a flat band. The average occupation of these states for quarter-filling of the lattice is depicted by the teal color in Fig. 3.2(a). A single particle occupies one V shaped island that consists of three sites with corresponding on-site densities $\frac{1}{4}$, $\frac{1}{2}$ and $\frac{1}{4}$ that are separated from the rest of the lattice by empty sites at the edges. An example of such a density island is marked by a dashed box in Fig. 3.2(a). Since the system at $\frac{1}{4}$ filling is partitioned into

these islands it is easy to calculate the total energy of a system of an arbitrary length $L + 1$ if we know the energy of a single island. A state of an island can be written as

$$|\psi_j\rangle = \frac{1}{2} \left(\sqrt{2}\hat{a}_j^\dagger - \hat{a}_{j-1}^\dagger - \hat{a}_{j+1}^\dagger \right) |\text{vac}\rangle, \quad (3.17)$$

with j labeling an even site and $|\text{vac}\rangle$ being the vacuum state of an empty lattice. Calculating the energy of such a state $\langle\psi_j| \left(\hat{H}_0 + \hat{H}_{\text{int}} \right) |\psi_j\rangle$ we see that it is equal to $-2|J'|$ keeping in mind that $J' < 0$. It is important to stress that it does not depend on the interaction strength, i.e. $\langle\psi_j|\hat{H}_{\text{int}}|\psi_j\rangle = 0$. Thus for a finite lattice of $L + 1$ sites the full energy of the ground state is $E_{\text{gs}} = -\frac{|J'|L}{2}$. For filling larger than $\frac{1}{4}$ the calculations are more difficult and in most cases calculated numerically.

For the purpose of studying the neural network, we will focus on the flat band regime with $J = \sqrt{2}|J'|$ and $J' < 0$. We set the lattice filling to be $\frac{1}{4}$ and take several values of interaction strength U . This regime provides sufficiently rich features for the neural network to learn and at the same time the exact results can be easily calculated analytically for comparison. The goal of the neural network is to obtain the ground state density wave depicted in Fig. 3.2(a) as accurately as possible.

3.2.2 Learning the density wave

The characteristic properties of the ground state are calculated using the implementation of a restricted Boltzmann machine by the Netket collaboration [193]. The considered physical system is a $L+1 = 17$ site sawtooth lattice with $N_p = 4$ particles corresponding to the quarter-filling regime. The hopping parameters are chosen to establish a dispersionless band as described in the previous subsection and the interactions are set to $\frac{U}{|J'|} = 0.1$. For the artificial neural network we select the number of hidden nodes to be $M = \lfloor \alpha(L+1) \rfloor$ with $\alpha = 2.5$ being the hidden node density and $\lfloor \cdot \rfloor$ denoting the floor function. We perform $N_{\text{update}} = 15000$ weight \vec{w} updates using AdaMax optimization routine with its default meta-parameters defined in subsection 3.1.2. Before each update of weights, $N_{\text{MC}} = 5000$ Monte Carlo moves are made to explore the configuration space. The choice of the lattice and hidden layer sizes is motivated by the fact that the selected number of sites provides a configuration space that is larger than the number of network weights. This means that if the ground state is learned by the network we effectively encoded the state into a reduced representation.

The main parameters that are monitored during the learning process of the network are the ground state energy E_{gs} , the overlap f between exact and network predicted ground states, the on-site occupation of three sites that have different densities: the empty site at the edge of an island with expected density $\bar{n}_4 = 0$, the site at the edge of the V-shaped island $\bar{n}_5 = \frac{1}{4}$ and the site

at the center of the island $\bar{n}_6 = \frac{1}{2}$. The total density of the second island Σ is observed as well and it is expected to be equal to $\bar{\Sigma} \equiv \bar{n}_5 + \bar{n}_6 + \bar{n}_7 = 1$. The decimal logarithm of the absolute error ε for each of these values is shown in Fig. 3.3 after every weight update. We will focus on the densities of a single density island for concreteness but the results are general for each island. Let us look at the behavior of each observable more carefully.

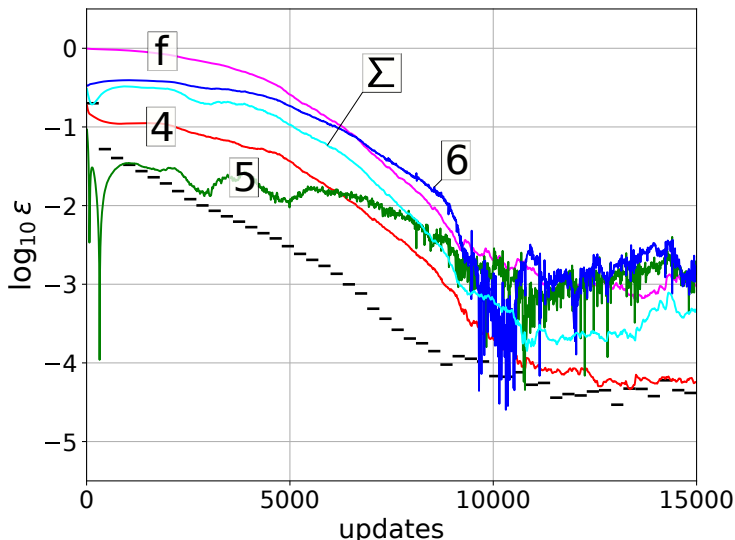


Figure 3.3: Absolute error ε convergence of properties describing the ground state of a sawtooth lattice: ground state energy E_{gs} error (black dashes), average occupation error on sites 4 (red), 5 (green) and 6 (blue), deviation from the total density Σ on the second V shaped island (cyan) and the deviation from unity of overlap f between exact and calculated ground states (magenta).

The convergence of absolute error of the ground state energy E_{gs} is depicted by black dashes. Each dash is 300 updates long and its value is the average of energy errors binned during those iterations. The error decreases exponentially for the first 10000 updates and then levels out when the deviation from the exact energy value $\frac{E_{\text{gs}}}{|\mathcal{J}|} = -8$ is between 10^{-5} and 10^{-4} . This is comparable to the energy errors obtained with neural networks for other quantum models [57, 60, 63]. The high convergence rate and accuracy of ground state energy is not surprising since reinforced learning of the network is guided by energy minimization.

The global and local density structure recognition can be judged by the convergence of on-site densities. Empty sites separating each density island define the global structure of the density wave. It is accurately captured by the neural network as can be seen from the on-site occupation of the empty site labeled ‘4’. During the initial updates, the error decrease of the zero density site

lags behind the energy error which is expected because density is not the target quantity being optimized by the network. Despite the slower convergence, the final density of the empty site is determined with accuracy comparable to that of the ground state energy, i.e. the deviation from true value is within the range 10^{-5} and 10^{-4} . The local structure is defined by the densities within each V-shaped island. We concentrate on the second island depicted by the dashed box in Fig. 3.2(a). The occupation error evolution of sites with expected densities $\bar{n}_5 = \frac{1}{4}$ and $\bar{n}_6 = \frac{1}{2}$ is labeled by ‘5’ and ‘6’ respectively in Fig. 3.3. Firstly, we note that the sharp downward peaks of errors is not a physical effect but an artifact of absolute error changing sign. Secondly, we see that the end result is not as accurate compared to the previously considered observables. Initially, the error of density on site ‘5’ seems to be lower than the rest of the density errors. This is because the on-site density $\frac{1}{4}$ is very close to the average density $\frac{4}{17}$ of the lattice therefore a typical random distribution can estimate it straight away, nevertheless, the initial small error does not improve or accelerate the convergence to the exact value. The final deviation from exact density values for both sites is of the order 10^{-3} which is more than a magnitude larger than the energy or empty site density errors. The relatively high fluctuations of these errors at the final updates show that the network struggles to distribute the density between the three sites of the island. Thus the network efficiently and accurately determines the global structure of the density wave but the local features are obtained with lower accuracy.

Finally, we look at the overlap f of the calculated state with the exact ground state and the sum of densities Σ of the second island sites. These quantities support the previously obtained results. The overlap essentially accounts for densities over all sites thus its convergence rate mimics the plotted densities and arrives at the error of 10^{-3} which is mostly due to the local density fluctuations within the islands. The sum of densities follows a similar pattern of convergence for the initial 10000 updates but then it achieves an error smaller than that of density errors of sites ‘5’ and ‘6’. This indicates that the network fairly accurately predicts the presence of a single particle per one island and larger on-site density errors show that indeed the difficulties arise due to local density fluctuation balancing on an individual island.

The results shown in Fig. 3.3 correspond to a single statistical sample of observables obtained from a restricted Boltzmann machine throughout the learning process. Starting the learning procedure with different initial weights produces qualitatively similar behavior of error values. To check if the global and local features are reproduced for larger systems we look at the occupation of all sites for quarter-filled lattices of sizes $L \in \{20, 60, 100\}$. The evolution of densities in Fig. 3.4 for $L = 20$ (a), $L = 60$ (b) and $L = 100$ (c) share the key feature that the formation of the global density wave structure appears on average after the same number of updates independently on the system size.

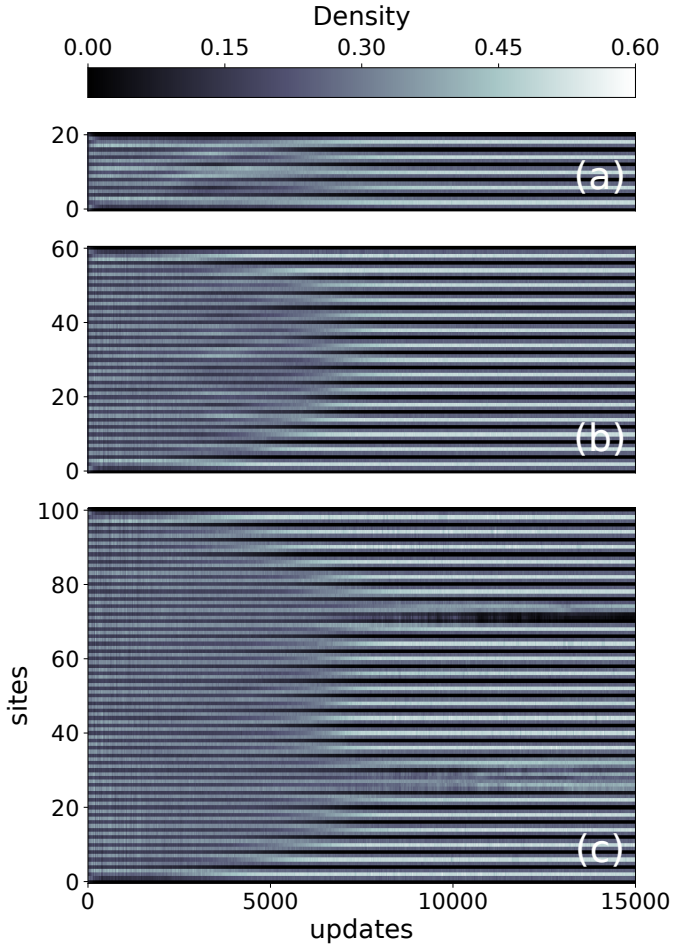


Figure 3.4: On-site density evolution for lattices of size $L = 20$ (a), $L = 60$ (b) and $L = 100$ (c) with parameters $\alpha = 2.5$, $N_{\text{MC}} = 5000$ and $\frac{U}{|J|} = 0.1$.

However, in the depicted case, only the smaller lattices (a) and (b) manage to converge to the exact ground state. For the largest lattice (c) local defects are created which are hard for the network to eliminate. The origin of these defects can be explained as independent island formation in separate parts of the lattice – the independent islands seed the global structure in their regions which permeates until the regions meet. If the initial islands did not have matching periodicity, the regions clash and form the observed defect. In principle, this defect can appear in a system of any size but it is more likely to form in larger systems. The network has difficulties escaping this configuration because a global structure change of one of the regions is required to restore proper periodicity of the full density wave. It is equivalent to a problem of escaping a local energy minimum which is a typical obstacle that optimization

algorithms face [194]. One needs to either improve the optimization protocol or sample multiple networks initiated with different weights to obtain the exact ground state.

To summarize, the restricted Boltzmann machine accurately determines the global structure of the ground state of a sawtooth lattice by identifying the partition of the lattice into density islands with high precision. However, the local structure within each island is obtained with an accuracy lower by an order of magnitude. The convergence rate of densities does not depend on the lattice size although for larger lattices local defects can appear preventing the density wave formation.

3.2.3 Impact of hidden layer size

In the previous section, we have explored a typical learning process of a neural network for a fixed set of lattice and network parameters. In this section, we will check how the change of hidden node density affects the learning rate of the main observables.

The hidden node density α allows controlling the number of weights that encode the wavefunction. By choosing $\alpha = 2.5$ with $L+1 = 17$ sites and $N_p = 4$ particles considered previously, the number of coefficients needed to describe the ground state was reduced to $\frac{\mathcal{N}}{\mathcal{C}} \approx 16\%$ (recall that \mathcal{N} is the number of network weights and \mathcal{C} is the number of complex coefficients describing the full state). In the following, the size and filling of the system remain as before but the network hidden node density is set to be $\alpha \in \{1, 2, 2.5, 4\}$ corresponding to a reduction of the total coefficients to 7%, 13%, 16% and 26% respectively.

We will concentrate on two quantities that allow us to evaluate the accuracy of the neural network – absolute error of ground state energy E and the deviation from the total occupation Σ of the second island. First let us look at the evolution of ground state energy error for different hidden layer sizes in Fig. 3.5. The increase of hidden node density provides a twofold improvement – the convergence to the expected value is faster and the deviation from the exact value is smaller. A prominent improvement is observed in the detection of total second island occupation as well (Fig. 3.6). The estimated density value improves by two orders of magnitude going from $\alpha = 1$ to $\alpha = 4$. The number of updates required to reach higher accuracy is decreased by incrementing α as well. Note that even though the precision increases for both parameters with large α , the single island density still does not reach the accuracy of the ground state energy which means the problem of learning local structure remains. The results shown in the figures are obtained from a single learning procedure of a restricted Boltzmann machine for each α . To strengthen the observations we collect the statistics of how long it takes for the observables to reach the error of 10^{-3} from their exact values. Ten independent networks are initiated for each

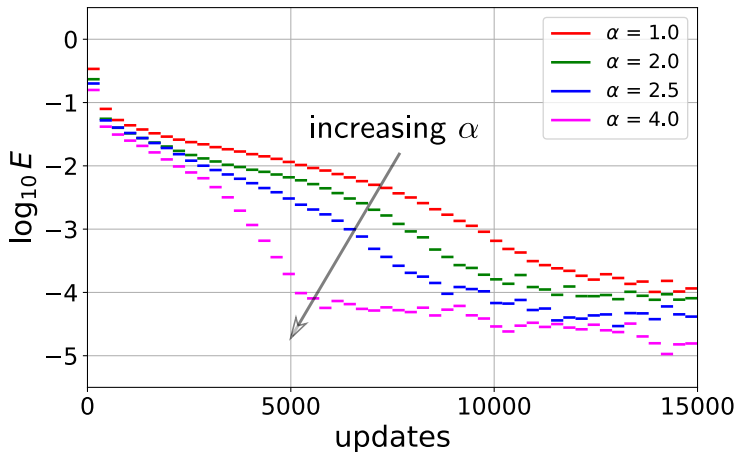


Figure 3.5: Convergence of the absolute error (in decimal logarithm) of ground state energy for hidden node density $\alpha \in \{1, 2, 2.5, 4\}$. Parameters used for the simulation: $L + 1 = 17$, $\frac{U}{|J|} = 0.1$ and $N_{\text{MC}} = 5000$.

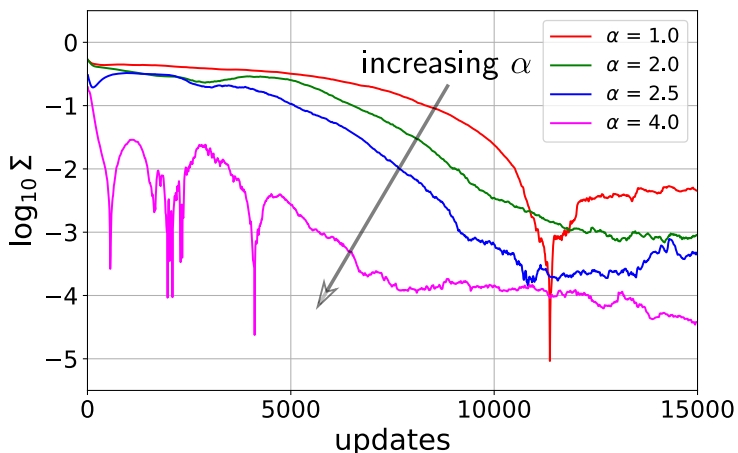


Figure 3.6: Deviation from unity of the total density on the second island throughout the learning process for hidden node density $\alpha \in \{1, 2, 2.5, 4\}$.

α , the average number of updates it takes to arrive at the aforementioned error for energy and total second island density is plotted in Fig. 3.7 by black and red points respectively. There is a clear downward trend for both observables in the number of required iterations to achieve the same error with the increase of hidden layer size. The update number starts to level off for large α . This confirms that increasing the hidden node density improves convergence. The downside of having a large hidden node density is that although the accuracy is improved the computational time of each weight update increases depending

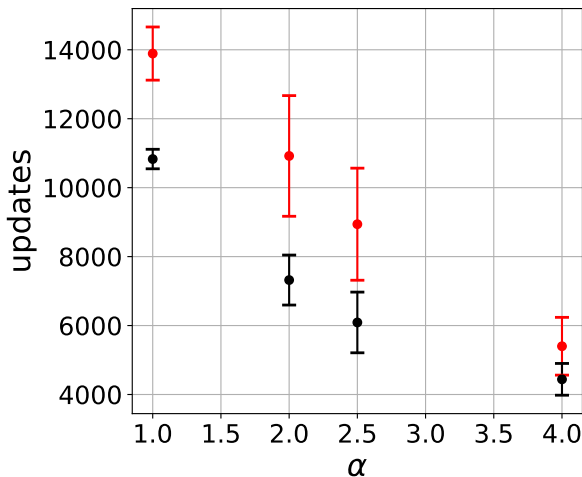


Figure 3.7: The average number of updates required to reach the ground state energy (black) and total second island occupation (red) error of 10^{-3} given the hidden node density $\alpha \in \{1, 2, 2.5, 4\}$. The errorbars show the standard deviation calculated from ten independent learning procedures for each α .

on the chosen optimizer. Therefore it is often the case that accuracy has to be sacrificed for the network to learn in a reasonable amount of time.

Overall increasing the size of the hidden layer proves to be beneficial to obtain more accurate results in a smaller amount of updates. The limiting factor of this improvement is the computational time required by the optimizer to efficiently adjust the enlarged weight space. This leads to only marginal precision gain for large hidden node density.

3.2.4 Role of interaction strength

The ground state of a flat band sawtooth lattice with quarter-filling is a special case – it does not depend on the interaction strength since it is composed of separated single-particle islands. For the neural network to reach this density wave state, it inevitably explores the excited state manifold which does depend on interactions thus the learning rate and accuracy can be affected by the presence of interparticle effects. We will look at how different interaction strength changes the convergence of the ground state energy and the total occupation of one of the density islands.

Once again we consider a quarter-filled sawtooth lattice of $L + 1 = 17$ sites and a network with hidden node density $\alpha = 2.5$. The interaction values taken for the learning process are $\frac{U}{|J|} \in \{0.02, 0.1, 0.5, \infty\}$. Here $\frac{U}{|J|} = \infty$ is the hardcore boson regime that prohibits two or more bosons from occupying the same site which effectively corresponds to infinite repulsive interactions. We look

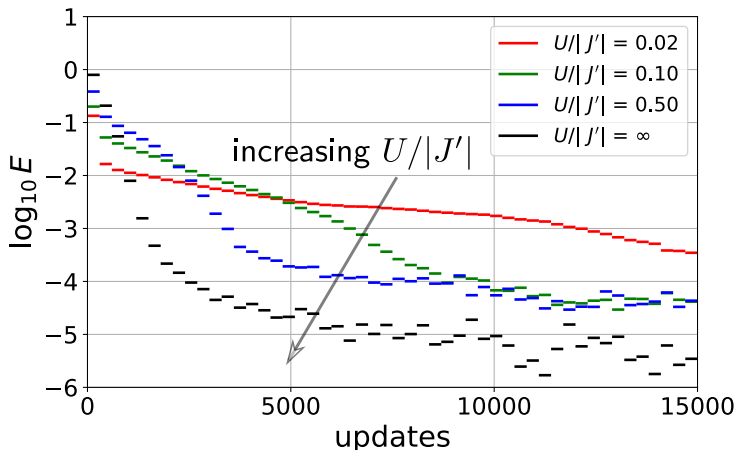


Figure 3.8: Ground state energy error convergence for different interaction strengths $\frac{U}{|J'|} \in \{0.02, 0.1, 0.5, \infty\}$.

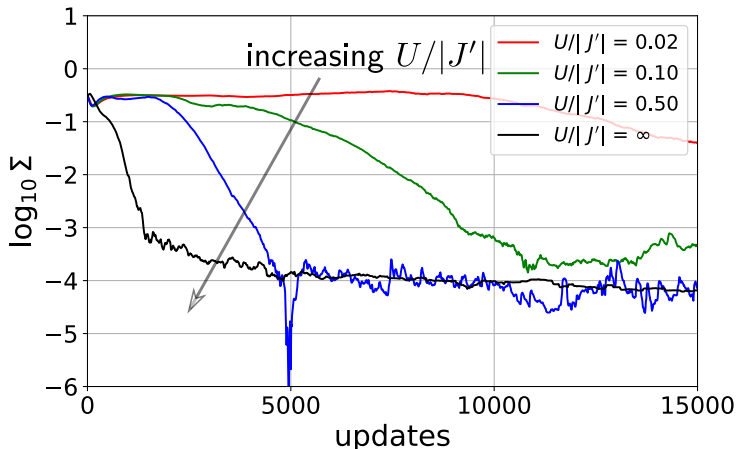


Figure 3.9: Evolution of the total occupation of the second density island error throughout the learning process for interactions $\frac{U}{|J'|} \in \{0.02, 0.1, 0.5, \infty\}$.

at the evolution of the decimal logarithm of the ground state energy error in Fig. 3.8 and the total density error on the second island in Fig. 3.9 for different interaction strengths. Both cases show significantly faster learning rates when interaction strength is increased. This is a similar result as observed in Ref. [60]. A possible explanation is that stronger interactions lead to a larger energy gap $E_{\text{gap}} \equiv E_1 - E_{\text{gs}}$ between the ground state energy E_{gs} and the first excited state energy E_1 thus making the lowest energy more discernible for the optimizer exploring the energy manifold. Exact diagonalization of the full Hamiltonian shows that in our case the gap is indeed getting wider for the selected interaction

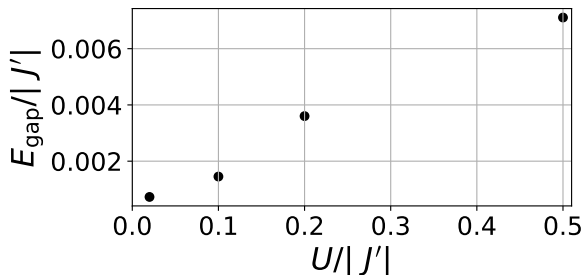


Figure 3.10: Energy gap between the ground and the first excited state energies of the sawtooth lattice for a set of interaction strengths.

strength values as seen in Fig. 3.10. The accuracy of the final values also improves however up to a certain point. For the energy error in Fig. 3.8 the converged accuracy improves significantly when the interaction is increased from $\frac{U}{|J'|} = 0.02$ to $\frac{U}{|J'|} = 0.1$ but does not effectively change when tuning from $\frac{U}{|J'|} = 0.1$ to $\frac{U}{|J'|} = 0.5$. The hard-core boson limit $\frac{U}{|J'|} = \infty$ provides the most accurate prediction of energy but it is a special case since it reduces the Fock space that is sampled – the states with two or more particles on a single site are ignored. This means that the high accuracy can be attributed to the improved representability of the wavefunction since the number of coefficients required to describe the full state is reduced but the amount of weights remains the same. It is equivalent to increasing the hidden node density as discussed in the previous subsection. The final precision of the island density in Fig. 3.9 shows improvement with increasing interaction strength until it reaches $\frac{U}{|J'|} = 0.5$ which fluctuates around the same value as the hard-core boson case.

Thus even though the observed values converge to the final value in a lesser number of updates for larger interaction strength, the final precision is not necessarily improved – the neural network reaches a limit over which there is no improvement.

This concludes the overview of the neural network convergence results obtained for the sawtooth lattice. By observing the on-site particle densities and the ground state evolution during the learning procedure and analyzing the precision of the final results we have determined that the global structure of the ground state density wave is learned with high precision while the local structure is detected with lower accuracy. Increasing the hidden layer size improves both the learning rate and the final result whereas increasing interaction strength significantly improves the learning rate but fails to improve accuracy for sufficiently high enough interaction strength values. In the following subsections, we will apply these observations to see if the neural network manages to successfully learn the properties of a higher dimensional flat-band system as well.

3.2.5 Kagome lattice

The kagome lattice forms a trihexagonal pattern shown in Fig. 3.11(a). It is an example of a 2D lattice that supports a flat band [192, 195]. The main challenge that this system poses for the artificial neural network to overcome is the extended dimensionality compared to the sawtooth lattice.

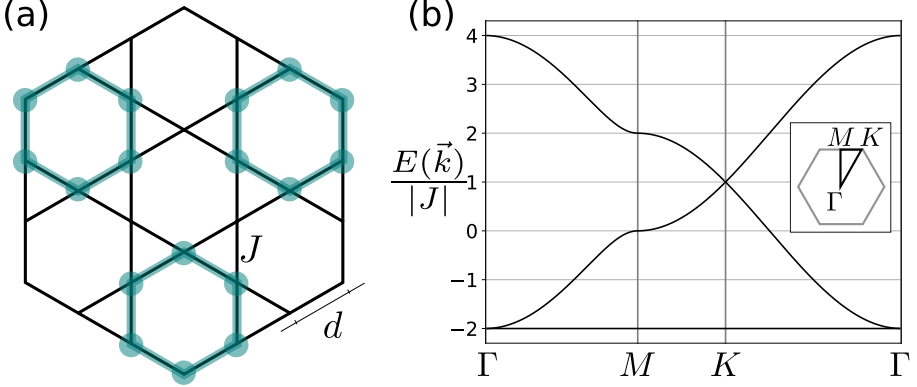


Figure 3.11: (a) Kagome lattice segment with lattice constant d . Hopping J is indicated by black links connecting all neighboring sites. Each teal-colored ring-like islands represent the density of a single localized particle, the remaining sites are empty. (b) Energy dispersion along the high symmetry lines of the Brillouin zone for $J < 0$. The inset contains the contour of the Brillouin zone (grey) with the high-symmetry points Γ , M , K and the path taken across the quasi-momentum space to plot the dispersion (black).

The Hamiltonian of the kagome lattice is

$$\hat{H} = -J \sum_{\langle ij \rangle} \hat{a}_i^\dagger \hat{a}_j + \frac{U}{2} \sum_i \hat{n}_i (\hat{n}_i - 1), \quad (3.18)$$

with J being the hopping parameter between neighboring sites, U – on-site interaction strength, $\hat{a}_i^{(\dagger)}$ – particle annihilation (creation) operator at site i , $\hat{n}_i = \hat{a}_i^\dagger \hat{a}_i$ – particle number operator and $\langle ij \rangle$ denotes summation over directed links connecting nearest neighbor sites. The energy bands calculated from the single-particle kinetic term are

$$E_1(\vec{k}) = 2J, \quad \text{and} \quad E_{2,3}(\vec{k}) = J \left(-1 \pm \sqrt{8\Lambda(\vec{k}) + 1} \right), \quad (3.19)$$

where we have denoted

$$\Lambda(\vec{k}) \equiv \cos \left(\frac{\sqrt{3}}{2} k_x d + \frac{1}{2} k_y d \right) \cos \left(-\frac{\sqrt{3}}{2} k_x d + \frac{1}{2} k_y d \right) \cos(k_y d). \quad (3.20)$$

Here $\vec{k} = (k_x, k_y)$ is the quasi-momentum vector and d – the lattice constant.

The system hosts a dispersionless band $E_1(\vec{k})$ and two dispersive energy bands $E_2(\vec{k})$ and $E_3(\vec{k})$ that differ by the sign in front of the square root term. If the hopping parameter is set to $J < 0$, then the flat band corresponds to the ground state energy and π fluxes appear piercing the triangular plaquettes of the lattice, like in the sawtooth geometry. The energy dispersion relation for this choice is plotted in Fig. 3.11(b) along the lines connecting the high symmetry points of the Brillouin zone shown in the inset. This parameter setting with the inclusion of non-zero repulsive interactions supports compact localized states for filling less than $\frac{1}{9}$. From now on we will only consider this filling regime since it establishes a localized island formation phenomena with a global structure similar to the one used to probe neural network capabilities in the sawtooth case. For the kagome lattice, the density islands form isolated hexagonal ring shapes (Fig. 3.11(a)) separated by sites having zero on-site occupation. Explicitly the localized state is [192]:

$$|\psi\rangle = \frac{1}{\sqrt{6}} \sum_{\ell_{\circ}=1}^6 (-1)^{\ell_{\circ}} \hat{a}_{\ell_{\circ}}^{\dagger} |\text{vac}\rangle, \quad (3.21)$$

where ℓ_{\circ} indicates the summation over the sites of a single hexagonal ring. The ground state is the union of these non-overlapping single-particle states, therefore the ground state energy E_{gs} of the system with filling less than $\frac{1}{9}$ is the energy of a compact localized state $\langle\psi|\hat{H}|\psi\rangle = -2|J|$ multiplied by the number of particles N_p in the lattice. Finally the average occupation of each site of the island is $\bar{n} = \frac{1}{6}$ which follows from the construction (3.21).

The analytical results obtained in this section will provide the exact values of observables to compare with the estimates calculated by the neural network.

3.2.6 Learning hexagonal density islands

After fairly successful attempts at recognizing the structure of the quasi-1D sawtooth lattice, in this section, we explore how the neural network fairs in determining the density islands of the 2D kagome lattice.

Let us start with finite kagome lattice segments that consist of either 30 sites with 3 particles or 41 sites with 4 particles present in the system. The geometry of these segments is shown in insets of Fig. 3.12(a) and Fig. 3.12(b) respectively. The hopping parameter is chosen to be $J < 0$ and the interaction strength is set to $\frac{U}{|J|} = \infty$. The hard-core boson regime is selected because even though the ground state does not depend on the interactions, a significant increase in network convergence rate and precision is obtained as seen from the results of the sawtooth case. This set of parameters and fillings satisfy the island formation conditions described in the previous subsection. For the neural network learning procedure, the hidden node density is $\alpha = 2.5$ and the number of Monte Carlo moves is $N_{\text{MC}} = 5000$.

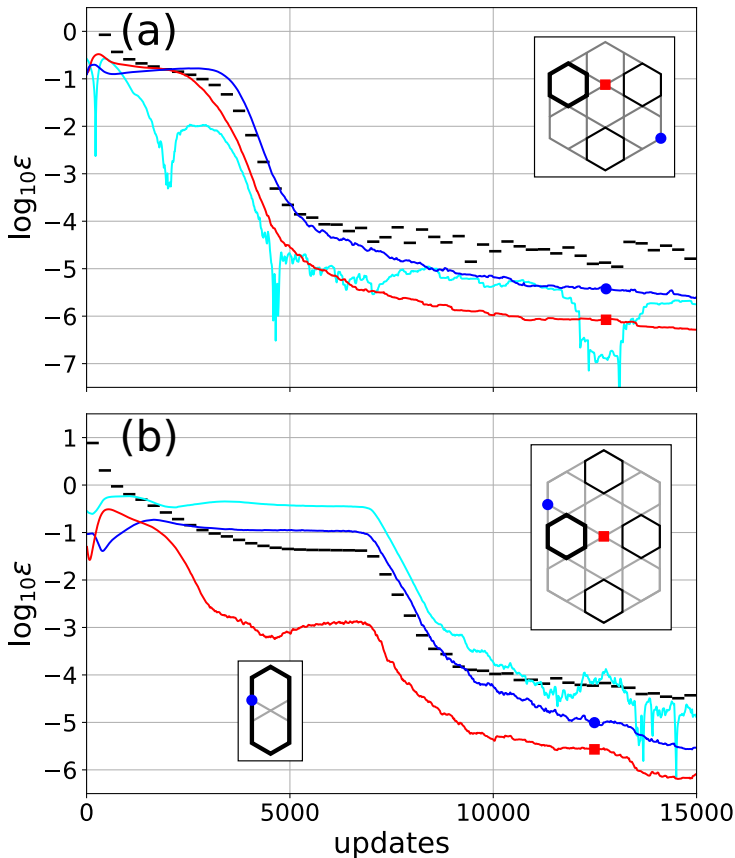


Figure 3.12: Convergence of (a) 30 site, 3 particle and (b) 41 site, 4 particle kagome lattice observables: evolution of logarithmic error of ground state energy (black bars), total occupation of a hexagonal island (cyan curve) and on-site density of selected sites (red and blue curves). The insets in the upper right corners show localized density islands indicated by the black hexagons, the hexagon with a thick black outline corresponds to the island selected for total occupation n_{\circ} monitoring, the red square and blue circle indicate the position of empty sites selected for density measurements. The small inset in (b) depicts a transient density structure forming during the plateau of the learning process.

Having established the system defining parameters we look at the evolution of absolute errors of observables in Fig. 3.12. The monitored observables are the ground state energy (black bars), the total occupation of a single density island (cyan curve) and on-site densities of two selected empty sites with their positions indicated by colored symbols in the inset (red square and blue circle). The expected values of ground state energy are $\frac{\bar{E}_{\text{gs}}}{|J|} = -6$ for the 3 particle and $\frac{\bar{E}_{\text{gs}}}{|J|} = -8$ for the 4 particle system. A single hexagonal density island is

occupied by one particle hence the expected density of such an island is $\bar{n}_O = 1$. For the smaller lattice that hosts three localized islands (Fig. 3.12(a)), we see that the neural network has no problems determining the energy with precision comparable to the sawtooth case. The empty site densities converge to zero fast and with high precision which indicates that global structure is recognized. The occupation of a single island precision after 15000 updates is of the order $10^{-6} \div 10^{-5}$ which affirms the localization of a particle. Similar results for final errors can be seen for the larger lattice with four compact localized states in Fig. 3.12(b). One distinct feature during the learning procedure for the larger segment is the plateau where the errors stay constant for a certain amount of updates. This happens because the network gets stuck into a local energy minimum when a local structure depicted by a thick black line in the lower inset of Fig. 3.12(b) forms. Due to the destructive interference of the wavefunction at the center of this transient structure, it takes a while for the optimizer to escape the minimum by locally rearranging the density to form one single-particle island.

The restricted Boltzmann machine successfully encodes the ground state of the kagome lattice. The global structure is determined with high accuracy but for larger lattices, local energy minima can hinder the learning rate of the network.

3.2.7 Summary

Employing an artificial neural network equipped with the restricted Boltzmann machine architecture we have analyzed the success of encoding the ground state of flat band systems in the network weights. Guided by energy minimization the network detected global features of the ground state with high accuracy for quasi-1D sawtooth and 2D kagome lattices. The empty sites separating compact localized single-particle states were detected with precision comparable to that of energy. The fidelity of local density distribution within a localized density island was typically a magnitude lower in the sawtooth case. Adjusting the size of the network we have seen that an increase of hidden layer nodes leads to improved learning rates and final results due to the increased representability. Faster learning rates were also observed with higher interaction strength values which can be explained by larger energy gaps between the ground and excited states improving the discernability of the lowest state. Finally, the performance of the network was tested with lattice scaling. For large lattices there was no decrease in precision however the optimizer tends to get stuck in local energy minima more frequently. This results in local density defects that hamper the learning rate or prevent the system from converging. To resolve this issue the learning procedure has to be restarted or the optimizer has to be improved.

3.3 Autoencoder-based ground state fidelity improvement

A general quantum state is described by a vector in a Hilbert space. For a system of N spins with m spin degrees of freedom, the number of coefficients needed to express such a state in a local basis is m^N . The number of coefficients increases exponentially with the size of the system and quickly becomes computationally intractable even for a moderate number of particles $N \sim 10^4$ typically considered in ultracold atom experiments. Hilbert space is a big place [196, 197]. Luckily, the interest usually lies in the lowest energy states. This allows numerical methods to target the small subspace of the Hilbert space that these states occupy. Various strategies are employed to reach the said manifold – a reduction of the complexity of the many-body quantum problem by projector operator based approaches [198], ground state solution calculation using imaginary time evolution [199, 200], variational methods based on an efficient representation of the wavefunction as a tensor network [54, 55] or an artificial neural network [57, 60, 63]. In the end, the output of these methods is an approximate ground state function.

In this section, we aim to employ a type of artificial neural network called an autoencoder [201] to perform a secondary analysis of the results obtained by approximate methods mentioned above. Assuming that the numerical methods generate a set of possible ground states with errors arising either due to the inherent truncation of the problem or randomness due to sampling and optimization, we use these states as a training input for the autoencoder. The autoencoder reduces the dimensionality of the provided results and encodes them in a low-dimensional subspace. By analyzing the structure of this encoding followed by autoencoder-preformed decoding, we explore the separability of low-lying energy states and potentially extract an improved estimate of the ground state.

3.3.1 Approximate states via feedforward neural network

The approximate methods used for ground-state calculation of a quantum problem provide a solution which is a random superposition of the lowest-lying energy states. The key assumption that we make is that the contribution of the ground state in this superposition is dominant. Based on this supposition we choose a training set of quantum states where the target ground state has on average the largest weight. In this section, we look at an example of a system where this can occur when applying artificial neural network-based methods.

To illustrate where the error can arise in practice and that indeed the ground state is dominant in the final result of the selected approximate method we look at the lowest energy state calculation performed by a feedforward neural

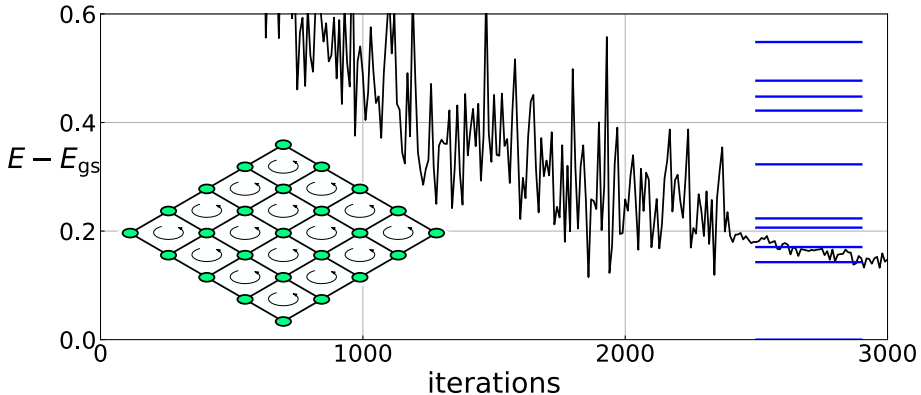


Figure 3.13: Ground state energy estimate E of a square 5×5 lattice with 4 interacting particles and homogeneous flux for a single training run of a feedforward neural network (black curve) with respect to the true ground state energy E_{gs} . The exact spectra of the lowest energy levels is denoted by horizontal blue lines for reference. The considered lattice scheme is depicted in the inset.

network for a many-body 2D square lattice problem with magnetic flux (inset of Fig. 3.13). The considered lattice is described by the dimensionless Bose-Hubbard model Hamiltonian

$$\hat{H} = - \sum_{\langle ij \rangle} e^{i\theta_{ij}} \hat{a}_i^\dagger \hat{a}_j + \frac{1}{2} \sum_i \hat{n}_i (\hat{n}_i - 1), \quad (3.22)$$

with $\hat{a}_i^{(\dagger)}$ being bosonic annihilation (creation) operator on site i and \hat{n}_i - occupation number operator on site i . The first term describes particle kinetics, i.e tunneling between neighboring sites i and j . The summation over $\langle ij \rangle$ indicates the addition of all the terms that link two neighboring sites, including their Hermitian conjugates. The complex hopping elements are defined through the position-dependent Peierls phase θ_{ij} and are chosen to produce a constant artificial magnetic flux through the lattice plaquettes. The second term is the on-site repulsion. The interplay of homogeneous flux and strong interactions is expected to give rise to topological effects such as the presence of topologically protected fractional Chern insulating states [100]. Accurate numerical computations for large systems would provide guidance on parameter selection for experimental realization and allow the possibility to probe effects related to the scaling of the system size. A lattice of N_{sites} sites occupied by $N_{\text{particles}}$ bosons will have $\frac{(N_{\text{particles}} + N_{\text{sites}} - 1)!}{(N_{\text{particles}})! (N_{\text{sites}} - 1)!}$ Fock basis elements, thus exact diagonalization algorithms become computationally intractable even for small systems ($N_{\text{particles}} \sim 1$, $N_{\text{sites}} \sim 10$). A possible solution is the use of an artificial neural network that reduces the number of coefficients required to describe the ground state and applies the Monte Carlo method to target only the relevant subspace

of low-lying energy states. We apply such a network following Ref. [60] for a 5×5 square lattice with 4 bosons and a homogeneous flux of $1/8$ flux quanta per plaquette. The chosen system size is small enough to allow a direct comparison between the neural network and the exact diagonalization results shown in Fig. 3.13. The black curve depicts the energy E convergence to the ground state energy E_{gs} for each iteration of the weight update of the network. The blue lines mark the precise lowest energy levels of the system obtained by performing exact diagonalization. We see that in this particular run of the neural network learning procedure, after 3000 iterations the energy converges only to the first excited energy. On the other hand, if we check the overlaps of the network estimated ground state $|\psi\rangle$ and the n exact lowest energy eigenstates $|\psi_{\text{gs}}\rangle, |\psi_1\rangle, \dots, |\psi_{n-1}\rangle$, we see that the contribution of the ground state is dominant in the estimate $|\langle\psi|\psi_{\text{gs}}\rangle|^2 = 0.765$, followed by the overlap with the first excited state $|\langle\psi|\psi_1\rangle|^2 = 0.124$ and the remaining small contribution consists of a mixture of higher energy states.

This is a result provided by a single run of a network learning procedure. Multiple runs form a set of ground state estimates $|\psi\rangle$ where each state is a superposition of the system's eigenstates with the highest contribution given by the true ground state. The values of coefficients in each superposition will vary due to random initialization of network weights and the random Monte Carlo sampling of states but the general tendencies given by the considered example sample run remain. Due to the variations of these states in the vicinity of the true ground state, the feedforward neural network generated set of states is a perfect candidate for the autoencoder aided analysis which should deduce a more accurate result from the approximate data.

3.3.2 Feedforward autoencoder

The analysis of the wavefunctions of interest will be done by employing a feedforward autoencoder. The goal of this artificial neural network is to encode and decode the provided input to match the output while guided by some loss function. Applications of such a network range from denoising, feature recognition and dimensional reduction to being used as a generative model [161]. In this subsection, we describe its architecture which is used in subsequent calculations for dimensional reduction in quantum systems.

The autoencoder structure is characterized by three parts. The first part is the encoder – here the provided input is compressed by decreasing network layer size for each successive layer. It is followed by a code (bottleneck) layer that consists of only a few nodes that store the latent variables describing the encoding. Finally, the decoder part unpacks the information from the code layer by increasing the number of nodes in each subsequent layer until the size of the output layer matches the size of the input layer. An example of a

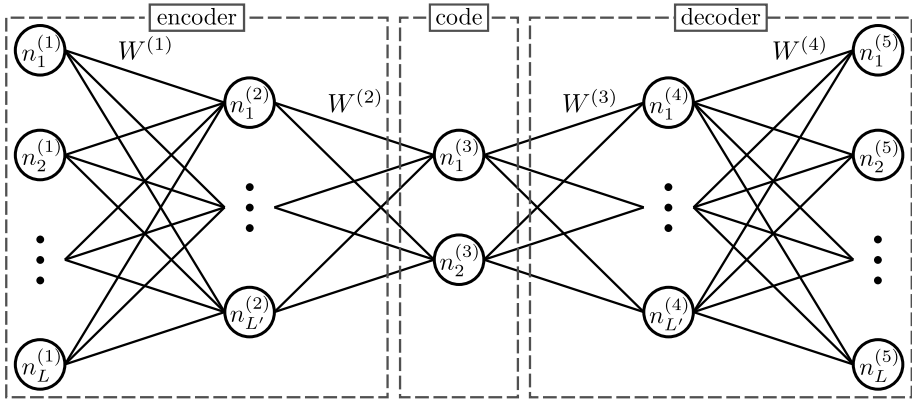


Figure 3.14: Schematic depiction of a fully connected five layer autoencoder.

five-layer autoencoder is shown in Fig. 3.14. The nodes are denoted by circles with coefficients $n_j^{(i)}$ – the superscript and subscript indicate the layer and the node index respectively. Since the number of nodes in the subsequent layers increases (decreases) in the encoder (decoder) we have that the number of nodes for the hidden 2nd and 4th layers are $L' < L$, where L is the number of input coefficients. The network is fully connected with connection weight matrices $W^{(i)}$ and the coupling coefficients are indicated by black lines connecting all nodes between each neighboring i and $i + 1$ layers.

Given an input vector $\vec{n}^{(1)} = (n_1^{(1)}, \dots, n_L^{(1)})$ the autoencoder produces an output vector following the standard feedforward model procedure. Starting from the initial data the coefficients for each subsequent layer are calculated iteratively:

$$\vec{n}^{(i+1)} = \sigma(W^{(i)}\vec{n}^{(i)} + \vec{b}^{(i)}), \quad (3.23)$$

with network weights $W^{(i)}$ and bias parameters $\vec{b}^{(i)}$. The function σ is commonly known as the activation function. It is a non-linear mapping that provides the complexity required for the network to learn. For the output to be meaningful, the network needs to be trained i.e. the network parameters $W^{(i)}$ and $\vec{b}^{(i)}$ need to be updated to produce the desired outcome given a training set. Since we are interested in dimensional reduction, the training procedure of the autoencoder aims to map the input to the output as close as possible. This corresponds to minimizing the error between the input $\vec{n}^{(1)}$ and the output $\vec{n}^{(o)}$ vectors for all training samples. To quantify the error we use the mean squared error function

$$E = \frac{1}{N_s L} \sum_{\mu=1}^{N_s} \sum_{l=1}^L \left(n_{l,\mu}^{(o)} - n_{l,\mu}^{(1)} \right)^2, \quad (3.24)$$

where we have introduced an additional subscript μ to indicated the summation over all N_s training samples. The error is minimized with respect to

the network parameters $W^{(i)}$ and $\vec{b}^{(i)}$ by employing the AdaMax optimization routine described in subsection 3.1.2 and using the standard backpropagation method [202, 203] that applies the weight and bias updates iteratively to each preceding layer starting from the last one.

The discussed fully-connected feedforward autoencoder is implemented using the Keras library [204]. Throughout this section we will consider systems that are described by normed vectors of $M \approx 500$ complex coefficients, therefore we set the node number in each autoencoder layer to follow the pattern L -100-50-25-2-25-50-100- L . For the encountered illustrative cases the number of nodes is sufficient to encode the given input, however for larger initial data, if the error function does not converge to zero, the size has to be increased at the cost of training time. Since the utilized neural network uses weights that are real numbers, the real and imaginary parts of each initial coefficient are separated into two vectors that are concatenated and provided as input of size $L = 2M$. The activation function σ is set to be the hyperbolic tangent function $\tanh(\cdot)$ for all layers since its generated output falls in the range $[-1, 1]$ which contains all possible values of the normalized vector coefficients. In each considered example the training set consists of 1000 samples and the network weights are updated for 3000 iterations. The update cutoff is chosen to prevent overfitting while the error is sufficiently converged.

A successfully trained autoencoder will store the compressed information about the training set vectors in the code layer. The goal is to analyze the distribution of the code layer coefficients for separable features that would allow to improve or generate the decoded results that surpass the initial sample set by some desired quantity.

3.3.3 Encoding the Bloch sphere

We start by analyzing the autoencoder trained with a superposition of eigenstates of a simple two-level quantum system. To gain intuition about the distribution of the code layer parameters we examine the cases for superpositions covering different sectors of the Bloch sphere.

A normalized state of a two-level system

$$|\psi\rangle = \cos\left(\frac{\theta}{2}\right)|a\rangle + e^{i\varphi}\sin\left(\frac{\theta}{2}\right)|b\rangle \quad (3.25)$$

can be represented as a point on a unit 2-sphere parametrized by the polar angle $\theta \in [0, \pi]$ and the azimuthal angle $\varphi \in [0, 2\pi)$. This sphere is called the Bloch sphere. Its poles at $\theta = 0$ and $\theta = \pi$ correspond to the orthonormal eigenstates $|a\rangle$ and $|b\rangle$ accordingly. We will be interested in three cases: when one of the states is dominant, when all possible superpositions of the two states contribute and when the samples are neglected if one of the state is highly dominant. To

generate the training set of states that have the form (3.25) for each case we uniformly sample different sectors of the Bloch sphere. Angle φ is uniformly sampled from the interval $\varphi \in [0, 2\pi)$ for all cases. The allowed range of angle θ determines the contribution of each eigenstate to the final state. The first considered case assumes that state $|a\rangle$ is dominant and restricts θ to a range $[0, \pi/2]$. It is covered by assigning $\theta = \arccos(z)$ by a random uniformly distributed variate z of interval $[0, 1]$. The sampled Bloch sector is shown in Fig. 3.15(a₁). Analogously, when all possible superpositions are present we have $\theta \in [0, \pi]$ with $z \in [-1, 1]$ covering the whole Bloch sphere (Fig. 3.15(b₁)) and when none of the states are strongly dominant $\theta \in [\pi/3, 2\pi/3]$ with $z \in [-1/3, 1/3]$ only the equator of the Bloch sphere is sampled (Fig. 3.15(c₁)). Before the training state is supplied to the autoencoder with a particular pair of parameters (φ, θ) , the eigenstates are expressed in an auxiliary MD basis $\{|\mu\rangle\}$ so that $|j\rangle = \sum_{\mu=1}^M c_{\mu}^{(j)} |\mu\rangle$ where $j \in \{a, b\}$. Without the loss of generality we can fix the global phase of each sample such that the μ' component is real, i.e. $\text{Im}\langle\mu'|\psi\rangle = 0$ for all ψ . As it turns out this improves separability of the encoded data.

The generated input, consisting of 1000 sample states in each case, is used to train the autoencoder discussed in the previous subsection. After training the network we concentrate on the code layer to analyze the encoding quality of the system. The code layer for the selected network structure consists of two nodes storing two real numbers $x \equiv n_1^{(\text{code})}$ and $y \equiv n_2^{(\text{code})}$. Their values for all generated states are plotted in Fig. 3.15(m₂-m₃) for $m \in \{a, b, c\}$. Each point (x, y) is calculated by supplying a sample state taken from the Bloch sphere sector of Fig. 3.15(m₁) to the trained autoencoder as an input. To illustrate how the represented encoding distributions can vary depending on the initialization of network weights and the generated training set, the two figures Fig. 3.15(m₂-m₃) are shown for different initial sampling of each selected Bloch sector (m₁). Evaluation of the encoding quality is aided by introducing the overlap $\mathcal{Q}_{\text{in}} \equiv |\langle a|\psi\rangle|^2$ of a sample state $|\psi\rangle$ with an exact eigenstate $|a\rangle$. The values of the overlap are depicted by color with the range shown by the colorbar. Providing exact eigenstates to the trained autoencoder we recover their position in the encoded layer marked by cyan point for state $|a\rangle$ and magenta point for state $|b\rangle$. With the established notation, each case can be now explored in detail.

Concentrating on the first column of Fig. 3.15, we see that the autoencoder for the $|a\rangle$ dominant case encodes the samples in a compact elliptical distribution (a₂) centered around the state $|a\rangle$ and well separated from the state $|b\rangle$. The encoding using a different seed of the same Bloch sector in (a₃) shows that an inverted case can occur as well – an elliptical void forms around state $|b\rangle$ while the samples are distributed around the edges of the said ellipse with a larger concentration near the state $|a\rangle$. The overlap \mathcal{Q}_{in} forms a contin-

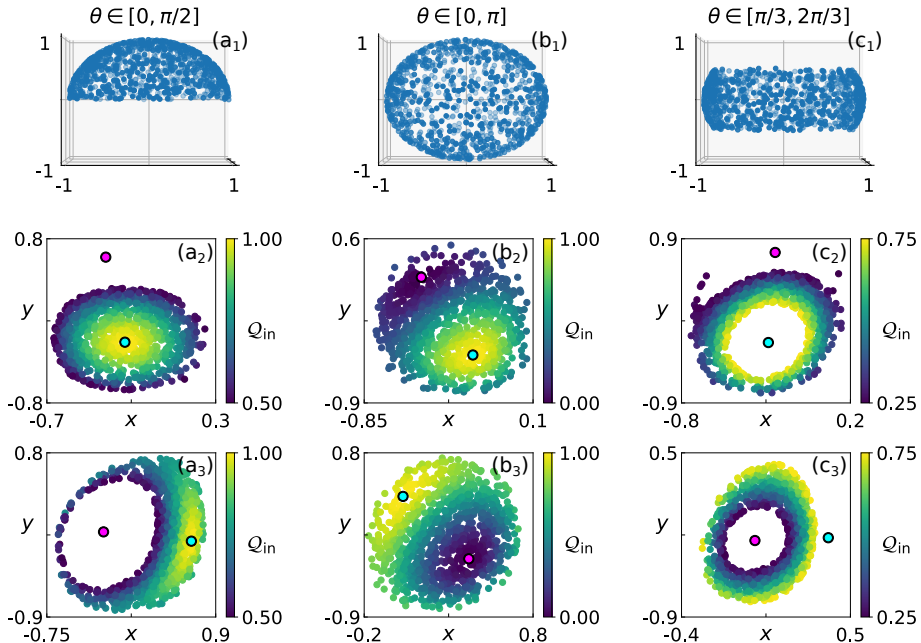


Figure 3.15: Sample distributions of the targeted Bloch sphere sectors (a_1), (b_1) and (c_1) with their corresponding encodings in the code layer (a_2), (b_2) and (c_2). The overlap of an eigenstate with a sample state $Q_{\text{in}} \equiv |\langle a|\psi\rangle|^2$ is shown by color. The cyan (magenta) point marks state $|a\rangle$ ($|b\rangle$). Figures (a_3), (b_3) and (c_3) depict the encodings of the same Bloch sectors as in the second row but with a sample set and initial network weights generated using a different seed.

uous gradient indicating that each superposition is systematically separated. The middle column of Fig. 3.15 describes the encoding of the whole uniformly sampled Bloch sphere. Subplots (b_2) and (b_3) show a circular distribution of encoded samples in the parameter space of the code layer. Both of the eigenstates lie within the distribution and the overlap shows a clear distinction between the regions where each of the eigenstates dominate. Finally, the third column of Fig. 3.15 focuses on superpositions where both of the eigenstates have similar contributions. The resulting encoding is consistent with previous observations – if the dominant samples mapped close to the eigenstates were to be subtracted from the encoding presented for the fully sampled Bloch sphere we would obtain ring-like distributions seen in (c_2) and (c_3). Note that due to the random initialization of the simulation and the symmetry of the sampling either state $|a\rangle$ or $|b\rangle$ can end up at the center of the ring-like distribution as shown by the overlap of two different seeds. It is important to stress that the overlap is an external parameter that assumes the knowledge of the exact eigenstate. While it aids the analysis of the encoding it is not available when

tackling the problem of ground state determination. One way to extract the information would be by looking at the geometric properties of the distribution provided the sampling is not uniform, e.g. in the two-level system, we see that when one state is dominant (a_2), the ground state could be found by taking the center of the ellipse. An alternative would be to scan the code layer and subject the output state generated by each point (x, y) to some goal function which when extremized would determine the code space point giving the optimal output (e.g. find the output state that produces the energy minimum by exploring the code layer parameters).

We have analyzed the encoding of a two-level system for various samplings of the Bloch sphere which provided an overview of how the code variables behave for a simple, well-controlled study case. The gained intuition will be useful when considering the system we initially set out to explore – a system that hosts multiple energy levels described by a set of approximate lowest energy solutions with a dominant ground state contribution. In the next subsection, we define the model that generates the training set for such a system with a small number of controllable parameters.

3.3.4 Sample set generation with dominant ground state

In subsection 3.3.1 we found good candidates for a set of training states for an autoencoder by exploring a specific problem and method. Now we would like to consider a general model which does not depend on a particular problem and only relies on the dominance of the ground state in the estimated solution.

Let a sample state have the form

$$|\psi\rangle = \sum_{j=1}^N w_j^{\frac{1}{2}} e^{i\varphi_j} |j\rangle, \quad (3.26)$$

where w_j is the weight contribution of the $|j\rangle$ orthogonal basis state with a uniformly sampled random phase factor $\varphi_j \in [0, 2\pi)$. The set of states $\{|j\rangle\}$ spanning the ND Hilbert space is the solution obtained by diagonalizing the Hamiltonian of a specific problem, one of the states being the ground state we are looking for. In general these states can be expressed in some convenient MD basis $\{|\mu\rangle\}$ (e.g. configuration space elements):

$$|j\rangle = \sum_{\mu=1}^M c_{\mu}^{(j)} |\mu\rangle, \quad (3.27)$$

with probability amplitudes $c_{\mu}^{(j)}$. Although the states are determined by a distinct problem, the encoding exhibits universal behavior as asserted by considering different systems with $M \approx 500$ sites/configurations. States obtained by solving 23×23 single-particle square lattice tight-binding problem ($M = 529$)

with and without uniform flux of $1/8$ flux quanta piercing the plaquettes, many-body problem of a 3×3 square lattice with 4 bosons ($M = 495$) described by Hamiltonian (3.22) and orthogonal complex vectors obtained via reduced QR decomposition ($M = 500$) all give similar grouping of the code variables in the autoencoder provided that the weights w_j follow the same distribution. Following this observation we restrict our analysis of the code variable layer by considering orthogonal vectors generated from a random complex matrix A . The matrix A consists of $M \times N$ complex elements with real and imaginary parts sampled uniformly from an interval $[-1, 1]$. By performing reduced QR decomposition of A we get N orthogonal vectors $\vec{c}^{(j)} = (c_1^{(j)}, \dots, c_M^{(j)})$ which form the set of basis states $\{|j\rangle\}$. Having the basis at hand we are left to choose the weight w_j generation method for each sample state.

The weights need to satisfy the normalization condition $\sum_j w_j = 1$ and have a dominant value for the ground state with decaying values for higher energy excited states. A natural choice that preserves the normalization is the random division of the unit interval method [205]. The idea is to randomly draw $N - 1$ points from some probability density function $f(x)$ with domain $[0, 1]$ that divide the interval $[0, 1]$ into N subintervals. The length of a subinterval

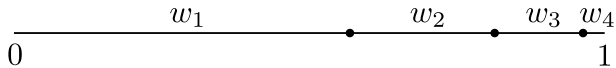


Figure 3.16: Division of the unit interval by $N - 1 = 3$ points generated from the probability density function $f(x) \propto x^2$. The length of the $N = 4$ subintervals gives the values of the weights w_1, \dots, w_4 .

corresponds to a weight w_j . Choosing the probability density function to be $f(x) \propto x^p$ with $p > 0$ guarantees the existence of a structure with subintervals of on average decreasing length. Typically the subinterval closest to zero will be the longest hence we map the weights w_1, w_2, \dots, w_N to the subinterval lengths going left to right on the interval $[0, 1]$ as illustrated in Fig. 3.16. For the selected labeling the ground state is associated with $|j = 1\rangle$ and the excited states are $|j = 2\rangle, \dots, |j = N\rangle$.

The described construction of a sample state (3.26) allows generating a training set of vectors that depends only on two parameters – the number of eigenstates N which give non-zero overlap with the sample state and the parameter p of the chosen probability density function which describes how fast the contribution of excited states decays. This set will serve as a tool to probe the encoding/decoding capabilities of the autoencoder for a different number of states and varying contributions of eigenstates in the sample state while keeping the ground state weight dominant.

3.3.5 Endcoding few-level systems

Let us consider few-level systems where the main contribution to the noisy sample state comes from $N \in \{2, 5, 50\}$ eigenstates. The key assumption is that the ground state has a large contribution in the sample state compared to the remaining excited states. The training set that contains such samples is generated using the random division of the unit interval to assign weights to the eigenstates as described in the previous subsection. We will look at the encoding properties of the autoencoder when the power-law exponent p determining the eigenstate weight distribution in a sample is $p = 2$ or $p = 10$ and the basis states (3.27) are generated via QR decomposition on a support basis of $M = 500$ elements.

The main results of a trained autoencoder are shown in Fig. 3.17. The same autoencoder structure is used as in the Bloch sphere encoding case. The plots depict the code layer parameter (x, y) distribution of a 1000 sample states, where the first column of subplots is obtained for $p = 2$ and the second column for $p = 10$. Each row considers different number of contributing eigenstates in the sample: first row – $N = 2$ (Fig. 3.17(a-b)), second row – $N = 5$ (Fig. 3.17(c-d)) and third row – $N = 50$ (Fig. 3.17(e-f)). The mapping of the exact ground state $|1\rangle$ to the code layer parameter space is depicted by the cyan point, the first excited state $|2\rangle$ is marked by a magenta point and the remaining $|3\rangle, \dots, |N\rangle$ excited states in Fig. 3.17(c-f) with smaller contributions are shown by red points. The overlaps of samples with the ground state $Q_{\text{in}} = |\langle 1|\psi\rangle|^2$ are depicted by color.

First, let us focus on the two-level systems in Fig. 3.17(a-b). In both $p = 2$ and $p = 10$ cases the samples are well separated based on their overlaps, clustering near appropriate eigenstates. The main difference between (a) and (b) is the overlap range due to the different power-law statistics. For $p = 2$ we have that the weight contribution to the sample state on average is $3/4$ for the ground state $|1\rangle$ and $1/4$ for the excited state $|2\rangle$. Meanwhile, for $p = 10$ the corresponding mean weights of the ground and excited states are 0.917 and 0.083, hence in this case the sample distribution is denser near the ground state with overall larger overlaps. The observed distributions are consistent with the results seen in the Bloch sphere encoding. Moving on to systems with $N = 5$ contributing states, in Fig. 3.17(c-d) we see that the ground state (cyan) and the first excited state (magenta) are clearly separated in the encoding space with the higher excited states (red) located in-between. The noisy overlap distribution in Fig. 3.17(c) arises due to the five eigenstates, that compose each sample, having comparable mean weights ranging between 0.074 and 0.534. Therefore it is harder for the autoencoder to separate higher-dimensional data with comparable information content (weights) in the 2D code layer. In (d) the ground state has a much larger contribution (with a weight 0.832) compared

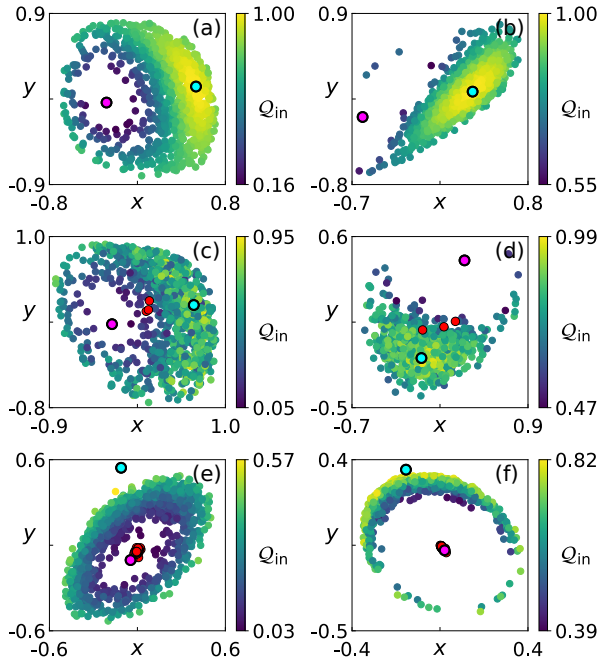


Figure 3.17: Sample distributions of systems with $N = 2$ (a-b), $N = 5$ (c-d) and $N = 50$ (e-f) eigenstates contributing to the superposition of the sample. The first column shows the encoding of samples with weights generated by the power-law with exponent $p = 2$ and the second column – $p = 10$. Color of the colorbar denotes the overlap of a sample and exact ground state. Encoding of the exact ground state is marked by a cyan point, first excited state – magenta point and higher excited states – red points.

to the excited states thus the neighboring overlaps in parameter space vary mildly which is reflected in the range of the overlaps as well. Similar results are observed for $N = 2, 3, 4$. If the contributing state number is increased considerably, e.g. $N = 50$, then the typically observed encoding is depicted in Fig. 3.17(e-f). The ground state and all of the excited states are separated into two regions by a ring-shaped distribution of sample states. Calculating the mean weight of the ground state in the sample states gives 0.243 for $p = 2$ (e) and 0.67 for $p = 10$ (f) with the remaining exciting states having a significantly smaller impact. This is similar to the Bloch sphere case when the samples did not have a dominant contribution from either of the eigenstates leading to isolated exact ground and excited states. The inclusion of many additional excited eigenstates here does not change the picture qualitatively – their small contributions translate to the lack of information content which leads to their clustering in the center of the ring.

The general features seen in the two-level system are reflected in the few-level systems studied above which exemplify the universality of the encoding.

For $N = 5$ the presence of noisy overlap encoding arises due to comparable contributions of eigenstates in the samples. This does not cause problems for decoding the ground state provided one of the eigenstates is dominant as we shall see in the next subsection. In general, one can relax the restriction of having only two nodes at the code layer which can improve separability at the cost of universality in the sense that an additional network meta parameter controlling the code layer size is introduced which is tuned depending on the system.

3.3.6 Decoding few-level systems

Structurally we have addressed the encoding part of the autoencoder which describes the separability of features in the code layer given an initial set of states. This was done by inspecting the encoded distribution of overlaps of input samples and the exact ground state. We now analyze the decoding part to see if it can generate an improved ground state estimate. The decoding is firstly considered by taking overlaps between the output and the input states to assess the accuracy of the one-to-one correspondence between them. Secondly, the overlap of the output and the exact ground state is calculated to evaluate if the ground state can be recovered by sampling the code layer variables.

The first quantity we consider is the overlap of an arbitrary sample state $|\psi\rangle$ and the output state $|\psi_{\text{out}}\rangle$ it produces after being propagated through the autoencoder. It is denoted by $\mathcal{Q} \equiv |\langle\psi_{\text{out}}|\psi\rangle|^2$ that represents the accuracy of the bijective mapping between the states by the autoencoder. The second quantity is the overlap $\mathcal{Q}_{\text{out}} \equiv |\langle 1|\psi_{\text{out}}\rangle|^2$ between the ground state $|1\rangle$ and the output state. It is referred to as decoding quality since it provides information about the ability of the neural network to reproduce the ground state, e.g. if $\mathcal{Q}_{\text{out}} = 1$ for some pair of code layer variables, then the exact ground state is recovered. To illustrate the typical decoding properties we use the trained autoencoder of the previous subsection that produced the encoded sample distribution shown in the first column of Fig. 3.17. The accuracy \mathcal{Q} and quality \mathcal{Q}_{out} are depicted in Fig. 3.18 for samples with $N = 2$ (a,b), $N = 5$ (c,d) and $N = 50$ (e,f) eigenstates contributing to the superposition. The decoding quality values are obtained by sampling the code layer parameter pairs $(x, y) \in [-1.5, 1.5] \times [-1.5, 1.5]$ with both intervals uniformly discretized to a 100 points. The point of the code layer variables that results in the largest value of \mathcal{Q}_{out} is marked by '+'. The coloring of the points representing the ground state and the excited states in the code layer parameter space is the same as in the encoding case.

Starting with the $N = 2$ system we see that the input and the output states are mapped to each other almost identically with \mathcal{Q} ranging between 0.99 and 1 (Fig. 3.18(a)) which is expected since the initial weight data matches the

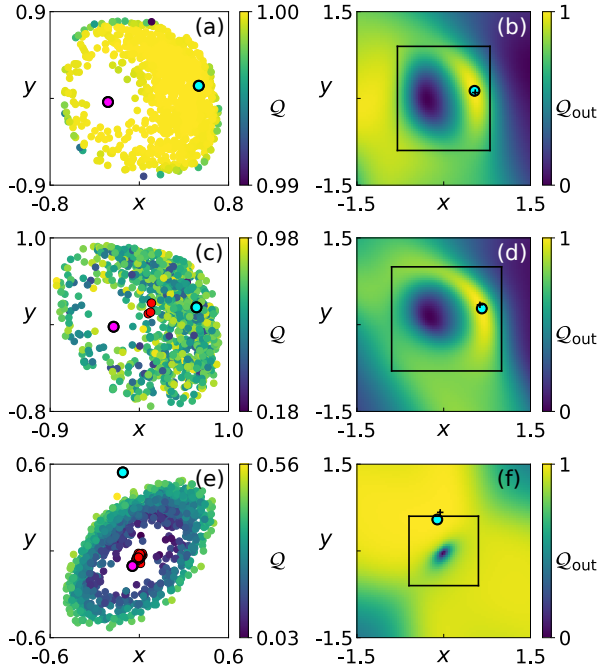


Figure 3.18: The decoding accuracy $\mathcal{Q} = |\langle \psi_{\text{out}} | \psi \rangle|^2$ and quality $\mathcal{Q}_{\text{out}} = |\langle 1 | \psi_{\text{out}} \rangle|^2$ of the autoencoder trained with samples composed of $N = 2$ (a,b), $N = 5$ (c,d) and $N = 50$ (e,f) contributing eigenstates. The weights are generated using random division of unit interval for $p = 2$ case. Cyan point marks the ground state, magenta – first excited and red – higher excited states. Symbol '+' denotes the maximum of \mathcal{Q}_{out} . Black borders in the second column indicate the sample region of the first column.

dimensionality of the code layer. The decoding quality \mathcal{Q}_{out} is close to unity and the code layer point '+' corresponding to the predicted optimal decoding value almost exactly coincides with the cyan point representing the encoded ground state (Fig. 3.18(b)). For $N = 5$, the accuracy \mathcal{Q} in Fig. 3.18(c) mimics the noise seen in the encoding analysis due to multidimensionality of weights mapped to a 2D code layer, indicating that the initially encoded state does not necessarily map to the same state after decoding, however the decoding quality \mathcal{Q}_{out} in Fig. 3.18(d) covers the whole range of possible overlaps hence the improved ground state estimate can be reconstructed. Finally, for $N = 50$ the decoding accuracy \mathcal{Q} is almost identical to the \mathcal{Q}_{in} values in Fig. 3.17(e) that depict the overlaps of encoded states with the ground state. This suggests that the output states might be close to the ground state which is indeed the case as seen from the decoding quality in Fig. 3.18(f). Unlike the previous few-state systems, the current one has broad regions of high decoding quality. This is because it becomes easier for the autoencoder to interpret the high

variability of the weights of many excited eigenstates in each sample as noise and separate it from the consistently large ground state contribution.

The decoding analysis of the autoencoder shows that it is possible to obtain an improved ground state estimate by sampling the code layer parameters. However, it does not provide a direct way to find the feature space variables that generate the best improvement. In the next subsection, a few examples are given of how the optimal point can be found for a 2D square and quasi-1D sawtooth lattices by minimizing the energy with respect to the code layer parameters.

3.3.7 Application: square and sawtooth lattices

To illustrate the ground state reconstruction capabilities of the autoencoder we consider that it is trained using a noisy set of superpositions of the lowest energy eigenstates of either a 2D square or a quasi-1D sawtooth lattice. The improved ground state estimate is calculated by sampling the code layer variables guided by the minimization of the energy of the system.

The simple 2D square lattice is described by the single-particle tight-binding Hamiltonian

$$\hat{H} = -J \sum_{\langle ij \rangle} \hat{a}_i^\dagger \hat{a}_j, \quad (3.28)$$

with J characterizing the hopping parameter along directed links $\langle ij \rangle$ connecting the nearest-neighboring lattice sites and $\hat{a}_j^{(\dagger)}$ being the particle annihilation (creation) operator at site j . We will be interested in the qualitative comparison of on-site densities between the exact and autoencoder estimated ground state, therefore it is useful to recall that the density of some state $|\phi\rangle$ at a site j is defined as the expectation value of the usual particle number operator $\langle \hat{n}_j \rangle \equiv \langle \phi | \hat{a}_j^\dagger \hat{a}_j | \phi \rangle$.

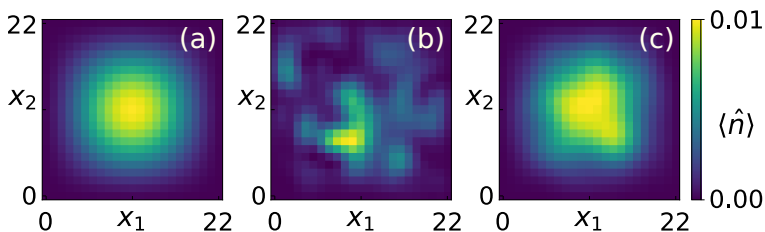


Figure 3.19: (a) Exact ground state density $\langle \hat{n} \rangle$ of a 23×23 site lattice. (b) Density of the initially generated sample that has the largest overlap with the ground state. (c) Density of the optimal state produced by the autoencoder based on energy minimization.

For numerical computations, a 23×23 site lattice with the open boundary condition is used and the hopping parameter is set to $J = 1$. The sites are

indexed by their spatial coordinate (x_1, x_2) with $x_1, x_2 \in \{0, 1, \dots, 22\}$, assuming that the lattice spacing is unity. Solving the eigenvalue problem of the finite lattice Hamiltonian we see that the ground state of this system is a product of two sine functions forming the density profile $\langle \hat{n} \rangle$ shown in Fig. 3.19(a). Our goal is to recover this density while initially having a noisy set of sample states. A thousand sample states $|\psi\rangle$ are constructed as superpositions of the first 50 lowest energy eigenstates of the square lattice with eigenstate weights assigned using the random division of unit interval method. The points that divide the interval are drawn from the power-law probability density function of the power $p = 2$. The autoencoder is trained using the generated sample set for 3000 weight updates while its layer structure remains as before. Fig. 3.19(b) shows the density of the sample producing the largest overlap with the ground state. It clearly does not resemble the density of the lowest energy state. To get the improved ground state estimate we require some additional information about the system that would allow us to evaluate the output's closeness to the target state. The obvious choice is the energy since it is computationally efficient to calculate and the lowest energy state should be close to the ground state. We minimize the energy $E = \langle \phi_{\text{out}}(x, y) | \hat{H} | \phi_{\text{out}}(x, y) \rangle$ of the system with respect to the code layer variables (x, y) that produce the state $|\phi_{\text{out}}(x, y)\rangle$. The optimal code layer point $(x_{\text{min}}, y_{\text{min}})$ is calculated using the AdaMax optimizer described in subsection 3.1.2 and the density of the corresponding optimal state $|\phi_{\text{out}}(x_{\text{min}}, y_{\text{min}})\rangle$ is depicted in Fig. 3.19(c). Although the result is not perfect, it is a drastic improvement compared to the initially given samples.

The second system we explore is the flat-band quasi-1D sawtooth lattice at the quarter-filling regime that we have encountered in subsection 3.2.1. It poses additional challenge since it includes interactions and the support basis is composed of more configurations compared to the square lattice case. Recalling the Hamiltonian terms (3.13) and (3.16) describing this lattice

$$\hat{H} = \hat{H}_0 + \hat{H}_{\text{int}} = \left(-J \sum_{\ell=1}^L \hat{a}_{\ell}^{\dagger} \hat{a}_{\ell-1} - J' \sum_{j=1}^{L/2} \hat{a}_{2j}^{\dagger} \hat{a}_{2j-2} + \text{h.c.} \right) + \frac{U}{2} \sum_{\ell=0}^L \hat{n}_{\ell} (\hat{n}_{\ell} - 1), \quad (3.29)$$

we select a system of $L+1 = 17$ sites with open boundaries and 4 particles. The hopping parameters are set to $J = \sqrt{2}|J'|$ and $J' = -1$ which realizes the flat energy band at the bottom of the energy spectrum. The interaction strength is chosen to be $U = 0.1$. This selection produces the previously analyzed ground state density wave structure (Fig 3.2(a)) which is plotted once again for convenience with respect to the site index x_1 in Fig. 3.20 (black squares).

To test the autoencoder's ground state reconstruction capability, we first repeat the noisy sample state set generation in the same manner as we did for the square lattice. The autoencoder structure, node count and training procedure are unchanged. For reference, we check the density of the sample

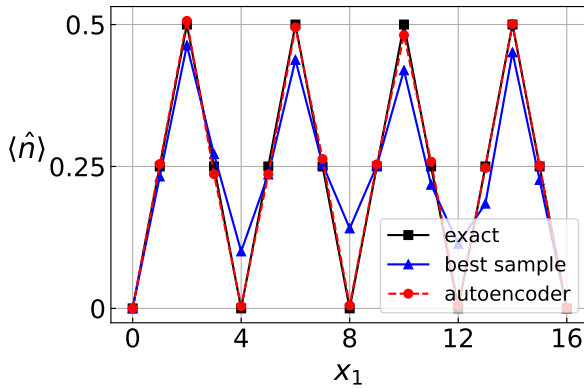


Figure 3.20: Spatially dependent density of the exact ground state of the quarter-filled 17 site sawtooth lattice (black squares), density of the sample giving the largest overlap with the ground state (blue triangles) and density of the ground state estimate produced by the autoencoder (red circles).

that produces the best overlap with the ground state depicted by blue triangles in Fig. 3.20. It fails to capture the isolated nature of the density islands. Using energy minimization as before, the autoencoder constructs the ground state estimate represented by red circles in Fig. 3.20. It achieves significant improvement and recognizes the main feature – separation of localized densities.

In both considered lattices the autoencoder successfully improved the ground state estimate having only a noisy set of states to work with. Note that even though the support basis of the many-body sawtooth lattice is much larger ($M = 4845$ configurations) than the previously considered systems, e.g. square lattice ($M = 529$), it does not qualitatively impact the reconstruction of the ground state, which emphasizes the universality of the autoencoder.

3.3.8 Summary

Approximate ground state determination methods provide the solution of the eigenvalue problem up to a certain error which originates either from inherent randomness or truncation procedure of the method. Autoencoder-based secondary analysis of the set of the approximate ground states offers a possibility to improve the final result. To this end, the encoding and decoding capabilities of the autoencoder featuring a two-node code layer were explored, guided by the key assumption that the ground state contribution is dominant in the superpositions of the lowest-lying eigenstates forming the initially provided solutions. For input states satisfying this condition, the encoding displayed universality and efficiently separated the states based on their ground state contribution regardless of the number of contributing eigenstates. This is reflected by the generated output obtained by sampling the code layer variables – nearly all of

the range of overlaps between the output states and the lowest energy state is covered. Although the trained autoencoder is able to represent the target state, there is no straightforward way to obtain the optimal result from the initial data alone. A way to quantify the search is to select a goal function that is optimized over the code layer parameters. Choosing to minimize the energy which should lead to the lowest-lying eigenstate, two systems were considered – a square and a quasi-1D sawtooth lattices. After optimization, the ground state estimate was significantly improved in both cases compared to the initially supplied sample states.

CONCLUSIONS

In the first part of this thesis, we have proposed a novel type of system coined as the time-space crystalline structure that exhibits periodicity in both space and synthetic temporal dimension arising from the resonant periodic driving of the lattice. We have established the quantum description of such a system guided by the insights acquired from the classical picture and provided an explicit example of how to construct a quasi-1D time-space crystalline structure. A generalization to 4D and 6D structures was provided as well. From these results we form the first statement of the thesis:

1. A resonantly periodically driven lattice supports a parameter regime that realizes a time-space crystalline lattice – a spatial lattice equipped with periodic temporal structure at each site acting as a synthetic dimension.

Employing additional potential driving modulation an energy offset is created that suppresses tunneling between different temporal lattice sites. The introduction of Raman laser beams restores the couplings and in addition imprints a controllable phase to the hopping parameters. The control of these phases allows to create plaquette-piercing artificial magnetic fluxes that are key to the presence of topological phenomena. This is illustrated by the presence of topologically protected edge states in the 6D time-space crystalline structure. It leads to the second statement:

2. Time-space crystalline structures offer a platform to probe topological properties in six dimensions.

The second part of the thesis first considered the ability of an artificial neural network with restricted Boltzmann machine architecture to learn the ground-state features of flat dispersion band models. The learning procedure was based on minimizing the energy of the system. Quasi-1D sawtooth and finite 2D kagome lattices were taken as models to be learned by the network. Both systems exhibit global density wave-type ground state structure which the neural network successfully learned, however, local features were recognized with lower fidelity. This allows us to form the third statement:

3. Artificial neural networks with restricted Boltzmann machine architecture successfully encode the global structure of the ground state of dispersionless band lattice models while only guided by the energy minimization.

For large systems there is a higher chance for the observed parameters to fail to converge and get trapped in a local energy minimum, requiring a re-initialization of the learning procedure. This is caused by global structure formation at different local regions which upon touching form a defect in the density wave. Restoration of the ordered structure requires a global rearrangement of densities of one of the clashing regions. This is energetically highly unfavorable and the learning procedure fails to escape such a configuration, hence we state that:

4. Restricted Boltzmann machines are prone to getting stuck at a density configuration corresponding to a local energy minimum for large systems.

Finally, a different neural network architecture was explored as a means of secondary data analysis. An autoencoder was utilized to filter out the ground state from a given collection of sample states that are superpositions of lowest energy eigenstates with the ground state providing on average the largest weight. The trained autoencoder encoded sufficient information about the initial data to reconstruct an improved ground-state estimate which has an overlap close to unity with the exact result. Thus we conclude that:

5. Autoencoder-aided analysis allows one to extract an improved ground-state estimate based on a set of noisy states with a dominant ground-state contribution.

ACKNOWLEDGEMENTS

First and foremost, I would like to thank my scientific supervisor Prof. Egidijus Anisimovas, who introduced me to the field of ultracold atom gases and guided through its intricacies in a clear and concise manner. This thesis would not have seen the light of day without him.

I thank my colleague and friend Mantas Račiūnas for the countless discussions, collaboration and the shared journey through the study of physics since the bachelor years.

I am grateful to Prof. Krzysztof Sacha and Chu-Hui Fan for the opportunity to explore time crystal phenomena together.

I thank Prof. Gediminas Juzeliūnas, Hamid R. Hamed, Viktor Novičenko and Mažena Mackoit-Sinkevičienė for the collaborations together.

I thank Andrius Gelžinis, Prof. Thomas Gajdosik, Jevgenij Chmeliov, Vytautas Dūdėnas, Augustinas Stepšys, Vytautas Bubilaitis and Simonas Draukšas for the fun times at the gravitation and physical kinetics seminars.

Personal thanks to my friends David, Marvin Mayer, Parvez, Marina, Rich, Rob, Jeff Shupe, Andriy, Zara, Andy, Sophie Klein, Alyssa Tiffin, Daniel Bi and Ethan Thorpe for all the encouragement during the years of studies.

Finally, I thank my parents Irena and Artūras for all the support throughout my life.

SANTRAUKA LIETUVIŲ KALBA

Įvadas

Šaltųjų atomų sistemos yra sudarytos iš atšaldytų neutralių atomų dujų, kurių temperatūra yra mažesnė už dešimtis mikrokėlvinų. Šios dujos yra laikomos tiksliai valdomose elektromagnetinėse gaudyklėse. Keičiant gaudyklių parametrus įmanoma tirti įvairius kvantinius efektus, išvengiant problemų atsirandančių dėl priemaišų ir defektų įprastuose medžiagų bandiniuose.

Bose Einstein kondensato sukūrimas 1995 m. [1, 2] žymi intensyvių tyrimų pradžią šaltųjų atomų sistemų srityje. Pirmuosiuose eksperimentuose atominių dujų debesis buvo pagaunamas magnetinėje gaudyklėje ir šaldomas pasitelkiant naujus lazerinio vėsinimo ir aukščiausių energijos dalelių išgarinimo metodus. Tai leisdavo pasiekti itin šaltas temperatūras ir sukurti egzotišką medžiagos būseną, kurioje dominuoja kvantiniai efektai. Šie eksperimentai patvirtino Bose ir Einstein teorinius skaičiavimus atliktus XX a. pirmoje pusėje [3, 4] bei paskatino tolimesnius supertakios medžiagos tyrimus (kolektyvinius svyravimus [5], kvantuotų sūkurių susidarymą [6], Josephson tipo efektus [7]). Po sėkmingų bozoninių dujų eksperimentų sekė fermioninių kondensatų bandymai: 1999 m. analizuoti judesio kiekio pokyčiai ^{40}K atomų dujose, atsirandantys dėl Pauli draudimo principo [8], užfiksuotas supertakumas, kurį prognozavo Bardeen-Cooper-Schrieffer teorija [9]. Išsami fermioninių dujų eksperimentų ir teorijos apžvalga pateikiama [10].

Sekantis žingsnis šaltųjų atomų dujų tyrime buvo skirtingų gaudyklių formų išbandymas – pradėti kurti periodiniai potencialai leidžiantys simuliuoti kietųjų kūnų struktūrą. Pagrindinis įrankis, leidžiantis sukurti periodines struktūras tokiose ekstremaliose sąlygose yra optinės gardelės. Optinės gardelės – interferuojančių lazerių pluoštų intensyvumo skirstinys pasižymintis erdviu periodiškumu [11]. Tokioje gardelėje atomai sąveikauja su šviesa per elektrinio lauko ir atomo dipolinio momento sąveiką, kurios dėka atomai pagaunami periodiniuose šviesos intensyvumo maksimumuose arba minimumuose, priklausomai nuo poliarizuojamumo. Tokie šviesos kristalai sulaukia didelio dėmesio, nes jie gali būti panaudojami kaip daugiadaleliniai kvantiniai simulatoriai pasiūlyti

Feynman 1982 m. [12, 13]. Reguluojant lazerių pluoštų konfigūraciją galima sukurti įvairių geometrijų gardeles, tuo tarpu keičiant lazerio intensyvumą, parenkama dalelių tuneliavimo sparta tarp gardelės mazgų bei modifikuojama tarpdalelinė sąveika. Tikslus šaltųjų atomų gardelę aprašančių parametru kontroliavimas ir mažas kiekis defektų leidžia lengvai išbandyti teorinius modelius eksperimentuose. Dažnai nagrinėjamų modelių pavyzdžiai yra Hubbard tipo modeliai [14–17] aproksimuojantys sąveikaujančių fermionų ir bozonų elgesį gardelėje. Fermi-Hubbard modelis suteikia įžvalgų aukštos temperatūros superlaidininkų tyrime [18, 19] bei nagrinėja kvantines sukinių sistemas [20]. Bose-Hubbard hamiltonianai gali būti naudojami kvantinių fazinių virsmų aprašymui bozonų dujose [21–23]. Optinių gaudyklių ir gardelių universalumas taip pat atveria galimybes sukurti naujas medžiagos formas, tokias kaip diskretaus laiko kristalai [24, 25], fazinės erdvės kristalai [26] ir superkietieji kūnai [27, 28].

Kondensuotų medžiagų fizikoje įprasta tirti sistemos atsaką patalpinant bandinį į išorinį magnetinį lauką. Tuo tarpu šaltųjų atomų dujos yra neutralios, todėl magnetiniai efektai turi būti indukuoti alternatyviais būdais. Vienas iš metodų yra periodinis sistemos purtymas [29, 30], kuris sukelia Coriolis tipo jėgą, sukuriančią dirbtinį kalibruotės lauką ekvivalentų magnetiniam laukui. Kitas būdas yra panaudoti Raman [31, 32] arba optinio laikrodžio šuolius [33], suteikiančius dalelių banginėms funkcijoms fazę, kurią jos įgytų judėdamos magnetiniame lauke. Šie įrankiai, sukuriantys efektyvų magnetinį lauką leidžia šaltųjų atomų sistemose nagrinėti kvantinį Hall efektą [34, 35] bei topologines medžiagos formas [36–38] atsparias išoriniams trikdžiams. Tokių sistemų tyrimas tiksliai valdomoje aplinkoje yra svarbus žingsnis įgyvendinant topologinius elektroninius prietaisus [39] bei prisideda prie potencialaus taikymo kvantinių skaičiavimų srityje [40].

Šaltųjų atomų dujos optinėse gardelėse taip pat suteikia prieigą prie aukštesnių dimensijų fizikos. Vidiniai sistemos laisvės laipsniai, pvz. dujas sudarančių atomų sukabintos vidinės būsenos ar sukininiai laisvės laipsniai gali būti išnaudoti kaip papildoma sintetinė dimensija. Tai leidžia tirti keturmatį [43, 44] arba net šešiamatį [45] kvantinį Hall efektą, kuris yra reikšmingas kvazikristalų topologijos supratimui [46], laiko apgražai invariantiškų izoliatorių nagrinėjime [47] bei kituose egzotiniuose reiškiniuose [48, 49].

Šaltųjų atomų gardelių visapusiškumas verčia tobulėti ir skaitmeninius metodus. Iš vienos pusės, analitiniai ir skaitiniai skaičiavimai padeda atpažinti parametru režimus, kuriuose pasireiškia įdomios medžiagos fazės ir kartu užduoda eksperimentinių tyrimų linkmę. Iš kitos pusės, besiplečiančios eksperimentinės galimybės suteikia daugiau valdomų parametru, leidžiančių sukurti sudėtingesnes sistemas, kurių stebėjimų tikrinimui ir lyginimui su teoriniais modeliais reikia vis daugiau skaičiavimo resursų. Analitinės aproksimacijos turi ribotas galiojimo ribas [50, 51], todėl norint spręsti daugiadalelinius uždavinius tenka taikyti skaitinius metodus, kurie yra nuolat tobulinami siekiant didesnio

tikslumo bei pritaikomumo didesnėms sistemoms [52]. Mažų gardelių su keilomis dalelėmis žemiausios energijos būsenos sėkmingai suskaičiuojamos pasitelkiant tikslios diagonalizacijos algoritmus [53]. Didesnėms sistemoms tenka taikyti tenzorinių tinklų metodus [54, 55], kvantinį Monte Carlo metodą [56] ar net neuroninius tinklus [57–61]. Konkretaus metodo parinkimas priklauso nuo sprendžiamos problemos specifikos.

Šios disertacijos tikslas yra dvilypis, paliečiantis tiek analitinius, tiek skaitinius šaltųjų atomų dujų fizikos aspektus. Pirmas tikslas yra pritaikyti diskrečių laiko kristalų idėjas periodiškai purtomoms optinėms gardelėms ir sukurti efektingą daugiamatę gardelę, kurią vadinsime laiko-erdvės kristaline struktūra. Tokia sistema potencialiai leistų nagrinėti topologinius efektus šešiamatėje erdvėje. Antras tikslas yra skaitmeniškai ištirti neuroninių tinklų taikymą kvazivienmačių gardelių (vienmačių gardelių, sukabintų į baigtinio pločio juostą) ir dvimačių gardelių segmentų savybių nustatymui.

Darbo tikslai ir sprendžiami uždaviniai

Pirmas darbo tikslas yra pasiūlyti gardelės modelį su sintetinė laike dimensija – laiko-erdvės kristalinę struktūrą, kuri leistų tirti fizikinius procesus gardelėse, turinčiose iki šešių dimensijų bei parodyti, kad tokia sistema gali pasižymėti topologinėmis savybėmis. Šiam tikslui pasiekti yra iškelti atitinkami uždaviniai:

- Ištirti laikinio periodiškumo struktūros kilmę viename iš rezonansiniu dažniu purtomo sinuso kvadrato formos potencialo minimumų, pasitelkiant klasikinės Hamiltono mechanikos formalizmą.
- Įvesti kvantinį sistemos aprašymą, kuriame sukabinama laikinė struktūra kiekviename erdvėje periodinės gardelės minimume su struktūromis, esančiomis gretimuose gardelės mazguose, taip suformuojant kvazivienmatę gardelę.
- Pritaikyti periodiškai rezonansiniu dažniu purtomos gardelės potencialą efektingai daugiamatės gardelės sukūrimui.
- Sukurti dirbtinį magnetinį srautą, kuris kerta laiko-erdvės kristalinės gardelės elementariusius narvelius bei ištirti topologinių efektų pasireiškimą, pasitelkiant lazeriu indukuotus dalelių šuolius ir tiesinį gardelės potencialo išderinimą.

Antras tikslas yra ištirti dirbtinių neuroninių tinklų taikymo galimybes žemiausių energijos būsenos radimui bei stebimų dydžių nustatymui ribotos geometrijos gardelėse. Uždaviniai šiai problemai spręsti yra:

- Pasirinkti tinkamą dirbtinio neuroninio tinklo architektūrą ir tinklo koeficientų optimizavimo algoritmą.

- Pasirinkti tiriamus gardelės modelius, kurie pasižymėtų netrivialiomis savybėmis, bet kartu turėtų žinomus analitinius sprendinius, leidžiančius įvertinti tinklo rastų rezultatų tikslumą.
- Ištirti lokalių ir globalių dalelių tankio pasiskirstymo bruožus, parenkant įvairius tinklo ir gardelių modelių parametrus.
- Patikrinti kaip keičiasi charakteringų dydžių konvergavimo sparta didinant sistemą.

Mokslinis darbo naujumas

- Laiko-erdvės kristalinė struktūra yra nauja aukšto dimensiškumo gardelė, sukuriama pasitelkiant erdvėje periodinio gaudyklės potencialo rezonansinį purtymą. Ši sistema papildo žinomų gardelių su sintetinėmis dimensijomis gretas [41, 42], pasiūlydama alternatyvų įgyvendinimo būdą ir suteikia įrankius nagrinėti topologinius efektus, tokius kaip lokalizuotų kraštinių būsenų susidarymą [62] ar Thouless pumpavimą daugiamatėje erdvėje [45].
- Dirbtinių neuroninių tinklų taikymas gardelių žemiausios energijos būsenos radimui yra nauja sritis [57, 63], kuri pasiūlo skaičiavimo metodą papildantį tipiška naudojamus tikslaus diagonalizavimo ir tenzorinių tinklų algoritmus. Analitinė analizė rodo, kad dirbtiniai neuroniniai tinklai gali tiksliai atvaizduoti daugiadalelines būsenas [64], tačiau yra išlikęs atviras optimizavimo klausimas – neaišku ar duotas tinklas sugebės tiksliai išmokti duoto modelio bruožus. Šiame darbe tiriamos dvi skirtingos tinklų architektūros, siekiančios tiksliai nustatyti arba pagerinti žemiausios energijos būsenos įvertį ribotos geometrijos gardelėse. Ypač daug dėmesio skiriama gardelėms su plokščiomis energijos juostomis. Fizikiniu požiūriu jos yra įdomios dėl dominuojančio sąveikų indėlio plokščiose juostose, o skaičiavimų atžvilgiu, šios gardelės iškelia pakankamai sudėtingą problemą dirbtiniams neuroniniams tinklams įveikti. Kadangi neuroniniai tinklai remiasi efektyviu banginės funkcijos kodavimu, juos sėkmingai pritaikius potencialiai atsivertų galimybės tirti didesnes sistemas negu įmanoma su kitais skaičiavimo metodais.

Ginamieji teiginiai

1. Rezonansiniu dažniu purtoma gardelė palaiko parametrų režimą, kuriame susidaro laiko-erdvės kristalinė struktūra – erdvinė gardelė su periodine laikine struktūra kiekviename erdvinės gardelės mazge.
2. Laiko-erdvės kristalinės struktūros leidžia tirti šešiamacių gardelių topologines savybes.

3. Atribotos Boltzmann architektūros neuroniniai tinklai sėkmingai koduoja plokščių energijos juostų gardelių modelių globalią banginės būsenos tikimybės tankio struktūrą, pasitelkdami energijos minimizavimą.
4. Dirbtiniai neuroniniai tinklai didelėse sistemose yra linkę užstrigti tikimybės tankio konfigūracijose atitinkančiose lokalius energijos minimumus.
5. Autoenkoderio taikymas triukšmingų duomenų analizei leidžia patikslinti žemiausios energijos būsenos įvertį, turint aibę apytikslių banginių būsenų superpozicijų su dominuojančiu žemiausios energijos būsenos indėliu.

Laiko-erdvės kristalinės struktūros

Įprastas kristalas yra periodinis atomų išsidėstymas, kurio struktūrą nulemia tarpdalelinės sąveikos. Tokį kristalą galima aprašyti kaip stabilią kvantinę būseną, susidarancią po spontaninio banginių būsenų tolydinės transliacinės simetrijos sulaužymo dėka išorinių trikdžių, pvz. sąveikos su aplinka ar atlikto matavimo. Kristalo būseną yra simetrinė gardelės konstantos kartotinio postūmio atžvilgiu, tuo tarpu hamiltonianas, aprašantis sistemą, turi aukštesnę, tolydinę transliacijos simetriją, kuria taip pat pasižymi sistemos tikrinės būsenos. Laiko kristalą [24, 25, 131–133] galima įsivaizduoti analogiškai, tereikia sukeisti erdvės ir laiko vaidmenis. Šiuo atveju spontaniškai sulaužoma arba diskreti, arba tolydinė laiko transliacinė simetrija, todėl sistema pasižymi laikiniu periodiškumu, aprašomu bazine būseną, kurios simetrija yra žemesnė negu sistemos hamiltoniano. Termodinaminėje pusiausvyroje iškyla fundamentalių laiko kristalų sukūrimo apribojimų [132, 134], tačiau periodiškai purtomos daugiadalelės sistemos leidžia įgyvendinti laiko kristalus tiek teoriškai [135–138], tiek ir eksperimentiškai [139–144]. Gerai žinomas diskretaus laiko kristalo pavyzdys yra šaltųjų atomų Bose Einstein kondensatas, šokinėjantis ant rezonansiškai virpinamo veidrodžio [135], kai virpinimo dažnis yra natūralios atomų osciliacijos kartotinis. Tuomet šokinėjančių dalelių periodas sulaužytos simetrijos būsenoje tampa didesnis už virpinimo periodą.

Spontaninis simetrijos sulaužymas yra ne vienintelis būdas sukurti periodišką struktūrą laike. Panašiai kaip optinės gardelės sugaunančios daleles šviesos sudarytame periodiniame potenciale, taip ir tinkamai parinktas rezonansinis sistemos purtymas gali sukurti efektinį potencialą išrikiuojantį daleles periodiškai laike [24, 25, 133, 145]. Šios sukonstruotos laiko kristalinės struktūros suteikia galimybes tirti kondensuotų medžiagų reiškinius laiko dimensijoje – teoriškai yra numatyta Anderson lokalizacija [146–149], Mott izoliatoriaus fazė [150], topologiškai apsaugotos būsenos [151, 152] ir plokščių energijos juostų gardelių sukūrimas [153].

Sekančiuose skyreliuose pristatysime laiko-erdvės kristalines struktūras, kurios yra periodiškos laike ir erdvėje. Pasinaudodami laiko kristalinių struktūrų idėjomis, sukonstruosime naujo tipo aukšto dimensiskumo gardelę, kurioje laikas elgiasi kaip sintetinė dimensija susieta su kiekvienu erdviniu laisvės laipsniu. Pagrindiniai šių skyrelių rezultatai publikuoti [A1]. Pirmiausia sudarysime laikines struktūras kiekvienoje erdvinės gardelės potencinėje duobėje (mazge) parinkę atitinkamą gardelės purtymą. Taip efektyviai suformuosime dvimatę sistemą, susidedančią iš erdvėje ir laike pasikartojančių gardelės mazgų. Toliau parodysime, kad pridėdant papildomus du tarpusavyje ortogonalius erdvinius periodiškai purtomus potencialus galima padidinti sistemos išmatavimų skaičių iki šešių dimensijų. Daugiamatė sistema susiformuoja, nes su kiekviena erdvine kryptimi yra susieta laikinė dimensija. Iš to seka, kad

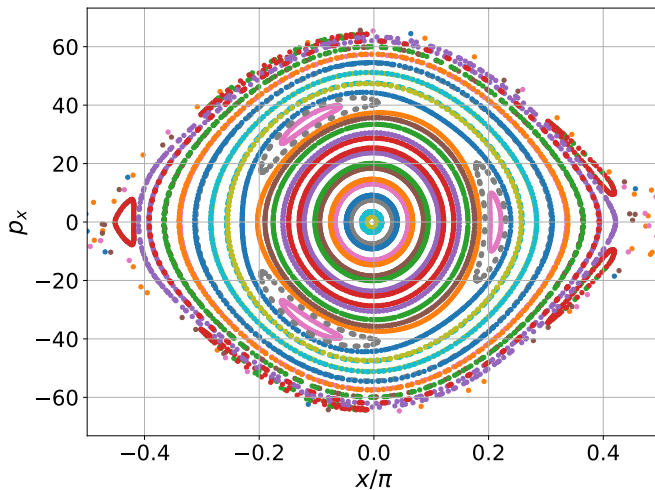
purtoama trimatė erdvinė gardelė sudaro šešiamatę laiko-erdvės kristalinę struktūrą. Galiausiai įvesime dirbtinius kalibruotės laukus, kurie leis tirti kvantinį Hall efektą ir topologines savybes aukštų dimensijų sistemose.

Laikinė kristalinė struktūra

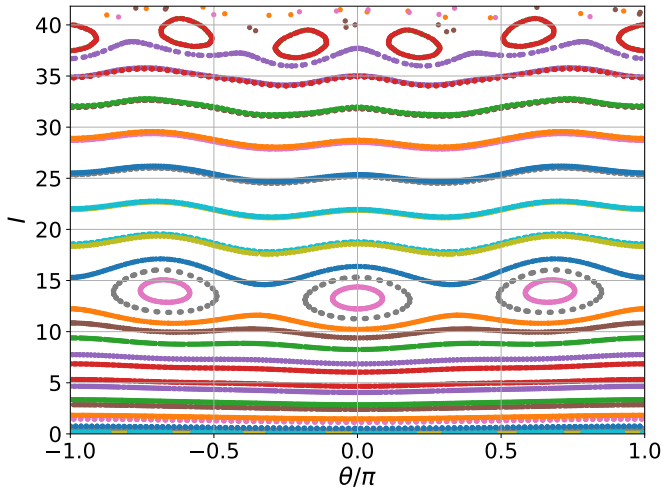
Laiko-erdvės kristalinės struktūros konstravimą pradėsime nuo laikinės struktūros, atsirandančios viename iš periodiškai purtomos erdvinės gardelės minimumų, tyrimo. Mūsų nagrinėjamą vienmatę sistemą aprašo klasikinis hamiltonianas

$$H(x, p_x, t) = \frac{p_x^2}{2m} + V_0 \sin^2(k_L [x - \lambda \cos(\omega t)]), \quad (1)$$

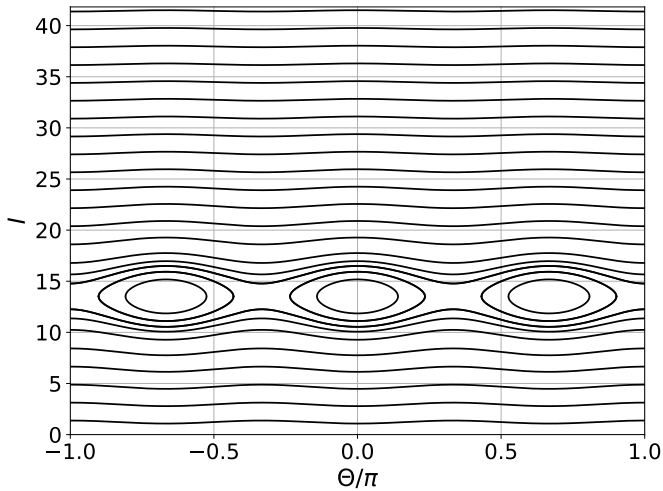
kai m yra dalelės masė, x – koordinatė, p_x – judesio kiekis, V_0 – gardelės potencialo amplitudė, k_L – banginis vektorius, aprašantis gardelės periodiškumą, ω – purtymo dažnis ir λ – maksimali gardelės nuokrypio amplitudė x kryptimi, dėl periodinio purtymo. Jei nesutrikdytame potenciale pagautos dalelės judėjimo dažnis Ω sutampa su sistemos virpinimo dažniu, arba sudaro jo kartotinį, t.y. $\omega = s\Omega$, kai $s \in \mathbb{Z}$, tuomet kiekviename gardelės minimume stebimas stroboskopinis fazinis portretas pasižymi diskrečia struktūra (1 pav.). Susidaro rezonansinės salos – uždaros trajektorijos neapimančios koordinatinių pradžių taško: $s = 3$ atveju 1 pav. matomos trys pilkos salos, o $s = 5$ – penkios raudonos salos fazinės erdvės kraštuose. Šios salos yra periodinės laikinės struktūros pagrindas – dalelės ties pasirinkta rezonansine trajektorija kiekvienoje iš salų vidutiniškai praleidžia vieną virpinimo periodą $T = 2\pi\omega$, kas sukuria diskretų ir lokalizuotą sistemos elgesį.



1 pav. Tipinis periodiškai purtomos vienmatės gardelės stroboskopinis fazinis portretas su charakteringomis rezonansinėmis salomis.



2 pav. Stroboskopinis fazinis portretas veikimo-kampo koordinatinių sistemoje su tais pačiais parametrais kaip ir 1 pav.



3 pav. Efektinio hamiltoniano (2) judėjimo lygčių sprendiniai su 2 pav. naudotais parametrais.

Norint gauti efektinę sistemos aprašymą ties rezonansinėmis salomis, patogiu atlikti kanoninę transformaciją, leidžiančią atvaizduoti fazinį portretą veikimo I ir kampo θ koordinatinių sistemoje [154]. Tuomet 1 pav. naujoje koordinatinių sistemoje atrodys kaip pavaizduota 2 pav. Šis atvaizdavimas leidžia lengvai nustatyti veikimo I_s vertę, ties kuria formuojasi s -tojo rezonanso salos. Taikant sekuliarią aproksimaciją, suvidurkinančią hamiltonianą per laiką, atmetami sparčiai osciluojantys nariai. Tuomet galime užrašyti efektinį hamiltonianą

besisukančioje koordinačių sistemoje $\Theta = \theta - \frac{\omega t}{s}$ nusakantį sistemos elgesį ties s -tuoju rezonansu [155]:

$$H_{\text{eff}}(\Theta, I) = \frac{P^2}{2m_{\text{eff}}} - V_{\text{eff}} \cos(s\Theta) + \text{const.} \quad (2)$$

Čia $m_{\text{eff}} = \left(\frac{\partial^2 H_0(I)}{\partial I^2} \Big|_{I_s} \right)^{-1}$ yra efektinė masė, nustatoma iš nepurtomo hamiltoniano $H_0(I)$, o $V_{\text{eff}} = \lambda\omega |p_s(I)|$ yra efektinis potencialas, kai p_s – s -toji judesio kiekio Fourier komponentė. Taip pat apibrėžiamas efektinis judesio kiekis $P \equiv I - I_s$. Norint įsitikinti, kad šis hamiltonianas gerai aproksimuoja purtomos sistemos elgesį, išsprendžiame judėjimo lygtis aplink $s = 3$ rezonansą ir matome, kad sprendiniai (3 pav.) gerai įvertina rezonansinių salų dydį pavaizduotą 2 pav. Efektinio hamiltoniano (2) forma atitinka tipinį kietojo kūno kristalo aprašymą pagautam elektronui. Naudodamiesi šia analogija sakome, kad ties kiekvienu erdviu gardelės minimumu egzistuoja periodinė sistema aprašoma (2) hamiltonianu, kurią vadinsime laikine struktūra.

Analizuojant šią sistemą klasikiniame režime mes pamatėme, kad purtant vienmatę gardelę rezonansiniu dažniu galime lokaliai sukurti efektyvias periodines struktūras kiekviename gardelės mazge. Norint kiekvieną struktūrą sukabinti su gretimuose gardelės mazguose esančiomis struktūromis ir pagaminti laiko-erdvės kristalinę gardelę, tenka naudoti kvantinį aprašymą, kuris leidžia įskaityti tuneliavimą tarp skirtingų mazgų.

Laiko-erdvės kristalinių struktūrų kvantinis aprašymas

Kvantinę problemos analizę pradėsime nuo kanoniškai kvantuoto (1) hamiltoniano:

$$\hat{H}(t) = \frac{\hat{p}_x^2}{2m} + V_0 \sin^2(k_L [\hat{x} - \lambda \cos(\omega t)]). \quad (3)$$

Perėjus į virpinamą atskaitos sistemą ir perrašius hamiltonianą atatranks energijos vienetais $E_R = \frac{\hbar^2 k_L^2}{2m}$ gauname

$$\hat{H}(t) = \hat{p}_x^2 + V_0 \sin^2(\hat{x}) + \lambda\omega \sin(\omega t)\hat{p}_x. \quad (4)$$

Šis hamiltonianas yra periodinis laike, todėl patogu taikyti Floquet formalizmą. Ieškosime Floquet hamiltoniano $\hat{\mathcal{H}}(t) = \hat{H}(t) - i\frac{\partial}{\partial t}$ tikrinių verčių problemas

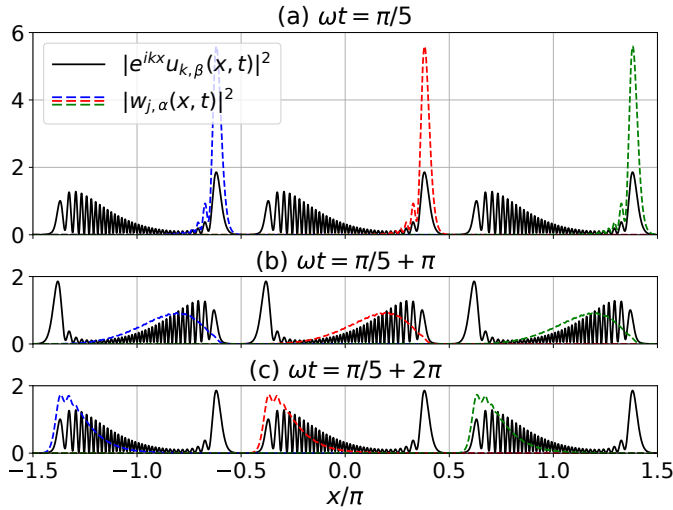
$$\hat{\mathcal{H}}(t)\Phi_{k,\alpha}(x, t) = E_{k,\alpha}\Phi_{k,\alpha}(x, t), \quad (5)$$

sprendinių, kurie yra Bloch funkcijos formos $\Phi_{k,\alpha}(x, t) = e^{ikx}u_{k,\alpha}(x, t)$. Funkcija $u_{k,\alpha}(x, t) = u_{k,\alpha}(x + \pi, t) = u_{k,\alpha}(x, t + \frac{2\pi}{\omega})$ yra periodinė tiek erdvėje, tiek laike. Kvazienergija $E_{k,\alpha}$ priklauso nuo kvazijudėsio kiekio k ir ją indeksuoja kvantinis skaičius α .

Skaitmeninis problemos sprendimas leidžia rasti Floquet funkcijų $\Phi_{k,\beta}(x, t)$ sprendinius s -tojo rezonanso aplinkoje. Vieno iš šių sprendinių tikimybės tankis pavaizduotas 4 pav. juoda linija skirtingais laiko momentais, trijuose periodinio erdvinio potencialo mazguose. Matome, kad po vieno virpinimo periodo ši funkcija sugrįžta į pradinę padėtį, t.y. išlaiko hamiltoniano periodiškumą. Iš šių rezonansinių Floquet būsenų galima sudaryti lokalizuotas Wannier būsenas, skaitmeniškai diagonalizuojant pozicijos operatorių rezonansinių būsenų bazėje [76]. Gautas Wannier funkcijas galime užrašyti kaip

$$w_{j,\alpha}(x, t) = \sum_{k,\beta} b_{k,\beta}^{j,\alpha} \Phi_{k,\beta}(x, t), \quad (6)$$

kai k sumuojamas per visus leidžiamus kvazijudėsio kiekius, o $\beta = 1, \dots, s$ per visas rezonansines būsenas. $b_{k,\beta}^{j,\alpha}$ – skaitmeniškai nustatyti koeficientai. Kiekviena iš Wannier būsenų yra lokalizuota tam tikrame j -ajame erdviniam gardelės mazge ir laikiniame mazge α . Laikinį mazgą atitinka vienas iš laikinio potencialo minimumų ties rezonansine sala. Pažvelgę į trijų Wannier funkcijų, pažymėtų skirtingomis spalvomis, evoliuciją trijuose gardelės mazguose 4 pav., matome, kad per purtymo periodą T funkcijos nesugrįžta į pradinę padėtį – jų periodiškumas sT yra būdingas s mazgų laikinei struktūrai.



4 pav. Vienos iš rezonansinių Floquet būsenų tikimybės tankio (juoda kreivė) ir Wannier būsenų tikimybės tankio (spalvotos brūkšninės linijos) priklausomybė nuo erdvinės koordinatės trijuose mazguose. Funkcijos pavaizduotos trimis laiko momentais, atitinkančiais fazes: (a) $\omega t = \pi/5$, (b) $\omega t = \pi/5 + \pi$ ir (c) $\omega t = \pi/5 + 2\pi$.

Wannier funkcijų lokalumas leidžia jas panaudoti kaip bazę stipraus ryšio artinio hamiltonianui užrašyti, t.y. apibrėžti efektyvų modelį, aprašantį laiko-

erdvės kristalinę struktūrą kaip gardelę:

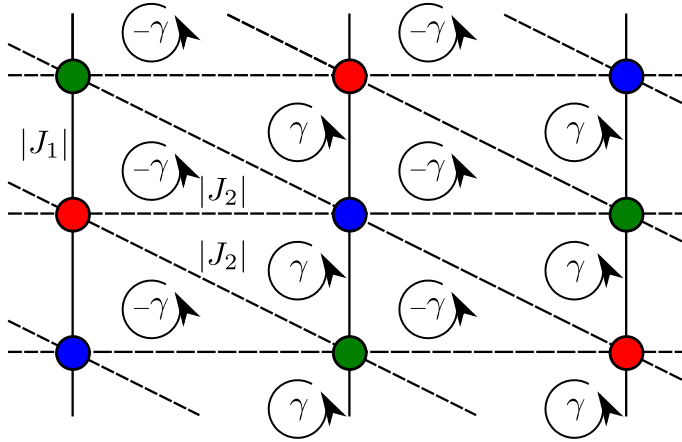
$$\hat{H}_{\text{TB}} = -\frac{1}{2} \sum_{j',\alpha',j,\alpha} J_{j,\alpha}^{j',\alpha'} \hat{a}_{j',\alpha'}^\dagger \hat{a}_{j,\alpha}, \quad (7)$$

kai operatorius $\hat{a}_{j,\alpha}^{(\dagger)}$ sunaikina (sukuria) dalelę j -ajame erdviniame mazge ir α -jame laikiniame mazge. Tuneliavimo stipris $J_{j,\alpha}^{j',\alpha'}$ aprašo kompleksines šuolio amplitudes iš mazgo (j, α) į (j', α') :

$$J_{j,\alpha}^{j',\alpha'} = -\frac{2}{sT} \int_0^{sT} dt \int_{-\frac{\pi}{2}L}^{\frac{\pi}{2}L} w_{j',\alpha'}^*(x,t) \hat{\mathcal{H}}(t) w_{j,\alpha}(x,t) dx, \quad (8)$$

čia L – gardelę sudarančių erdvinių mazgų skaičius.

Viena iš tokių gardelių realizacijų yra pavaizduota 5 pav. Išilgai horizontalios ašies turime išsidėsčiusius L erdvinius gardelės mazgus, o išilgai vertikalios ašies yra pasiskirstę s laikiniai mazgai. Šuolių matrica sudaryta iš $J_{j,\alpha}^{j',\alpha'}$ elementų apibrėžia galimus tuneliavimus, kurie yra pavaizduoti skirtingomis mazgus jungiančiomis linijomis ir pilnai nusako gardelės geometriją. Esant kompleksiniams šuoliams taip pat gali atsirasti ir uždarus gardelės kontūrus (plaketes) kertantys dirbtiniai magnetiniai srautai γ . Modifikuojant purtymo ir potencialo parametrus, gardelės geometrija ir srautai gali keistis iš esmės, todėl norint tiksliau reguliuoti srautus reikia įvesti papildomą potencialo moduliavimą.



5 pav. Kvazivienmatė laiko-erdvės kristalinė struktūra, kai $V_0 = 4320$, $s = 3$, $\omega = 240$ ir $\lambda = 0.01$. Horizontali ašis atitinka erdvės dimensiją, o vertikali – laikinę. Tos pačios spalvos mazgai žymi vienodos fazės Wannier funkcijas prieš laikinį vidurkinimą. $|J_1|$ ir $|J_2|$ yra šuolių parametrų vertės tarp mazgų atitinkamai sujungtų vientisa ir brūkšniuota linija. γ yra dirbtinis magnetinis srautas kertantis gardelės plakečių plotus.

Aukščiau nagrinėtą laiko-erdvės struktūrą nesunku generalizuoti aukštesnėms dimensijoms. Prie turimos purtomos vienmatės gardelės aprašomos hamiltonianu (4) galime pridėti dvi papildomas virpinamas vienmates gardeles nukreiptas ortogonaliomis kryptimis, taip sukuriant trimatį erdvinį kristalą. Kadangi kiekviena vienmatė gardelė palaiko periodinį laikinį potencialą, tokiam kristale galime įgyvendinti šešiamatę laiko-erdvės kristalinę struktūrą. Ją apibrėžia hamiltonianas

$$\hat{H}^{3D}(t) = \hat{H}_x(t) + \hat{H}_y(t) + \hat{H}_z(t), \quad (9)$$

kai $\hat{H}_q(t)$, $q \in \{x, y, z\}$ yra hamiltonianas (4), aprašantis sistemą q ašies kryptimi. Šis trimatis hamiltonianas yra atskiriamas, todėl galime rasti Wannier funkcijas $w_{j_q, \alpha_q}(q, t)$ kiekvienai ašiai atskirai. Tuomet bendras erdvėje trimačio kristalo sprendinys yra šių Wannier funkcijų sandauga:

$$W_{\vec{j}, \vec{\alpha}}(\vec{r}, t) = w_{j_x, \alpha_x}(x, t) w_{j_y, \alpha_y}(y, t) w_{j_z, \alpha_z}(z, t). \quad (10)$$

Vektoriniai dydžiai apibrėžti kaip $\vec{r} = (x, y, z)$, $\vec{j} = (j_x, j_y, j_z)$ ir $\vec{\alpha} = (\alpha_x, \alpha_y, \alpha_z)$. Erdviniai mazgai yra indeksuojami vektoriumi \vec{j} , o laikiniai – $\vec{\alpha}$ su komponentėmis $a_q \in \{1, \dots, s\}$, kai s yra rezonanso, ties kuriuo purtoma sistema, skaičius. Pasinaudojant šiomis Wannier funkcijomis galime sudaryti laiko-erdvės kristalinę struktūrą aprašomą stipraus ryšio modeliu

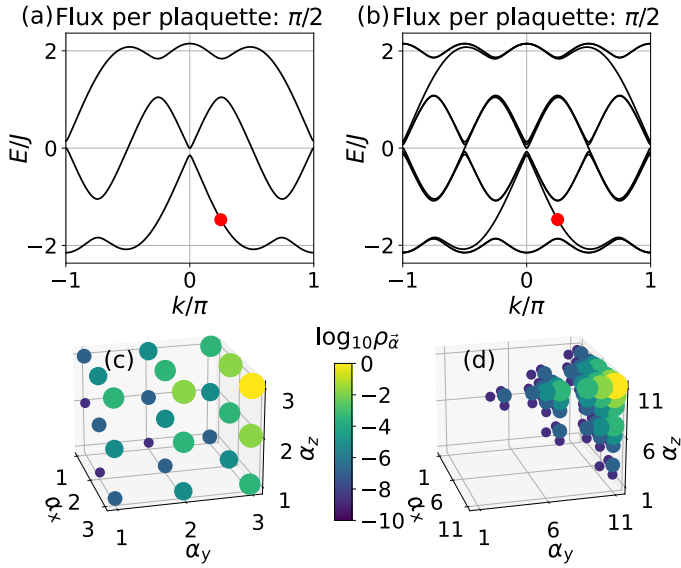
$$\hat{H}_{TB} = -\frac{1}{2} \sum_{\vec{j}', \vec{\alpha}', \vec{j}, \vec{\alpha}} J_{\vec{j}, \vec{\alpha}}^{\vec{j}', \vec{\alpha}'} \hat{a}_{\vec{j}', \vec{\alpha}'}^\dagger \hat{a}_{\vec{j}, \vec{\alpha}}, \quad (11)$$

su šuolio parametrais

$$J_{\vec{j}, \vec{\alpha}}^{\vec{j}', \vec{\alpha}'} = -\frac{2}{sT} \int_0^{sT} dt \int dx \int dy \int dz W_{\vec{j}', \vec{\alpha}'}^*(\vec{r}, t) \left(\hat{H}^{3D}(t) - i \frac{\partial}{\partial t} \right) W_{\vec{j}, \vec{\alpha}}(\vec{r}, t). \quad (12)$$

Matome, kad kiekvienas mazgas indeksuojamas šešiais indeksais, taigi gauta gardelė yra šešiamatė. Toks pats išvedimas galioja sistemai sudarytai iš poros lazerių – tuomet gauta struktūra bus keturmatė. Šios daugiamatės struktūros gali būti alternatyva sistemoms su sintetinėmis dimensijomis [41, 42], kurios išnaudoja vidinę dalelių sandarą aukštesnėms dimensijoms pasiekti.

Laiko-erdvės kristalinės struktūros yra taip pat tinkamos topologinėms medžiagų savybių tyrimams aukštesnėse dimensijose. Kontroluojamų dirbtinių kalibruotės laukų sukūrimui galima pasitelkti metodus žinomus optinių gardelių fizikoje [35, 159] – išderinus laikinių mazgų energiją periodiškai moduluotu potencialu sustabdomi natūralūs šuoliai laikine kryptimi, tuomet panaudojant papildomus lazerius atstatomas tuneliavimas, tačiau su valdoma, lazerių sąlygota faze. Tinkamai parinkus šių lazerių kryptis, įmanoma sukurti bet kokią efektyvią magnetinį srautą kertantį daugiamatės gardelės plaketes.



6 pav. Viršutinė eilutė: Vienos 2D kvadratinės laiko-erdvės struktūros sudarančios 6D gardelę energijos dispersijos sąryšis, kai mazgų skaičius laikine kryptimi yra (a) $s = 3$ ir (b) $s = 11$. Gardelės plaketės kerta dirbtinis magnetinis srautas $\frac{\pi}{2}$. Raudoni taškai žymi pasirinktą kraštinę būseną, kurios tikimybės tankio projekcijos $\rho_{\vec{\alpha}}$ į laikinę dimensiją pavaizduotos (c) ir (d) po atitinkamomis dispersijomis.

Vienas iš topologinių efektų, kurių įmanoma realizuoti šešiamatėje laiko-erdvės struktūroje, yra topologinės kraštinės būsenos. Tai yra būsenos, kurios lokalizuojasi ties atvirais gardelės kraštais ir apibūdinamos netrivialiu topologiniu invariantu [45]. Tarkim turima kubinė gardelė yra periodinė visomis erdvinėmis kryptimis, o kiekviena su erdvine 1D gardele susieta laikinė kryptis turi baigtinį skaičių s mazgų. Jei gardelės kvadratinės laiko-erdvės plaketės kerta magnetinis srautas $\gamma = \frac{\pi}{2}$, energijos dispersijoje atsiranda charakteringos linijos atitinkančios kraštinių būsenų energiją ir jungiančios energijos juostas per draustinį tarpą (6 pav. (a), kai $s = 3$, (b) – $s = 11$). Apibrėžus tikimybės tankį kraštinėje būsenoje $|\psi\rangle$ ties mazgu $(\vec{j}, \vec{\alpha})$ kaip $\rho_{\vec{j}, \vec{\alpha}} = \langle \psi | \hat{a}_{\vec{j}, \vec{\alpha}}^\dagger \hat{a}_{\vec{j}, \vec{\alpha}} | \psi \rangle$, galime suskaičiuoti tankio projekciją $\rho_{\vec{\alpha}} = \sum_{\vec{j}} \rho_{\vec{j}, \vec{\alpha}}$. Ši projekcija nusako kokį tankio indelį sudaro kiekvienas laikinis mazgas $\vec{\alpha}$ susumavus per visus to mazgo erdvininius indeksus \vec{j} . Pasirinkę kraštinę būseną ties kvaziimpulsu $k_x = k_y = k_z = \frac{\pi}{4}$ pažymėtą dispersijos sąryšiuose raudonu tašku, matome, kad tankio projekcijos $\rho_{\vec{\alpha}}$ pavaizduotos 6 pav. (c, d) lokalizuojasi kampiniuose taškuose. Tai reiškia, kad būseną yra lokalizuota visų 2D laiko-erdvės struktūrų (iš kurių sudaryta 6D struktūra) viename iš laikinių kraštų.

Apibendrinant, startavę nuo klasikinės virpinamos gardelės pamatėme, kad

purtant sistemą rezonansiniu dažniu išryškėja papildoma periodinė struktūra kiekvienoje gardelės potencinėje duobėje. Ši struktūra gali būti išnaudojama kaip sintetinė dimensija, kurią vadiname laikine arba laiko dimensija. Kvantinis šios sistemos tyrimas leido aprašyti purtomą vienmatę gardelę kaip efektingą dvimatę laiko-erdvės struktūrą ir įvertinti tokių sistemų geometriją iš leistinų tuneliavimo parametrų tarp mazgų. Kadangi kiekviena 1D erdvinė purtoma gardelė palaiko laikinę struktūrą, pasitelkiant du arba tris lazerius galima įgyvendinti 4D arba atitinkamai 6D laiko-erdvės kristalines struktūras. Turėdami šių struktūrų aprašymą, į sistemas įvedėme kontroliuojamus efektinius magnetinius srautus, leidžiančius kurti topologines savybes svarbias kvantinių kompiuterių veikimui. Taigi laiko-erdvės kristalinės struktūros yra universalios daugiamatės gardelės, kurios atveria kelią tirti ir tobulinti elektroniką aukštesnėse dimensijose.

Dirbtinių neuroninių tinklų taikymas žemiausiai energijos būsenai nustatyti

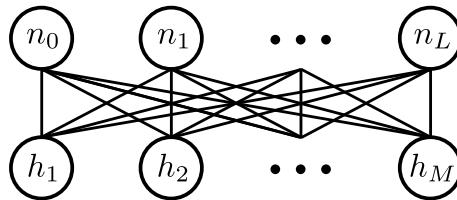
Optinėse gardelėse pagautų šaltųjų atomų dujų daugiadalelinių procesų skaitmeninis modeliavimas yra sudėtingas, daug kompiuterinių resursų reikalaujantis uždavinys. Dabartiniai skaitmeniniai metodai, priklausomai nuo uždavinio specifikos, geba surasti gardelių, susidedančių iš dešimčių/šimtų mazgų žemiausios energijos būsenas [52]. Norint pasiekti didesnį tikslumą ir spręsti problemas, susidedančias iš daugiau dalelių, plėtojami seni bei kuriami nauji algoritmai veikiantys žemų energijų poerdvyje [160]. Mašininis mokymasis yra jau ilgą laiką taikomas didelių duomenų apdorojimui – kalbos analizei, klasifikavimo problemos ir vaizdų atpažinimui [161, 162]. Pastaruoju metu šis metodas sulaukia vis daugiau sėkmės ir kondensuotų medžiagų fizikoje. Jis pradėtas taikyti medžiagų fazėms atpažinti [163, 164], ekstrapoliuoti informaciją apie fazinius virsmus [165], klasifikuoti eksperimentinius duomenis [166, 167] ir atlikti kvantinę tomografiją [168]. Ypač aktualus taikymas kvantinių problemų skaičiavimų sričiai yra galimybė atvaizduoti banginę būseną kaip neuroninį tinklą [57, 60]. Neuroninis tinklas gali užkoduoti žemiausios energijos būsenas, kurios yra labai susietos [64, 169] bei pritaikyti šį kodavimą stipriai koreliuotos kvantinės medžiagos skaičiavimams su tikslumu prilygstančiu arba net geresniu negu įprastai naudojamų algoritmų [170–176].

Mūsų tikslas yra pritaikyti dirbtiniais neuroniniais tinklais koduojamų būsenų formalizmą plokščių energijos juostų gardelėms ir ištirti rezultatų tikslumą, taip pat išnagrinėti galimybę išgauti žemiausios energijos banginę būseną iš triukšmingų banginių būsenų imties, kurios būsenos yra artimos tiksliam rezultatui. Šiems tikslams įgyvendinti mes pasitelksime dviejų tipų dirbtinius neuroninius tinklus – apribotą Boltzmann mašiną ir tiesioginio sklidimo

autoenkoderį. Apribota Boltzmann mašina bus taikoma gardelių žemiausios energijos būsenos nustatymui ir jos tikimybių tankio struktūros tyrimui, pasitelkiant neuroninio tinklo koeficientų optimizavimą minimizuojant sistemos energiją. Sekant [A2], ypatingas dėmesys bus skirtas dviems gardelių geometrijoms palaikančioms kompaktiškas lokalias būsenas – kvazivienmatedi trikampaui gardelei ir dvimatei kagome gardelei. Tuo tarpu autoenkoderis bus taikomas kaip antrinės analizės įrankis, kaip įvestį priimantis apytiksles žemiausios energijos būsenos išraiškas, gautas kitais skaičiavimo metodais, ir bandantis sugeneruoti geresnę įvestį. Šio tinklo galimybės bus tiriamos bandant išgauti kvadratinės ir kvazivienmatės trikampės gardelių tikimybių tankius iš pradinės triukšmingų būsenų aibės pagal [A3].

Apribota Boltzmann mašina

Dirbtinio neuroninio tinklo architektūros pasirinkimas priklauso nuo sprendžiamos problemos. Labiausiai paplitusios architektūros skirtos žemiausių kvantinės sistemos būsenų radimui yra apribota Boltzmann mašina [57–59] ir tiesioginio sklidimo neuroniniai tinklai [60]. Taip pat taikomi konvoliuciniai neuroniniai tinklai [61, 171]. Motyvuoti apribotų Boltzmann mašinų sėkme nustatant žemiausią sistemos energiją, mes pasirenkame šią architektūrą žemiausių energijos būsenų struktūrų tyrimui.



7 pav. Apribota Boltzmann mašina. Kiekvienas iš $L + 1$ įvesties mazgų n_ℓ yra sujungtas su M paslėptų mazgų h_j tiesiomis linijomis, kurios atvaizduoja svorinius koeficientus $W_{\ell j}$.

Apribota Boltzmann mašina atvaizduoja banginę būseną kaip dviejų sluoksnių neuroninį tinklą. Jis yra visiškai sujungtas – kiekvienas vieno sluoksnio mazgas yra sujungtas su visais kito sluoksnio mazgais. Ši struktūra schematiškai pavaizduota 7 pav. Mazgai pažymėti n_ℓ priklauso taip vadinamam matomam sluoksniui ir žymi įvesties koeficientus, o h_j yra paslėpti mazgai, kurie gali įgyti vertes $\{-1, 1\}$. Sąryšį tarp matomų ir paslėptų mazgų aprašo svoriai $W_{\ell j}$. Pagrindinė prielaida apie žemiausios energijos būsenos koeficientus $\psi(\gamma)$ yra gaunama susumavus neuroninį tinklą aprašančius Boltzmann faktorius per visas įmanomas paslėptų mazgų vertes [57]. Šie koeficientai nusako, kokį svorį turi bazinis vektorius atitinkantis $\gamma = (n_0, n_1, \dots, n_L)$ konfigūraciją

žemiausios energijos būsenoje:

$$\psi(\gamma) = e^{\sum_{\ell=0}^L a_{\ell} n_{\ell}} \prod_{j=1}^M 2 \cosh \left(\sum_{\ell=0}^L W_{\ell j} n_{\ell} + b_j \right), \quad (13)$$

kai a_{ℓ} yra matomo sluoksnio koeficientų pataisa ir b_{ℓ} – paslėpto sluoksnio koeficiento pataisa. Neuroninio tinklo koeficientų aibė $\vec{w} = \{W_{\ell j}, a_{\ell}, b_j\}$ visiems $j = 1, 2, \dots, M$ ir $\ell = 0, 1, \dots, L$ pilnai nusako sistemą. Norint rasti jų vertes neuroninis tinklas turi būti apmokomas. Mokymo procedūra susideda iš dviejų žingsnių – variacinis Monte Carlo metodas atsitiktinai atrenka bazinius vektorius iš konfigūracijų erdvės ir įvertina sistemos vidutinę energiją [193]. Gauta energija minimizuojama atnaujinant neuroninio tinklo koeficientus pasitelkiant optimizavimo metodus [180]. Mokymosi protokolas gali būti susumuotas kaip kelių žingsnių seka:

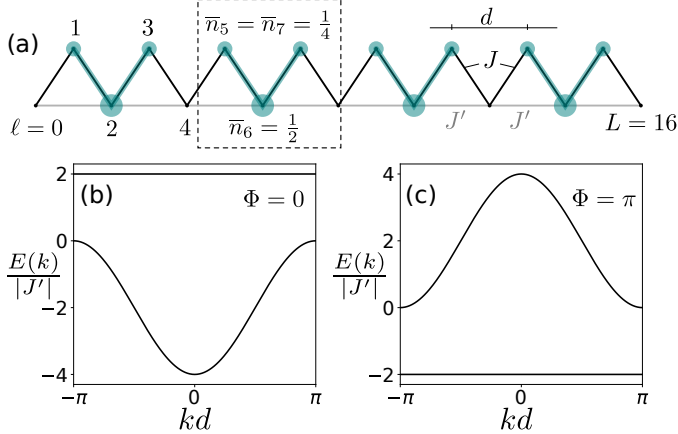
1. Atribota Boltzmann mašina inicijuojama su atsitiktiniais mažais svoriniais koeficientais \vec{w} ir pasirenkama atsitiktinė sistemos konfigūracija γ .
2. Atliekami N_{MC} Monte Carlo algoritmo žingsniai atrenkantys konfigūracijų rinkinį ir įvertinama sistemos energija esant pradiniam tinklo svoriniams koeficientams.
3. Tinklo koeficientai atnaujinami pasitelkiant Adam/AdaMax metodą [180], kuris minimizuoja energiją.
4. Procesas kartojamas nuo 2 punkto baigtinį N_{update} atnaujinimų skaičių arba kol pasiekiamas norimas stebimo dydžio tikslumas.

Apmokytas neuroninis tinklas gali įvertinti bet kokio operatoriaus \hat{A} tikėtinausią vertę $\langle \hat{A} \rangle = \left\langle \frac{\langle \gamma | \hat{A} | \psi \rangle}{\langle \gamma | \psi \rangle} \right\rangle_{\gamma}$ imant statistinį vidurkį per Monte Carlo metodu sugeneruotas γ konfigūracijas [193].

Plokčių energijos juostų gardelių savybių tyrimas taikant atribotą Boltzmann mašiną

Gardelės su plokščiomis energijos juostomis pasižymi įdomiais dalelių sąveikos nulemtais reiškiniiais – trupmeniniu kvantiniu Hall efektu [100, 181, 182], superlaidininkų būsenų koreliavimu [183, 184], plokščių juostų magnetizmu sukintose sistemose [185] ir kitais, žiūrėti [71]. Mes nagrinėsime žemiausios energijos būsenas, kurios gali būti išreikštos per kompaktiškas lokalias tikrines būsenas [186, 187], susietas su gardelės žemiausia plokščia energijos juosta. Šios būsenos yra Bloch bangų superpozicijos ir lokalizuojasi ant keleto gardelės mazgų atskirtų nuo kitų lokalizuotų sričių per tuščius mazgus, kuriuose nėra dalelių dėl destruktivios kvantinės interferencijos. Dalelių tankio skirstiniai susiformavę iš kompaktiškų lokalizuotų būsenų sudaro pakankamai sudėtingas

struktūras, tinkamas tirti neuroninio tinklo gebėjimą išmokti su jomis susijusias savybes. Šiame skyrelyje taikysime apribotą Boltzmann mašiną kvazivienmatės trikampės ir dvimatės kagome geometrijos gardelėms su plokščiomis žemiausios energijos juostomis tyrimui ir įvertinsime kiek tiksliai neuroninis tinklas nustato sistemos parametrus.



8 pav. (a) Kvazivienmatė trikampė gardelė su $L+1 = 17$ mazgais, atskirtais per gardelės konstantą d . Šuolio parametrai J ir J' pažymėti atitinkamai juodomis ir pilkomis linijomis. Brūkšninės linijos apsupa antrąją tankio salą, kurioje lokalizuota viena dalelė su žaliai pažymėtais dalelių tankiais $\bar{n}_5 = \bar{n}_7 = \frac{1}{4}$ ir $\bar{n}_6 = \frac{1}{2}$ atitinkamuose mazguose. (b) Energijos dispersijos sąryšis, kai $J'/|J'| > 0$, šiuo atveju sužadinta energijos juosta yra plokščia ir srauto kertančio elementarų gardelės narvelį nėra ($\Phi = 0$). (c) Energijos dispersijos sąryšis, kai $J'/|J'| < 0$ – žemiausia energijos juosta yra plokščia ir dėl neigiamo šuolio parametro atsiranda elementarų gardelės narvelį kertantis srautas $\Phi \neq 0$.

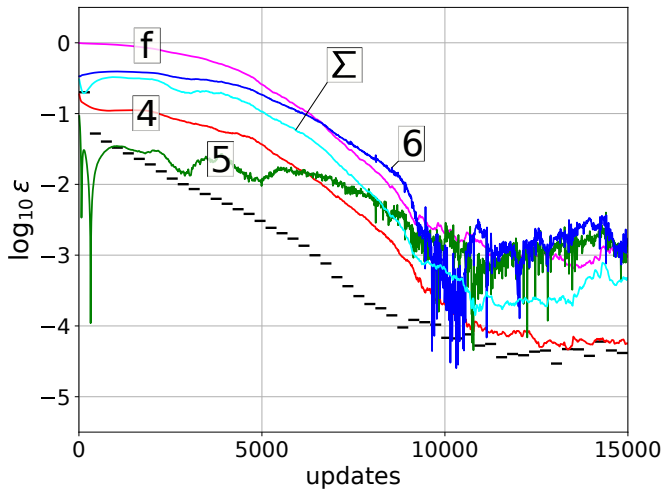
Viena iš paprasčiausių gardelių, turinčių plokščią energijos juostą yra kvazivienmatė trikampė gardelė (8 pav. (a)). Toks gardelės modelis gali būti įgyvendinamas tiek fotoniniuose kristaluose [190], tiek šaltųjų atomų sistemoje [191]. Mes pasirinksime parametrų režimą, kuriame tokioje gardelėje žemiausios energijos būsenoje matoma tankio banga sudaryta iš kompaktiškų lokalizuotų būsenų. Laikant, kad kvazivienmatė gardelė aprašoma stipraus ryšio artinio hamiltonianu

$$\hat{H} = \left(-J \sum_{\ell=1}^L \hat{a}_{\ell}^{\dagger} \hat{a}_{\ell-1} - J' \sum_{j=1}^{L/2} \hat{a}_{2j}^{\dagger} \hat{a}_{2j-2} + \text{h.c.} \right) + \frac{U}{2} \sum_{\ell=0}^L \hat{n}_{\ell} (\hat{n}_{\ell} - 1), \quad (14)$$

tarsim, jog sistemą sudaro $L+1 = 17$ mazgas ir 4 dalelės, sąveikaujančios $U/|J'| = 0.1$ stiprio sąveika išreikšta šuolio parametro vienetais. Gardelės kraštines sąlygas laikysime atviromis. Jei šuolio parametrai tarp artimiausių kaimynų tenkina sąryšį $J = \sqrt{2}|J'|$ ir $J'/|J'| = -1$, tuomet turėsime plokščią

energijos juostą su mažiausia energija (8 pav. (c)). Esminės žemiausios energijos būsenos savybės pavaizduotos 8 pav. (a). Dalelių tankiai išsidėsto į tankio bangą pavaizduotą žaliai. Viena dalelė pasiskirsto per tris mazgus, taip vadinamą tankio salą, pažymėtą punktyrinio stačiakampiu, atskirtą nuo kitų salų per tuščią mazgą. Kiekvienos salos centrinio mazgo užpilda yra $\frac{1}{2}$, o gretimų mazgų – $\frac{1}{4}$. Šie tankiai yra viena iš pagrindinių sistemos savybių, kurią neuroninis tinklas stengsis išmokti atpažinti.

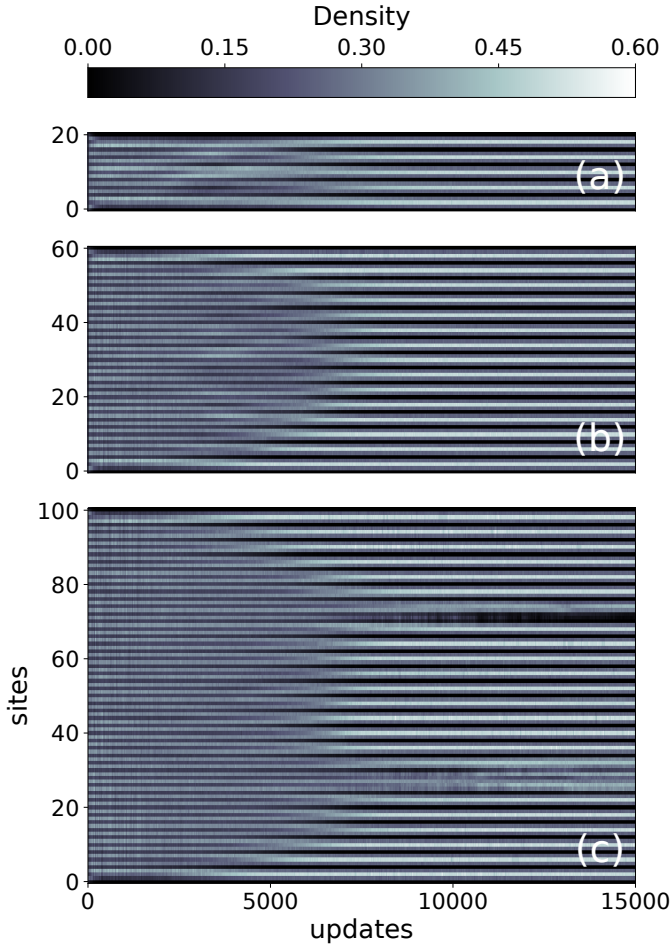
Skaičiavimams su apribota Boltzmann mašina atlikti taikysime Netket grupės neuroninio tinklo kodą [193]. Fizikinei sistemai apibūdinti naudosime parametrus iš praeito paragrafo. Laikysime, kad dirbtinio neuroninio tinklo paslėptų mazgų skaičius yra $M = \lfloor \alpha(L + 1) \rfloor$, kai paslėptų mazgų tankis $\alpha = 2.5$ ir $\lfloor \cdot \rfloor$ – funkcija grąžinanti didžiausią sveiką skaičių, kuris yra lygus arba mažesnis už įvestį. Atliksime $N_{\text{update}} = 15000$ neuroninio tinklo svorių \vec{w} optimizavimo operacijų pasitelkiant AdaMax algoritmą [180]. Prieš kiekvieną svorių atnaujinimą padaroma $N_{\text{MC}} = 5000$ Monte Carlo žingsnių, kurie išvaikšto konfigūracijų erdvę surinkdami būsenų sąrašą iš kurio gaunama suvidurkinta energija. Būtent toks gardelė dydžio ir paslėptų mazgų skaičiaus pasirinkimas yra motyvuotas tuo, kad šiuo atveju gardelės konfigūracijų skaičius viršija tinklo svorinių koeficientų skaičių. Tai reiškia, kad jei neuroninis tinklas išmoks banginę būseną, ji bus efektyviai užkoduota redukuota reprezentacija.



9 pav. Absoliučios paklaidos ε konvergavimas skirtingiems dydžiams, aprašantiems gardelę žemiausioje energijos būsenoje: žemiausios būsenos energijos E_{gs} paklaida (juodi brūkšniai), vidutinė užpildos paklaida 4 (raudona kreivė), 5 (žalia) ir 6 (mėlyna) mazge, nuokrypis nuo suminio tankio Σ antroje V formos saloje (žydra) ir tikslios bei suskaičiuotos žemiausios energijos būsenos persiklojimo f nuokrypis nuo vieneto (violetinė).

Pagrindiniai parametrai, kuriuos stebime mokymosi procese yra žemiausia sistemos energija E_{gs} , persiklojimas f tarp tikslios ir neuroninio tinklo numatomos žemiausios energijos būsenos, dalelių tankis trijuose skirtinguose gardelės mazguose: mazge besiribojančiame su tankio sala ir turinčiame tikslią tankio vertę $\bar{n}_4 = 0$, kraštiniame tankio salos mazge su tankiu $\bar{n}_5 = \frac{1}{4}$ ir centriniame salos mazge su iš analitinių skaičiavimų gauta tankio verte $\bar{n}_6 = \frac{1}{2}$. Taip pat žiūrėsime kiek suminis pasirinktos antrosios tankio salos tankis yra nutolęs nuo tikslios vertės $\bar{\Sigma} \equiv \bar{n}_5 + \bar{n}_6 + \bar{n}_7 = 1$. Visų šių dydžių absoliučių paklaidų nuo tikslų verčių dešimtainis logaritmas yra pavaizduotas 9 pav. po kiekvieno tinklo svorių atnaujinimo. Energija, žymima juodais brūkšneliais, sukongavus duoda tiksliausią rezultatą iš stebimų dydžių, su nuokrypiu tarp 10^{-5} ir 10^{-4} nuo tikslios vertės. Šis tikslumas yra palyginamas su rezultatais gautais nagrinėjant kitus kvantinius modelius pasitelkiant neuroninius tinklus [57, 60, 63]. Spartus kongavimas ir gautos energijos tikslumas nestebina, nes pats mokymosi procesas yra parentas energijos minimizavimu. Įdomiau pažiūrėti kaip elgiasi tankio struktūra. Galima išskirti dvi tankio struktūros charakteristikas – globalią ir lokalią. Globalią struktūrą apibrėžia neužimti gardelės mazgai, kurie atskiria tankio salas vieną nuo kitos. Vieno iš šių mazgų dalelių tankio nuokrypis nuo nulio pavaizduotas raudoną kreive, pažymėta mazgo numeriu „4“ 9 pav. ir matyti, kad šio įverčio tikslumas prilygsta energijos tikslumui. Kitų nulinio tankio mazgų rezultatai yra panašūs. Tai reiškia, jog neuroninis tinklas sugeba atpažinti tankio bangą sudarytą iš salų labai tiksliai. Tuo tarpu lokali struktūra nusako tankio pasiskirstymą individualioje saloje. Jeigu paimsime du konkrečius antrosios salos mazgus, pažymėtus numeriais „5“ ir „6“, atitinkančius užpildą kraštiniame ir centriniame salos mazge, pamatysime, kad jų nuokrypiai nuo tikslų verčių, neuroninio tinklo mokymo pabaigoje, yra apytiksliai eile didesni negu nustatytos globalios struktūros ir pasižymi santykiniai didelėmis fliktuacijomis aplink nuokrypį. Tai parodo, jog neuroninui tinklui yra sunku teisingai paskirstyti dalelių tankius vidinėje salos sandaroje. Vienos salos užpilda „ Σ “ ir tikslios bei rastos žemiausios energijos būsenų persiklojimas „ f “ patvirtina anksčiau padarytas išvadas. Persiklojimas konguoja panašiu tikslumu kaip lokalią struktūrą nulemiantys dydžiai, nes pagrindiniai nuokrypiai atsiranda dėl netikslaus tankio pasiskirstymo individualiose salose. Vienos salos užpilda konguoja tiksliau, nei lokali struktūra – tai parodo, jog tinklas pakankamai gerai atpažįsta, jog vienai salai tenka viena dalelė, bet vargsta su tankio pasiskirstymu per tris salos mazgus.

Norint patikrinti kokią įtaką dalelių tankio parametrų kongavimo spartai ir tikslumui daro sistemos dydis, neuroninis tinklas yra apmokomas ketvirčio užpildos skirtingo dydžio kvazivienmačių gardelių žemiausiai energijos būsenai nustatyti. Tankio struktūros kitimas po kiekvienos iteracijos pavaizduotas 10 pav., kai sistemą sudaro $L + 1 = 21$ (a), $L + 1 = 61$ (b) ir $L + 1 = 101$ (c) mazgai. Matome, kad nepriklausomai nuo sistemos dydžio, kongavi-

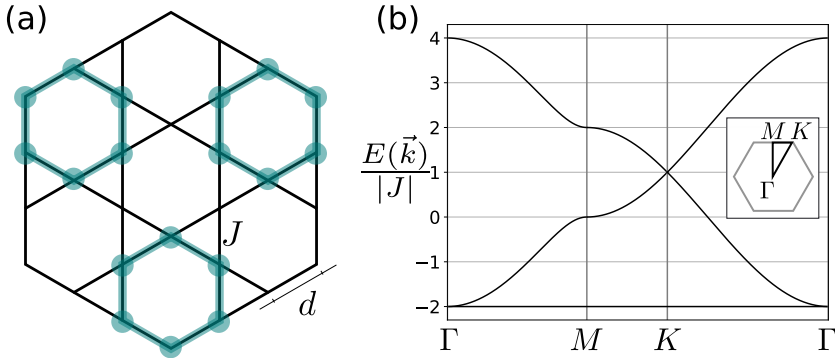


10 pav. Dalelių tankio evoliucija, kai gardelių dydis $L + 1 = 21$ (a), $L + 1 = 61$ (b) ir $L + 1 = 101$ (c) su parametrais $\alpha = 2.5$, $N_{MC} = 5000$ bei $\frac{U}{|J|} = 0.1$.

mas link tankio bangos struktūros prasideda po vidutiniškai vienodo skaičiaus neuroninio tinklo koeficientų atnaujinimų. Esminis požymis atsirandantis didesnėse sistemose yra tankio defektai matomi (c) dalyje, kurie sutrikdo tankio bangos struktūrą. Juos paaiškinti galima tuo, kad tankio banga pradeda formotis skirtingose gardelės dalyse, todėl lokalių formavimosi regionų salų periodiškumas gali nesutapti. Jei tai įvyksta, regionų sandaroje susidaro matomi defektai, kurių pašalinimui reikėtų globalaus tankio struktūros pertvarkymo suvienodinančio periodiškumą. Šis pertvarkymas atitiktų sistemos konfigūracijos pabėgimą iš lokalaus energijos minimumo, tačiau optimizatoriui tai yra sudėtinga problema [194], kuri nėra unikali neuroninio tinklo sprendžiamam uždaviniui. Norint gauti tikslų rezultatą tenka reinicializuoti neuroninių tinklų imtį su naujais atsitiktiniais parametrais.

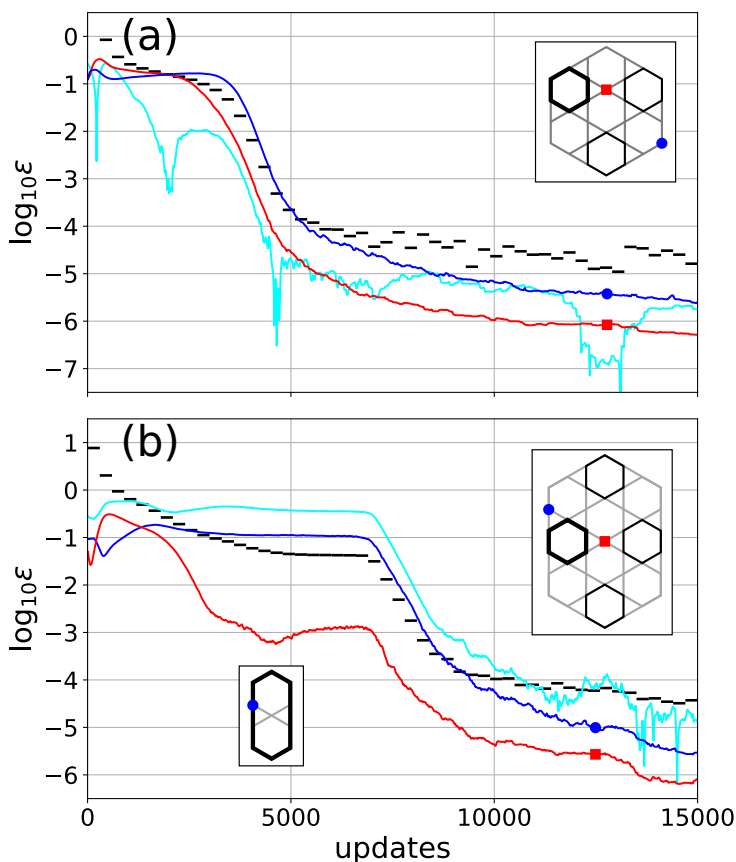
Konvergavimo sparta taip pat priklauso nuo neuroninio tinklo ir gardelės parametru. Didinant paslėptų tinklo mazgų tankį α , stebimų dydžių konvergavimo sparta ir tikslumas didėja, tačiau jie pagerėja optimizavimui skirtu laiko sąskaita. Taip pat konvergavimas priklauso nuo tarpo tarp žemiausios energijos juostos ir pirmos sužadintos energijos juostos – esant didesniam tarpui to pačio tikslumo rezultatui pasiekti užtenka mažesnio skaičiaus iteracijų [A2].

Norint ištirti neuroninio tinklo gebėjimą išmokti žemiausios energijos būsenos tankio struktūrą aukštesnėse dimensijose, analogiškus skaičiavimus galima atlikti ir dvimatei kagome gardelėi. Kagome gardelės pavadinimas kilęs iš japonų kalbos („kago“ – krepšys, „me“ – akis), dėl triheksagoninės geometrijos primenančios tradicinių Japonijoje pinamų bambukinių krepšių raštus (11 pav. (a)). Ši gardelė taip pat turi parametru režimą, palaikantį žemiausią plokščią energijos juostą [192, 195]. Jei gardelės užpilda yra mažesnė už $\frac{1}{9}$, susidaro charakteringos tankio salos. Šios tankio salos (heksagoniniai žiedai) yra paryškintos žaliai 11 pav. (a). Kiekvienoje heksagoninėje saloje yra po vieną dalelę, t.y. kiekvieno žiedo mazgo dalelių tankis atitinka $\bar{n} = \frac{1}{6}$.



11 pav. (a) Kagome gardelės segmentas. Šuolio parametras J jungiantis gardelės mazgus pažymėtas juodomis linijomis. Kiekviena žalia žiedo formos sala žymi vienos lokalizuotos dalelės tankio pasiskirstymą, likę mazgai tušti. (b) Gardelės energijos dispersija ties Brillouin zonos aukštos simetrijos linijomis, kai $J < 0$. Maža įklia vaizduoja Brillouin zoną (pilkas heksagonas) su aukštos simetrijos taškais Γ , M , K ir paryškintus kvazijudesio kiekio takus išilgai kurių yra atvaizduojama dispersija.

Apribotos Boltzmann mašinos veikimą tikrinsime dviems gardelių dydžiams – 30 gardelės mazgų su 3 dalelėmis sistemoje ir 41 mazgas su 4 dalelėmis. Šių gardelių geometrija pavaizduota 12 pav. (a) ir (b) įklijose. Laikysime, kad šuolio parametras yra $J < 0$ ir dalelių tarpusavio stūma begalinė $\frac{U}{|J|} = \infty$. Naudosime tokį patį neuroninio tinklo paslėptų mazgų tankį $\alpha = 2,5$ ir Monte Carlo žingsnių skaičių $N_{MC} = 5000$, kaip ir kvazivienmatei trikampei gardelėi. Mažesnei gardelėi su trimis tankio salomis 12 pav. (a) matome, kad neuroninis tinklas be problemų nustato energiją (juodi brūkšneliai) su tikslumu prilygi-



12 pav. (a) 30 mazgų, 3 dalelių ir (b) 41 mazgų, 4 dalelių kagome gardelės stebimų dydžių logaritminio nuokrypio konvergavimas: žemiausiai energijai (juodi brūkšniai), suminiam tankiui heksagoniniame žiede (žydra kreivė) ir dalelių tankiui pasirinktuose mazguose (raudona ir mėlyna kreivės). Įklijos dešiniuosiuose viršutiniuose kampuose parodo juodas lokalizuotas tankio salas, o paryškintas juodas žiedas žymi salą, kurios suminis tankis yra stebimas. Raudonas kvadratas ir mėlynas skritulys parodo tankio matavimams pasirinktų mazgų poziciją. Maža įklia (b) vaizduoja tarpinę tankio struktūrą, susidarantią mokymosi metu, kai paklaidos nemažėja.

namu kvazivienmatės trikampės gardelės atvejui. Sekant atsitiktinai parinktų dviejų tuščių mazgų tankio nuokrypį, įsitikiname, kad globali tankio struktūra nustatoma itin tiksliai. Šie taškai pažymėti raudonu kvadratu ir mėlynu skrituliu įklijoje bei atitinka raudoną ir mėlyną evoliucijos kreives. Žydra linija žymi tankio nuokrypį nuo tikslios vertės įklijoje paryškintame tankio žiede ir ji leidžia įsitikinti, kad žiede tiksliai lokalizuota viena dalelė. Panašūs rezultatai stebimi ir didesnėje sistemoje 12 pav. (b). Pagrindinis skirtumas yra atsirandanti atnaujinimų sritis, kurioje tam tikrą skaičių iteracijų nuokrypiai

praktiškai nekinta. Šioje srityje tinklas patenka į lokalų energijos minimumą, kuriame susidaro struktūra, pavaizduota 12 pav. (b) apatinėje įklijoje. Šioje tarpinėje struktūroje, dėl banginių būsenų destruktvyvos interferencijos, centrinis mazgas nenori būti užpildytas, todėl optimizatorius užtrunka šiek tiek ilgiau atlikdamas vietinį pertvarkymą į viendalelinę heksagoninę tankio salą.

Pasitelkiant apribotos Boltzmann architektūros dirbtinius neuroninius tinklus, išanalizavome žemiausios energijos būsenos kodavimo tikslumą kvazivienmatėms trikampėms ir dvimatėms kagome gardelėms su plokščiomis energijos juostomis. Tinklas vedamas energijos minimizavimo sugebėjo sėkmingai atpažinti globalų sistemų tankio pasiskirstymą. Tušti gardelių mazgai atskiriantys kompaktiškas lokalizuotas viendaleles bangines būsenas randami itin dideliu tikslumu, prilyginamu sukongvergavusios energijos tikslumui. Lokalaus tankio pasiskirstymo tikslumas, apskaičiuotas kiekvienos kvazivienmatės trikampės gardelės tankio salos viduje, yra eile mažesnis. Pastebėta, kad mazgų skaičiaus didinimas sistemose neturi įtakos konvergavimo spartai ir tikslumui, tačiau didėja tikimybė, kad tinklo parametrai dažniau užstrigs į tašką atitinkantį lokalų energijos minimumą. Tai lemia lokalių tankio defektų susidarymą, kurie sulėtina konvergavimą arba iš vis neleidžia neuroniniui tinklui pasiekti žemiausios energijos būsenos. Norint apeiti šią problemą tenka tinklą reinitializuoti arba ieškoti optimizavimo metodų patobulinimų.

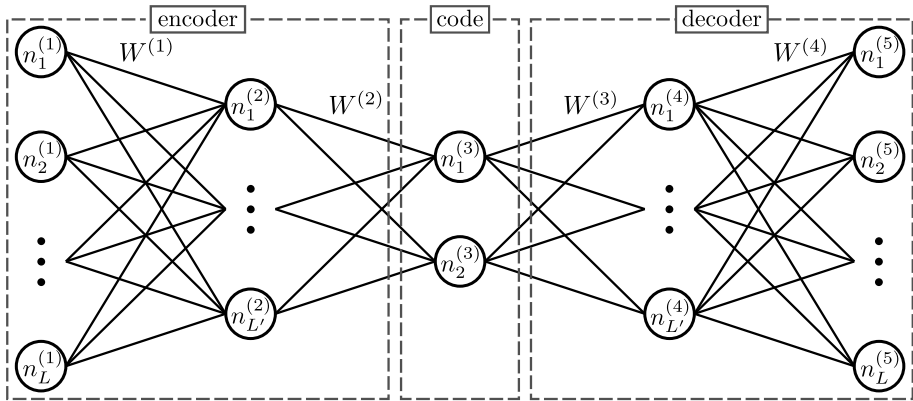
Žemiausios energijos būsenos įverčio patikslinimas taikant autoenkoderį

Kvantinė būsena yra aprašoma Hilbert erdvės vektoriumi. Sistemai sudarytai iš N sukinių su m laisvės laipsnių reikia m^N koeficientų būsenai nusakyti. Koeficientų skaičius auga eksponentiškai didinant sukinių skaičių ir greitai tampa skaitmeniškai neapdorojamu net ir nedidelėms $N \sim 10^4$ dalelių sistemoms tiriamoms šaltųjų atomų eksperimentuose. Hilberto erdvė yra milžiniška [196,197]. Laimei, dažniausiai yra įdomios žemiausios energijos būsenos. Tai leidžia skaitiniams metodams koncentruotis ties mažu Hilbert erdvės poerdviu, kuriame tos būsenos gyvena. Šiai daugdarai pasiekti naudojamos įvairios strategijos – daugiadalelinės kvantinės problemos kompleksiško redukavimas, pasitelkiant projekcijos operatorių metodus [198], žemiausios energijos būsenos skaičiavimas naudojant menamo laiko evoliuciją [199,200], variacinius metodus efektyviai atvaizduojančius banginę būseną kaip tenzorinį tinklą [54,55] arba dirbtinius neuroninius tinklus [57,60,63]. Galiausiai, šių metodų išvestis duoda žemiausios energijos būsenos įvertį.

Šiame skyrelyje nagrinėsime dirbtinį neuroninį tinklą vadinamą tiesioginio sklidimo autoenkoderiu [201]. Jis bus taikomas antrinei triukšmingų būsenų analizei, pavyzdžiui sugeneruotų aukščiau paminėtų apytikslų metodų būdu. Darant prielaidą, kad skaitmeniniai metodai sugeneruoja būseną su paklaidom

atsirandančiom dėl pačių metodų taikomų aproksimacijų arba atrankos ir optimizavimo algoritmų atsitiktinumų, mes galime panaudoti šių būsenų imtį autoenkoderio apmokymui. Autoenkoderis sumažina duomenų dimensiškumą užkoduodamas juos į žemesnės dimensijos poerdvį. Užkoduotos ir dekodautos autoenkoderio struktūros analizė leis nustatyti žemiausių energijos būsenų atskiriamumą ir potencialiai išrinkti rezultatą, kuris yra tikslesnis už bangines funkcijas naudotas autoenkoderio apmokymui.

Tiesioginio sklidimo autoenkoderis yra sudarytas iš trijų dalių. Pirmą dalį užkoduoja įvesties duomenis į neuroninio tinklo sluoksnius, kurių dydis su kiekvienu sluoksniu mažėja. Antra dalis yra tinklo sluoksnis su mažiausiu mazgų skaičiumi, vadinamas kodo arba latentiniu sluoksniu. Jis saugo labiausiai suspaustą informaciją apie sistemą. Galiausiai, trečia dalis susideda iš palaiptiesniui didėjančių sluoksnių iki tol, kol pasiekiamas sluoksnis lygus įvesties sluoksnio dydžiui. Ši dalis dekoduoja suspaustą informaciją. Autoenkoderio, susidedančio iš penkių sluoksnių, pavyzdys pateiktas 13 pav. bei išskirtos užkodavimo (encoder), kodo (code) ir dekodavimo (decoder) dalys. Mazgai pažymėti apskritimais su koeficientais $n_j^{(i)}$, su superskriptu nurodančiu sluoksnio numerį, subskriptu – mazgo numerį. Koeficientų matricos $W^{(i)}$, siejančios mazgus, atitinka mazgus jungiančias linijas tarp i ir $i + 1$ sluoksnio.



13 pav. Schematinis penkių sluoksnių autoenkoderio vaizdavimas.

Gavęs įvesties vektorį $\vec{n}^{(1)} = (n_1^{(1)}, \dots, n_L^{(1)})$, autoenkoderis suskaičiuoja išvesties vektorius taikydamas tiesioginio sklidimo modelio procedūrą. Tai yra procedūra, kuri priėmusi pirmo sluoksnio koeficientus sugeneruoja visų likusių sluoksnių koeficientus iteratyviai:

$$\vec{n}^{(i+1)} = \sigma(W^{(i)}\vec{n}^{(i)} + \vec{b}^{(i)}). \quad (15)$$

Čia $\vec{b}^{(i)}$ yra sluoksnių pataisų koeficientas ir σ – aktyvacijos funkcija. Neuroninis tinklas apmokomas minimizuojant vidutinį kvadratinį nuokrypį tarp įvesties ir išvesties mazgų koeficientų. Svoriai $W^{(i)}$ ir $\vec{b}^{(i)}$ atnaujinami atgalinio

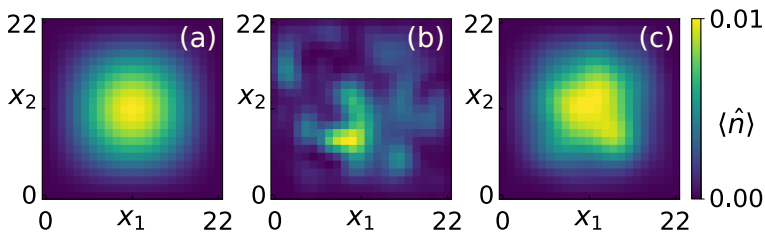
propagavimo metodu [202, 203]. Tolimesniems skaičiavimams naudojamas autoenkoderis implementuotas naudojant Keras biblioteką [204]. Laikysime, kad sluoksniai sudaryti iš L -100-50-25-2-25-50-100- L mazgų sekos, kai L – įvesties mazgų skaičius. Aktyvacijos funkcija σ yra hiperbolinis tangentas $\tanh(\cdot)$, nes į jos sugeneruotą išvestį patenka visos įmanomos normalizuoto vektoriaus koeficientų vertės. Tinklo apmokymo imtis susideda iš 1000 vektorių, o tinklo koeficientai viso mokymosi metu atnaujinami 3000 kartų.

Kiekviena įvesties būseną, naudojama autoenkoderio apmokymui, yra superpozicija iš N fizikinės sistemos žemiausios energijos tikrinių būsenų. Laikysime, kad kiekvienos tikrinės būsenos indėlis (tikimybės amplitudės kvadratas) yra sugeneruotas pagal vienetinio intervalo padalinimo principą [205], kai iš laipsnio p polinominio tikimybinio skirstinio atsitiktinai išrenkami $N - 1$ taškai padalinantys vienetinę atkarpą į N atkarpų. Šių atkarpų ilgiai priskiriami tikrinių būsenų svoriams taip, kad vidutiniškai visose imties vektoriuose didžiausią indėlį turėtų žemiausia energijos būseną. Turėdami tokią triukšmingą apmokymo imtį bandysime nustatyti tikslią žemiausios būsenos formą iš autoenkoderio savybių.

Nagrinėjant modelinę sistemą aprašomą ortogonaliais vektoriais gautais iš atsitiktinės matricos QR dekompozicijos ir pasvertais ankstesnėje pastraipoje minimu metodu, stebime kodo sluoksnio dėsningumus autoenkoderyje apmokytame šių vektorių superpozicijomis. Esant vienam dominuojančiam ortogonaliam vektoriui, nustatyti jo koeficientus vien iš pradinės apmokymo imties taškų skirstinio dvimačiame kodo sluoksnyje yra sudėtinga. Išvaikščiojus visą kodo sluoksnio erdvę matome, kad autoenkoderis gali duoti daug tikslesnę ieškomo vektoriaus vertę už turimas triukšmingų bandinių vertes, tačiau norint ją sugeneruoti, reikia žinoti tikslo funkciją, leidžiančią įvertinti išvesties gerumą. Fizikinei sistemai tikslo funkcija gali būti energija, gauta paveikus hamiltonianu į išvesties būseną. Tuomet varijuojant kodo sluoksnio parametrus galime rasti išvesties vektorių, kuris minimizuoja energiją. Šiuo būdu pabandysime surasti žemiausios enerijos būseną dvimatei kvadratinei gardelei ir kvazivienmatei trikampelei gardelei.

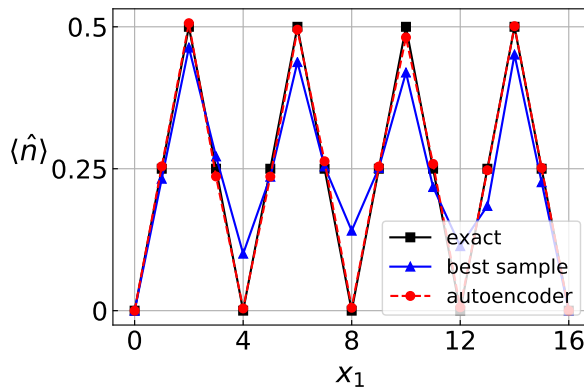
Tarkim, mūsų nagrinėjama dvimatė kvadratinė gardelė yra sudaryta iš 23×23 mazgų ir aprašoma stipraus ryšio artinio modeliu su vienetiniais šuolio parametrais tarp artimiausių mazgų. Sugeneravę triukšmingų būsenų rinkinį, sudarytą iš šios gardelės žemiausių energijos būsenų superpozicijų taip, kad žemiausios energijos būsenos dedamoji būtų didžiausia, jomis apmokome autoenkoderį. Pasinaudodami AdaMax optimizatoriumi vaikštome po kodo sluoksnį tol, kol randamas išvesties vektorius minimizuojantis energiją. Galime palyginti šiuo metodu gautą būsenos tankį $\langle \hat{n} \rangle$ 14 pav. (c) su tiksliau (a) bei geriausiu apmokymams naudoto vektoriaus tankiu (b). Matome, kad atsakymas nėra idealus, tačiau kokybiškai daug tikslesnis už geriausio bandinio.

Atliekant analogiškus skaičiavimus kvazivienmatei gardelei su parame-



14 pav. (a) Dvimatės kvadratinės gardelės būsenos tankio $\langle \hat{n} \rangle$ priklausomybė nuo erdviųjų koordinatėjų, kai būseną yra: (a) tiksliai žemiausios energijos būseną, (b) apmokymui naudojamas būsenos vektorius su didžiausiu persiklojimu su tikslia būseną ir (c) autoenkoderio pagalba rastas sprendinys.

trais palaikančiais izoliuotas tankio salas (15 pav. juodi kvadratai) žemiausioje energijos būsenoje, matome, kad minimizavus energiją autoenkoderis gauna būseną pasižyminčią charakteringa tankio bangos struktūra (raudoni skrituliai), kurios nesimato geriausiame triukšmingame bandinyje (mėlyni trikampiai).



15 pav. Kvazivienmatės trikampės gardelės dalelių tankio priklausomybė nuo koordinatės, kai sistema yra žemiausioje energijos būsenoje (juodi kvadratai), triukšmingoje būsenoje turinčioje didžiausią persiklojimą su tikslia būseną (mėlyni trikampiai) ir apytikslėje būsenoje gautoje pasitelkiant autoenkoderį (raudoni skrituliai).

Autoenkoderis sėkmingai pagerino žemiausios energijos būsenos įvertį abiejų nagrinėtų gardelių atveju, turėdamas tik triukšmingą superpozicijų aibę su dominuojančiu žemiausios energijos būsenos indėliu. Nors šių sistemų žemiausios energijos būsenos yra labai skirtingos ir turi reikšmingai besiskiriančią koeficientų skaičių, jų apskaičiavimas tos pačios struktūros autoenkoderiu neturi reikšmingos įtakos rekonstravimo kokybei. Tai pabrėžia autoenkoderio universalumą.

Išvados

Pirmoje disertacijos dalyje mes pasiūlėme naujo tipo sistemą – laiko-erdvės kristalinę struktūrą, kuri pasižymi periodiškumu tiek erdvėje, tiek sintetinėje laiko dimensijoje atsirandančioje dėl periodinio gardelės purtymo ties rezonansu. Pateiktas kvantinis šios sistemos aprašymas gautas pasitelkiant įžvalgas iš klasikinio vaizdinio ir sukonstruotas konkretus kvazivienmatės laiko-erdvės kristalinės struktūros pavyzdys. Taip pat parodyta, kad tokią sistemą galima generalizuoti iki keturmačių ir šešiamatinių struktūrų.

1. Rezonansiniu dažniu purtoma gardelė palaiko parametrų režimą, kuriame susidaro laiko-erdvės kristalinė struktūra – erdvinė gardelė su periodine laikine struktūra kiekviename erdvinės gardelės mazge.

Pasitelkiant papildomą potencialo purtymo moduliavimą yra sukuriamas energijos išderinimas, sustabdantis dalelių tuneliavimą tarp skirtingų laikinės dimensijos gardelės mazgų. Sistemą veikiant Raman lazerio pluoštais šį tuneliavimą galima atkurti kartu indukuojant kontroliuojamą fazę. Šuolių fazės valdymas leidžia gardelėje sukurti dirbtinius magnetinius srautus reikalingus topologiniams efektams įgyvendinti. Tai iliustruojama topologiškai apsaugotų kraštinių būsenų atsiradimu šešiamatiose laiko-erdvės kristalinėse struktūrose.

2. Laiko-erdvės kristalinės struktūros leidžia tirti šešiamatinių gardelių topologines savybes.

Antroje disertacijos dalyje iš pradžių nagrinėjome dirbtinio neuroninio tinklo su apribotos Boltzmann mašinos architektūra gebėjimą išmokti žemiausios energijos būsenos bruožus plokščių energijos juostų gardelių modeliuose – kvazivienmatėje trikampėje ir baigtinėje 2D kagome gardelėse. Mokymosi procedūra buvo paremta sistemų energijos minimizavimu. Abiejų tirtų gardelių žemiausių energijos būsenų tikimybės tankis turi globalią tankio bangos formos struktūrą, kurią neuroninis tinklas sėkmingai išmoksta, tačiau lokali tankio struktūra atpažįstama mažesniu tikslumu.

3. Apribotos Boltzmann mašinos architektūros neuroniniai tinklai sėkmingai koduoja plokščių energijos juostų gardelių modelių globalią banginės būsenos tikimybės tankio struktūrą, pasitelkdami energijos minimizavimą.

Atliekant neuroninio tinklo apmokymą didelėms gardelėms padidėja tikimybė, kad stebimi būsenos bruožai nepasieks tikslų verčių, bet užstrigs konfigūracijose atitinkančiose lokalų sistemos energijos minimumą. Tai įvyksta dėl globalių tankio struktūrų formavimosi skirtingose lokaliuose srityse. Šių sričių sandūroje susidaro defektas, kuriam pašalinti reikalingas globalus tankio perskirstymas kainuojantis daug energijos, todėl neuroninio tinklo optimizatorius nesugeba

ištrūkti iš energijos minimumo. Tokiu atveju tenka reinicializuoti mokymosi procedūrą.

4. Dirbtiniai neuroniniai tinklai didelėse sistemose yra linkę užstrigti tikimybės tankio konfigūracijose atitinkančiose lokalius energijos minimumus.

Antros dalies pabaigoje, nagrinėjome kitokios dirbtinio neuroninio tinko architektūros taikymą antrinei duomenų analizei. Tiesioginio sklidimo autoenkoderis buvo panaudotas pačios žemiausios energijos būsenos išgryninimui iš duotos triukšmingų banginių funkcijų aibės. Šios aibės elementai yra žemiausių energijos būsenų superpozicija, kurioje didžiausią svorį vidutiniškai turi pačios žemiausios energijos būsenos. Apmokytas autoenkoderis užkodavo pakankamai informacijos, kad galėtų atkurti tikslesnę žemiausios energijos būsenos įvertį, duodantį beveik idealų persiklojimą su tikslu rezultatu.

5. Autoenkoderio taikymas triukšmingų duomenų analizei leidžia patikslinti žemiausios energijos būsenos įvertį, turint aibę apytiksliai banginių būsenų superpozicijų su dominuojančiu žemiausios energijos būsenos indėliu.

BIBLIOGRAPHY

- [1] M. H. Anderson, J. R. Ensher, M. R. Matthews, C. E. Wieman, E. A. Cornell, Observation of Bose-Einstein Condensation in a Dilute Atomic Vapor, *Science* **269**(5221) (1995).
- [2] K. B. Davis, M.-O. Mewes, M. R. Andrews, N. J. van Druten, D. S. Durfee, D. M. Kurn, W. Ketterle, Bose-Einstein Condensation in a Gas of Sodium Atoms, *Phys. Rev. Lett.* **75**(22), 3969–3973 (1995).
- [3] S. N. Bose, Plancks Gesetz und Lichtquantenhypothese, *Z. Phys.* **26**(1), 178–181 (1924).
- [4] A. Einstein, Quantentheorie des einatomigen idealen gases, *Sitzungber. Kgl. Akad. Wiss.* (261) (1924).
- [5] D. S. Jin, J. R. Ensher, M. R. Matthews, C. E. Wieman, E. A. Cornell, Collective Excitations of a Bose-Einstein Condensate in a Dilute Gas, *Phys. Rev. Lett.* **77**(3), 420–423 (1996).
- [6] K. W. Madison, F. Chevy, W. Wohlleben, J. Dalibard, Vortex Formation in a Stirred Bose-Einstein Condensate, *Phys. Rev. Lett.* **84**(5), 806–809 (2000).
- [7] F. S. Cataliotti, S. Burger, C. Fort, P. Maddaloni, F. Minardi, A. Trombettoni, A. Smerzi, M. Inguscio, Josephson junction arrays with Bose-Einstein condensates, *Science* **293**(5531), 843–846 (2001).
- [8] B. DeMarco, D. S. Jin, Onset of fermi degeneracy in a trapped atomic Gas, *Science* **285**(5434), 1703–1706 (1999).
- [9] M. W. Zwierlein, J. R. Abo-Shaeer, A. Schirotzek, C. H. Schunck, W. Ketterle, Vortices and superfluidity in a strongly interacting Fermi gas, *Nature* **435**(7045), 1047–1051 (2005).
- [10] S. Giorgini, L. P. Pitaevskii, S. Stringari, Theory of ultracold atomic Fermi gases, *Rev. Mod. Phys.* **80**(4), 1215–1274 (2008).
- [11] P. Windpassinger, K. Sengstock, Engineering novel optical lattices, *Rep. Prog. Phys.* **76**(8), 086401 (2013).
- [12] R. P. Feynman, Simulating physics with computers, *Int. J. Theor. Phys.* **21**(6), 467–488 (1982).

- [13] F. Schäfer, T. Fukuhara, S. Sugawa, Y. Takasu, Y. Takahashi, Tools for quantum simulation with ultracold atoms in optical lattices, *Nat. Rev. Phys.* **2**(8), 411–425 (2020).
- [14] J. Hubbard, Electron correlations in narrow energy bands, *Proc. R. Soc. A: Math. Phys. Eng. Sci.* **276**(1365), 238–257 (1963).
- [15] W. Hofstetter, J. I. Cirac, P. Zoller, E. Demler, M. D. Lukin, High-Temperature Superfluidity of Fermionic Atoms in Optical Lattices, *Phys. Rev. Lett.* **89**(22), 220407 (2002).
- [16] D. Jaksch, P. Zoller, The cold atom Hubbard toolbox, *Ann. Phys.* **315**(1), 52–79 (2005).
- [17] O. Dutta, M. Gajda, P. Hauke, M. Lewenstein, D.-S. Lühmann, B. A. Malomed, T. Sowiński, J. Zakrzewski, Non-standard Hubbard models in optical lattices: a review, *Rep. Prog. Phys.* **78**(6), 066001 (2015).
- [18] T. Moriya, K. Ueda, Antiferromagnetic spin fluctuation and superconductivity, *Rep. Prog. Phys.* **66**(8), 1299–1341 (2003).
- [19] P. A. Lee, N. Nagaosa, X.-G. Wen, Doping a Mott insulator: Physics of high-temperature superconductivity, *Rev. Mod. Phys.* **78**(1), 17–85 (2006).
- [20] L.-M. Duan, E. Demler, M. D. Lukin, Controlling Spin Exchange Interactions of Ultracold Atoms in Optical Lattices, *Phys. Rev. Lett.* **91**(9), 090402 (2003).
- [21] D. Jaksch, C. Bruder, J. I. Cirac, C. W. Gardiner, P. Zoller, Cold Bosonic Atoms in Optical Lattices, *Phys. Rev. Lett.* **81**(15), 3108–3111 (1998).
- [22] M. Greiner, O. Mandel, T. Esslinger, T. W. Hänsch, I. Bloch, Quantum phase transition from a superfluid to a Mott insulator in a gas of ultracold atoms, *Nature* **415**(6867), 39–44 (2002).
- [23] C. Meldgin, U. Ray, P. Russ, D. Chen, D. M. Ceperley, B. DeMarco, Probing the Bose glass–superfluid transition using quantum quenches of disorder, *Nat. Phys.* **12**(7), 646–649 (2016).
- [24] K. Sacha, J. Zakrzewski, Time crystals: a review, *Rep. Prog. Phys.* **81**(1), 016401 (2017).
- [25] K. Sacha, *Time Crystals* (Springer International Publishing, Cham, Switzerland, 2020).
- [26] L. Guo, M. Marthaler, G. Schön, Phase Space Crystals: A New Way to Create a Quasienergy Band Structure, *Phys. Rev. Lett.* **111**(20), 205303 (2013).
- [27] G. V. Chester, Speculations on Bose-Einstein Condensation and Quantum Crystals, *Phys. Rev. A* **2**(1), 256–258 (1970).

- [28] M. A. Norcia, C. Politi, L. Klaus, E. Poli, M. Sohmen, M. J. Mark, R. N. Bisset, L. Santos, F. Ferlaino, Two-dimensional supersolidity in a dipolar quantum gas, *Nature* **596**(7872), 357–361 (2021).
- [29] J. Struck, J. Simonet, K. Sengstock, Spin-orbit coupling in periodically driven optical lattices, *Phys. Rev. A* **90**(3), 031601 (2014).
- [30] A. Eckardt, Colloquium: Atomic quantum gases in periodically driven optical lattices, *Rev. Mod. Phys.* **89**(1), 011004 (2017).
- [31] V. Galitski, I. B. Spielman, Spin-orbit coupling in quantum gases, *Nature* **494**(7435), 49–54 (2013).
- [32] N. Goldman, G. Juzeliūnas, P. Öhberg, I. B. Spielman, Light-induced gauge fields for ultracold atoms, *Rep. Prog. Phys.* **77**(12), 126401 (2014).
- [33] L. F. Livi, G. Cappellini, M. Diem, L. Franchi, C. Clivati, M. Frittelli, F. Levi, D. Calonico, J. Catani, M. Inguscio, L. Fallani, Synthetic Dimensions and Spin-Orbit Coupling with an Optical Clock Transition, *Phys. Rev. Lett.* **117**(22), 220401 (2016).
- [34] K. v. Klitzing, G. Dorda, M. Pepper, New Method for High-Accuracy Determination of the Fine-Structure Constant Based on Quantized Hall Resistance, *Phys. Rev. Lett.* **45**(6), 494–497 (1980).
- [35] M. Aidelsburger, M. Atala, M. Lohse, J. T. Barreiro, B. Paredes, I. Bloch, Realization of the Hofstadter Hamiltonian with Ultracold Atoms in Optical Lattices, *Phys. Rev. Lett.* **111**(18), 185301 (2013).
- [36] M. Z. Hasan, C. L. Kane, Colloquium: Topological insulators, *Rev. Mod. Phys.* **82**(4), 3045–3067 (2010).
- [37] X.-L. Qi, S.-C. Zhang, Topological insulators and superconductors, *Rev. Mod. Phys.* **83**(4), 1057–1110 (2011).
- [38] C.-K. Chiu, J. C. Y. Teo, A. P. Schnyder, S. Ryu, Classification of topological quantum matter with symmetries, *Rev. Mod. Phys.* **88**(3), 035005 (2016).
- [39] M. J. Gilbert, Topological electronics, *Commun. Phys.* **4**(70), 1–12 (2021).
- [40] M. He, H. Sun, Q. L. He, Topological insulator: Spintronics and quantum computations, *Front. Phys.* **14**(4), 1–16 (2019).
- [41] A. Celi, P. Massignan, J. Ruseckas, N. Goldman, I. B. Spielman, G. Juzeliūnas, M. Lewenstein, Synthetic Gauge Fields in Synthetic Dimensions, *Phys. Rev. Lett.* **112**(4), 043001 (2014).
- [42] T. Ozawa, H. M. Price, Topological quantum matter in synthetic dimensions, *Nat. Rev. Phys.* **1**(5), 349–357 (2019).
- [43] H. M. Price, O. Zilberberg, T. Ozawa, I. Carusotto, N. Goldman, Four-Dimensional Quantum Hall Effect with Ultracold Atoms, *Phys. Rev. Lett.* **115**(19), 195303 (2015).

- [44] M. Lohse, C. Schweizer, H. M. Price, O. Zilberberg, I. Bloch, Exploring 4D quantum Hall physics with a 2D topological charge pump, *Nature* **553**(7686), 55–58 (2018).
- [45] I. Petrides, H. M. Price, O. Zilberberg, Six-dimensional quantum Hall effect and three-dimensional topological pumps, *Phys. Rev. B* **98**(12), 125431 (2018).
- [46] Y. E. Kraus, O. Zilberberg, Quasiperiodicity and topology transcend dimensions, *Nat. Phys.* **12**(7), 624–626 (2016).
- [47] X.-L. Qi, T. L. Hughes, S.-C. Zhang, Topological field theory of time-reversal invariant insulators, *Phys. Rev. B* **78**(19), 195424 (2008).
- [48] J. Fröhlich, B. Pedrini, New applications of the chiral anomaly, in *Mathematical Physics 2000* (Imperial College Press, London, UK, 2000), 9–47.
- [49] S.-C. Zhang, J. Hu, A Four-Dimensional Generalization of the Quantum Hall Effect, *Science* (2001).
- [50] M. P. Gelfand, R. R. P. Singh, D. A. Huse, Perturbation expansions for quantum many-body systems, *J. Stat. Phys.* **59**(5), 1093–1142 (1990).
- [51] A. M. Rey, K. Burnett, R. Roth, M. Edwards, C. J. Williams, C. W. Clark, Bogoliubov approach to superfluidity of atoms in an optical lattice, *J. Phys. B: At. Mol. Opt. Phys.* **36**(5), 825–841 (2003).
- [52] A. Avella, F. Mancini, *Strongly Correlated Systems: Numerical Methods* (Springer, Berlin, Germany, 2013).
- [53] D. Raventós, T. Graß, M. Lewenstein, B. Juliá-Díaz, Cold bosons in optical lattices: a tutorial for exact diagonalization, *J. Phys. B: At. Mol. Opt. Phys.* **50**(11), 113001 (2017).
- [54] U. Schollwöck, The density-matrix renormalization group, *Rev. Mod. Phys.* **77**(1), 259–315 (2005).
- [55] R. Orús, Tensor networks for complex quantum systems, *Nat. Rev. Phys.* **1**, 538–550 (2019).
- [56] J. Kolorenč, L. Mitas, Applications of quantum Monte Carlo methods in condensed systems, *Rep. Prog. Phys.* **74**(2), 026502 (2011).
- [57] G. Carleo, M. Troyer, Solving the quantum many-body problem with artificial neural networks, *Science* **355**(6325), 602–606 (2017).
- [58] T. Vieijra, C. Casert, J. Nys, W. De Neve, J. Haegeman, J. Ryckebusch, F. Verstraete, Restricted Boltzmann Machines for Quantum States with Non-Abelian or Anyonic Symmetries, *Phys. Rev. Lett.* **124**(9), 097201 (2020).
- [59] V. Vargas-Calderón, H. Vinck-Posada, F. A. González, Phase Diagram Reconstruction of the Bose–Hubbard Model with a Restricted Boltzmann Machine Wavefunction, *J. Phys. Soc. Jpn.* **89**(9), 094002 (2020).

- [60] H. Saito, M. Kato, Machine Learning Technique to Find Quantum Many-Body Ground States of Bosons on a Lattice, *J. Phys. Soc. Jpn.* **87**(1), 014001 (2017).
- [61] C. Roth, A. H. MacDonald, Group Convolutional Neural Networks Improve Quantum State Accuracy, arXiv:2104.05085 (2021).
- [62] H. M. Price, T. Ozawa, N. Goldman, Synthetic dimensions for cold atoms from shaking a harmonic trap, *Phys. Rev. A* **95**(2), 023607 (2017).
- [63] H. Saito, Solving the Bose–Hubbard Model with Machine Learning, *J. Phys. Soc. Jpn.* **86**(9), 093001 (2017).
- [64] J. Chen, S. Cheng, H. Xie, L. Wang, T. Xiang, Equivalence of restricted Boltzmann machines and tensor network states, *Phys. Rev. B* **97**(8), 085104 (2018).
- [65] R. Grimm, M. Weidemüller, Y. B. Ovchinnikov, Optical Dipole Traps for Neutral Atoms, in *Advances In Atomic, Molecular, and Optical Physics* (Academic Press, Cambridge, MA, USA, 2000), volume 42, 95–170.
- [66] M. Lewenstein, A. Sanpera, V. Ahufinger, Ultracold Atoms in Optical Lattices: Simulating quantum many-body systems, in *Ultracold Atoms in Optical Lattices* (Oxford University Press, Oxford, England, UK, 2012).
- [67] N. B. Delone, V. P. Krainov, AC Stark shift of atomic energy levels, *Phys.-Usp.* **42**(7), 669–687 (1999).
- [68] H. Pichler, J. Schachenmayer, A. J. Daley, P. Zoller, Heating dynamics of bosonic atoms in a noisy optical lattice, *Phys. Rev. A* **87**(3), 033606 (2013).
- [69] N. W. Ashcroft, N. D. Mermin, *Solid state physics* (Brooks/Cole, Florence, KY, USA, 1976).
- [70] O. Morsch, M. Oberthaler, Dynamics of Bose-Einstein condensates in optical lattices, *Rev. Mod. Phys.* **78**(1), 179–215 (2006).
- [71] D. Leykam, A. Andreanov, S. Flach, Artificial flat band systems: from lattice models to experiments, *Adv. Phys.: X* **3**(1), 1473052 (2018).
- [72] C. Chin, R. Grimm, P. Julienne, E. Tiesinga, Feshbach resonances in ultracold gases, *Rev. Mod. Phys.* **82**(2), 1225–1286 (2010).
- [73] A. L. Fetter, J. D. Walecka, *Quantum Theory of Many-Particle Systems* (McGraw-Hill, Boston, 1971).
- [74] N. Marzari, D. Vanderbilt, Maximally localized generalized Wannier functions for composite energy bands, *Phys. Rev. B* **56**(20), 12847–12865 (1997).
- [75] W. Kohn, Analytic Properties of Bloch Waves and Wannier Functions, *Phys. Rev.* **115**(4), 809–821 (1959).

- [76] N. Marzari, A. A. Mostofi, J. R. Yates, I. Souza, D. Vanderbilt, Maximally localized Wannier functions: Theory and applications, *Rev. Mod. Phys.* **84**(4), 1419–1475 (2012).
- [77] N. Goldman, J. C. Budich, P. Zoller, Topological quantum matter with ultracold gases in optical lattices, *Nat. Phys.* **12**, 639–645 (2016).
- [78] N. R. Cooper, J. Dalibard, I. B. Spielman, Topological bands for ultracold atoms, *Rev. Mod. Phys.* **91**(1), 015005 (2019).
- [79] M. Schreiber, S. S. Hodgman, P. Bordia, H. P. Lüschen, M. H. Fischer, R. Vosk, E. Altman, U. Schneider, I. Bloch, Observation of many-body localization of interacting fermions in a quasirandom optical lattice, *Science* **349**(6250), 842–845 (2015).
- [80] P. Sierant, J. Zakrzewski, Many-body localization of bosons in optical lattices, *New J. Phys.* **20**(4), 043032 (2018).
- [81] J. Dalibard, F. Gerbier, G. Juzeliūnas, P. Öhberg, Colloquium: Artificial gauge potentials for neutral atoms, *Rev. Mod. Phys.* **83**(4), 1523–1543 (2011).
- [82] D. J. Griffiths, D. F. Schroeter, *Introduction to Quantum Mechanics* (Cambridge University Press, Cambridge, England, UK, 2018).
- [83] D. Vanderbilt, *Berry Phases in Electronic Structure Theory: Electric Polarization, Orbital Magnetization and Topological Insulators* (Cambridge University Press, Cambridge, England, UK, 2018).
- [84] Y. Aharonov, D. Bohm, Significance of Electromagnetic Potentials in the Quantum Theory, *Phys. Rev.* **115**(3), 485–491 (1959).
- [85] M. V. Berry, Quantal phase factors accompanying adiabatic changes, *Proc. R. Soc. Lond. A.* **392**(1802), 45–57 (1984).
- [86] A. Tonomura, N. Osakabe, T. Matsuda, T. Kawasaki, J. Endo, S. Yano, H. Yamada, Evidence for Aharonov-Bohm effect with magnetic field completely shielded from electron wave, *Phys. Rev. Lett.* **56**(8), 792–795 (1986).
- [87] N. Osakabe, T. Matsuda, T. Kawasaki, J. Endo, A. Tonomura, S. Yano, H. Yamada, Experimental confirmation of Aharonov-Bohm effect using a toroidal magnetic field confined by a superconductor, *Phys. Rev. A* **34**(2), 815–822 (1986).
- [88] M. Ballesteros, R. Weder, The Aharonov–Bohm effect and Tonomura et al. experiments: Rigorous results, *J. Math. Phys.* **50**(12), 122108 (2009).
- [89] E. Zohar, J. I. Cirac, B. Reznik, Quantum simulations of lattice gauge theories using ultracold atoms in optical lattices, *Rep. Prog. Phys.* **79**(1), 014401 (2015).

- [90] L. Tagliacozzo, A. Celi, P. Orland, M. W. Mitchell, M. Lewenstein, Simulation of non-Abelian gauge theories with optical lattices, *Nat. Commun.* **4**(2615), 1–8 (2013).
- [91] L. Barbiero, C. Schweizer, M. Aidelsburger, E. Demler, N. Goldman, F. Grusdt, Coupling ultracold matter to dynamical gauge fields in optical lattices: From flux attachment to \mathbb{Z}_2 lattice gauge theories, *Sci. Adv.* (2019).
- [92] J. M. Luttinger, The Effect of a Magnetic Field on Electrons in a Periodic Potential, *Phys. Rev.* **84**(4), 814–817 (1951).
- [93] K. Jiménez-García, L. J. LeBlanc, R. A. Williams, M. C. Beeler, A. R. Perry, I. B. Spielman, Peierls Substitution in an Engineered Lattice Potential, *Phys. Rev. Lett.* **108**(22), 225303 (2012).
- [94] D. R. Hofstadter, Energy levels and wave functions of Bloch electrons in rational and irrational magnetic fields, *Phys. Rev. B* **14**(6), 2239–2249 (1976).
- [95] F. D. M. Haldane, Model for a Quantum Hall Effect without Landau Levels: Condensed-Matter Realization of the "Parity Anomaly", *Phys. Rev. Lett.* **61**(18), 2015–2018 (1988).
- [96] G. Jotzu, M. Messer, R. Desbuquois, M. Lebrat, T. Uehlinger, D. Greif, T. Esslinger, Experimental realization of the topological Haldane model with ultracold fermions, *Nature* **515**(7526), 237–240 (2014).
- [97] J. Ruostekoski, G. V. Dunne, J. Javanainen, Particle Number Fractionalization of an Atomic Fermi-Dirac Gas in an Optical Lattice, *Phys. Rev. Lett.* **88**(18), 180401 (2002).
- [98] D. Jaksch, P. Zoller, Creation of effective magnetic fields in optical lattices: the Hofstadter butterfly for cold neutral atoms, *New J. Phys.* **5**(1), 56 (2003).
- [99] N. R. Cooper, J. Dalibard, Optical flux lattices for two-photon dressed states, *Europhys. Lett.* **95**(6), 66004 (2011).
- [100] E. J. Bergholtz, Z. Liu, Topological flat band models and fractional Chern insulators, *Int. J. Mod. Phys B* **27**(24), 1330017 (2013).
- [101] J. Motruk, I. Na, Detecting Fractional Chern Insulators in Optical Lattices through Quantized Displacement, *Phys. Rev. Lett.* **125**(23), 236401 (2020).
- [102] S. Raghu, X.-L. Qi, C. Honerkamp, S.-C. Zhang, Topological Mott Insulators, *Phys. Rev. Lett.* **100**(15), 156401 (2008).
- [103] K. Sun, W. V. Liu, A. Hemmerich, S. Das Sarma, Topological semimetal in a fermionic optical lattice, *Nat. Phys.* **8**(1), 67–70 (2012).
- [104] K. Kudo, T. Yoshida, Y. Hatsugai, Higher-Order Topological Mott Insulators, *Phys. Rev. Lett.* **123**(19), 196402 (2019).

- [105] N. Goldman, I. Satija, P. Nikolic, A. Bermudez, M. A. Martin-Delgado, M. Lewenstein, I. B. Spielman, Realistic Time-Reversal Invariant Topological Insulators with Neutral Atoms, *Phys. Rev. Lett.* **105**(25), 255302 (2010).
- [106] B. Béri, N. R. Cooper, \mathbb{Z}_2 Topological Insulators in Ultracold Atomic Gases, *Phys. Rev. Lett.* **107**(14), 145301 (2011).
- [107] X.-J. Liu, L. Jiang, H. Pu, H. Hu, Probing Majorana fermions in spin-orbit-coupled atomic Fermi gases, *Phys. Rev. A* **85**(2), 021603 (2012).
- [108] D. J. Thouless, M. Kohmoto, M. P. Nightingale, M. Den Nijs, Quantized Hall Conductance in a Two-Dimensional Periodic Potential, *Phys. Rev. Lett.* **49**(6), 405–408 (1982).
- [109] M. Kohmoto, Topological invariant and the quantization of the Hall conductance, *Ann. Phys.* **160**(2), 343–354 (1985).
- [110] T. Thonhauser, D. Vanderbilt, Insulator/Chern-insulator transition in the Haldane model, *Phys. Rev. B* **74**(23), 235111 (2006).
- [111] O. Zilberberg, S. Huang, J. Guglielmon, M. Wang, K. P. Chen, Y. E. Kraus, M. C. Rechtsman, Photonic topological boundary pumping as a probe of 4D quantum Hall physics, *Nature* **553**(7686), 59–62 (2018).
- [112] C. H. Lee, Y. Wang, Y. Chen, X. Zhang, Electromagnetic response of quantum Hall systems in dimensions five and six and beyond, *Phys. Rev. B* **98**(9), 094434 (2018).
- [113] T. Fukui, Theory of edge states based on the Hermiticity of tight-binding Hamiltonian operators, *Phys. Rev. Res.* **2**(4), 043136 (2020).
- [114] N. Hao, P. Zhang, Z. Wang, W. Zhang, Y. Wang, Topological edge states and quantum Hall effect in the Haldane model, *Phys. Rev. B* **78**(7), 075438 (2008).
- [115] J.-P. Brantut, J. Meineke, D. Stadler, S. Krinner, T. Esslinger, Conduction of Ultracold Fermions Through a Mesoscopic Channel, *Science* **337**(6098), 1069–1071 (2012).
- [116] L. J. LeBlanc, K. Jiménez-García, R. A. Williams, M. C. Beeler, A. R. Perry, W. D. Phillips, I. B. Spielman, Observation of a superfluid Hall effect, *Proc. Natl. Acad. Sci. U.S.A.* **109**(27), 10811–10814 (2012).
- [117] R. O. Umucalilar, H. Zhai, M. Ö. Oktel, Trapped Fermi Gases in Rotating Optical Lattices: Realization and Detection of the Topological Hofstadter Insulator, *Phys. Rev. Lett.* **100**(7), 070402 (2008).
- [118] E. Alba, X. Fernandez-Gonzalvo, J. Mur-Petit, J. K. Pachos, J. J. Garcia-Ripoll, Seeing Topological Order in Time-of-Flight Measurements, *Phys. Rev. Lett.* **107**(23), 235301 (2011).

- [119] N. Goldman, E. Anisimovas, F. Gerbier, P. Öhberg, I. B. Spielman, G. Juzeliūnas, Measuring topology in a laser-coupled honeycomb lattice: from Chern insulators to topological semi-metals, *New J. Phys.* **15**(1), 013025 (2013).
- [120] E. Zhao, N. Bray-Ali, C. J. Williams, I. B. Spielman, I. I. Satija, Chern numbers hiding in time-of-flight images, *Phys. Rev. A* **84**(6), 063629 (2011).
- [121] L. Wang, A. A. Soluyanov, M. Troyer, Proposal for Direct Measurement of Topological Invariants in Optical Lattices, *Phys. Rev. Lett.* **110**(16), 166802 (2013).
- [122] H. M. Price, N. R. Cooper, Mapping the Berry curvature from semiclassical dynamics in optical lattices, *Phys. Rev. A* **85**(3), 033620 (2012).
- [123] N. Goldman, J. Beugnon, F. Gerbier, Detecting Chiral Edge States in the Hofstadter Optical Lattice, *Phys. Rev. Lett.* **108**(25), 255303 (2012).
- [124] M. Leder, C. Grossert, L. Sitta, M. Genske, A. Rosch, M. Weitz, Real-space imaging of a topologically protected edge state with ultracold atoms in an amplitude-chirped optical lattice, *Nat. Commun.* **7**(13112), 1–8 (2016).
- [125] N. Goldman, J. Dalibard, A. Dauphin, F. Gerbier, M. Lewenstein, P. Zoller, I. B. Spielman, Direct imaging of topological edge states in cold-atom systems, *Proc. Natl. Acad. Sci. U.S.A.* **110**(17), 6736–6741 (2013).
- [126] D. H. Dunlap, V. M. Kenkre, Dynamic localization of a charged particle moving under the influence of an electric field, *Phys. Rev. B* **34**(6), 3625–3633 (1986).
- [127] H. Lignier, C. Sias, D. Ciampini, Y. Singh, A. Zenesini, O. Morsch, E. Arimondo, Dynamical Control of Matter-Wave Tunneling in Periodic Potentials, *Phys. Rev. Lett.* **99**(22), 220403 (2007).
- [128] A. Zenesini, H. Lignier, D. Ciampini, O. Morsch, E. Arimondo, Coherent Control of Dressed Matter Waves, *Phys. Rev. Lett.* **102**(10), 100403 (2009).
- [129] M. S. Rudner, N. H. Lindner, Band structure engineering and non-equilibrium dynamics in Floquet topological insulators, *Nat. Rev. Phys.* **2**(5), 229–244 (2020).
- [130] M. Holthaus, Floquet engineering with quasienergy bands of periodically driven optical lattices, *J. Phys. B: At. Mol. Opt. Phys.* **49**(1), 013001 (2015).
- [131] F. Wilczek, Quantum Time Crystals, *Phys. Rev. Lett.* **109**(16), 160401 (2012).
- [132] H. Watanabe, M. Oshikawa, Absence of Quantum Time Crystals, *Phys. Rev. Lett.* **114**(25), 251603 (2015).

- [133] L. Guo, P. Liang, Condensed matter physics in time crystals, *New J. Phys.* **22**(7), 075003 (2020).
- [134] V. K. Kozin, O. Kyriienko, Quantum Time Crystals from Hamiltonians with Long-Range Interactions, *Phys. Rev. Lett.* **123**(21), 210602 (2019).
- [135] K. Sacha, Modeling spontaneous breaking of time-translation symmetry, *Phys. Rev. A* **91**(3), 033617 (2015).
- [136] D. V. Else, B. Bauer, C. Nayak, Floquet Time Crystals, *Phys. Rev. Lett.* **117**(9), 090402 (2016).
- [137] N. Y. Yao, A. C. Potter, I.-D. Potirniche, A. Vishwanath, Discrete Time Crystals: Rigidity, Criticality, and Realizations, *Phys. Rev. Lett.* **118**(3), 030401 (2017).
- [138] Z. Gong, R. Hamazaki, M. Ueda, Discrete Time-Crystalline Order in Cavity and Circuit QED Systems, *Phys. Rev. Lett.* **120**(4), 040404 (2018).
- [139] J. Zhang, P. W. Hess, A. Kyprianidis, P. Becker, A. Lee, J. Smith, G. Pagano, I.-D. Potirniche, A. C. Potter, A. Vishwanath, N. Y. Yao, C. Monroe, Observation of a discrete time crystal, *Nature* **543**(7644), 217–220 (2017).
- [140] S. Choi, J. Choi, R. Landig, G. Kucsko, H. Zhou, J. Isoya, F. Jelezko, S. Onoda, H. Sumiya, V. Khemani, C. von Keyserlingk, N. Y. Yao, E. Demler, M. D. Lukin, Observation of discrete time-crystalline order in a disordered dipolar many-body system, *Nature* **543**(7644), 221–225 (2017).
- [141] J. Rovny, R. L. Blum, S. E. Barrett, Observation of Discrete-Time-Crystal Signatures in an Ordered Dipolar Many-Body System, *Phys. Rev. Lett.* **120**(18), 180603 (2018).
- [142] J. Smits, L. Liao, H. T. C. Stoof, P. van der Straten, Observation of a Space-Time Crystal in a Superfluid Quantum Gas, *Phys. Rev. Lett.* **121**(18), 185301 (2018).
- [143] H. Keßler, P. Kongkhambut, C. Georges, L. Mathey, J. G. Cosme, A. Hemmerich, Observation of a Dissipative Time Crystal, *Phys. Rev. Lett.* **127**(4), 043602 (2021).
- [144] A. Kyprianidis, F. Machado, W. Morong, P. Becker, K. S. Collins, D. V. Else, L. Feng, P. W. Hess, C. Nayak, G. Pagano, N. Y. Yao, C. Monroe, Observation of a prethermal discrete time crystal, *Science* **372**(6547), 1192–1196 (2021).
- [145] P. Hannaford, K. Sacha, Condensed matter physics in big discrete time crystals, *arXiv:2202.05544* (2022).
- [146] D. Delande, L. Morales-Molina, K. Sacha, Three-Dimensional Localized-Delocalized Anderson Transition in the Time Domain, *Phys. Rev. Lett.* **119**(23), 230404 (2017).

- [147] K. Giergiel, A. Kosior, P. Hannaford, K. Sacha, Time crystals: Analysis of experimental conditions, *Phys. Rev. A* **98**(1), 013613 (2018).
- [148] P. Matus, K. Giergiel, K. Sacha, Anderson complexes: Bound states of atoms due to Anderson localization, *Phys. Rev. A* **103**(2), 023320 (2021).
- [149] Y. Sharabi, E. Lustig, M. Segev, Disordered Photonic Time Crystals, *Phys. Rev. Lett.* **126**(16), 163902 (2021).
- [150] K. Sacha, Anderson localization and Mott insulator phase in the time domain, *Sci. Rep.* **5**(10787), 1–6 (2015).
- [151] K. Giergiel, A. Dauphin, M. Lewenstein, J. Zakrzewski, K. Sacha, Topological time crystals, *New J. Phys.* **21**(5), 052003 (2019).
- [152] E. Lustig, Y. Sharabi, M. Segev, Topological aspects of photonic time crystals, *Optica* **5**(11), 1390–1395 (2018).
- [153] K. Giergiel, A. Kuroś, A. Kosior, K. Sacha, Inseparable Time-Crystal Geometries on the Möbius Strip, *Phys. Rev. Lett.* **127**(26), 263003 (2021).
- [154] A. J. Lichtenberg, M. A. Lieberman, *Regular and chaotic dynamics*, volume 38 (Springer Science & Business Media, 2013).
- [155] A. Buchleitner, D. Delande, J. Zakrzewski, Non-dispersive wave packets in periodically driven quantum systems, *Phys. Rep.* **368**(5), 409–547 (2002).
- [156] K. Giergiel, A. Miroszewski, K. Sacha, Time Crystal Platform: From Quasicrystal Structures in Time to Systems with Exotic Interactions, *Phys. Rev. Lett.* **120**(14), 140401 (2018).
- [157] K. Martiyanov, V. Makhalov, A. Turlapov, Observation of a Two-Dimensional Fermi Gas of Atoms, *Phys. Rev. Lett.* **105**(3), 030404 (2010).
- [158] A. Kuroś, R. Mukherjee, W. Golletz, F. Sauvage, K. Giergiel, F. Mintert, K. Sacha, Phase diagram and optimal control for n-tupling discrete time crystal, *New J. Phys.* **22**(9), 095001 (2020).
- [159] H. Miyake, G. A. Siviloglou, C. J. Kennedy, W. C. Burton, W. Ketterle, Realizing the Harper Hamiltonian with Laser-Assisted Tunneling in Optical Lattices, *Phys. Rev. Lett.* **111**(18), 185302 (2013).
- [160] Z.-A. Jia, B. Yi, R. Zhai, Y.-C. Wu, G.-C. Guo, G.-P. Guo, Quantum Neural Network States: A Brief Review of Methods and Applications, *Adv. Quantum Technol.* **2**(7-8), 1800077 (2019).
- [161] I. Goodfellow, Y. Bengio, A. Courville, *Deep Learning* (MIT Press, 2016), <http://www.deeplearningbook.org>.
- [162] M. W. Berry, A. Mohamed, B. W. Yap, *Supervised and Unsupervised Learning for Data Science* (Springer, Cham, Switzerland, 2020).

- [163] J. Carrasquilla, R. G. Melko, Machine learning phases of matter, *Nat. Phys.* **13**, 431–434 (2017).
- [164] E. P. L. van Nieuwenburg, Y.-H. Liu, S. D. Huber, Learning phase transitions by confusion, *Nat. Phys.* **13**, 435–439 (2017).
- [165] R. A. Vargas-Hernández, J. Sous, M. Berciu, R. V. Krems, Extrapolating Quantum Observables with Machine Learning: Inferring Multiple Phase Transitions from Properties of a Single Phase, *Phys. Rev. Lett.* **121**(25), 255702 (2018).
- [166] Y. Zhang, A. Mesaros, K. Fujita, S. D. Edkins, M. H. Hamidian, K. Ch’ng, H. Eisaki, S. Uchida, J. C. S. Davis, E. Khatami, E.-A. Kim, Machine learning in electronic-quantum-matter imaging experiments, *Nature* **570**, 484–490 (2019).
- [167] A. Bohrdt, C. S. Chiu, G. Ji, M. Xu, D. Greif, M. Greiner, E. Demler, F. Grusdt, M. Knap, Classifying snapshots of the doped Hubbard model with machine learning, *Nat. Phys.* **15**, 921–924 (2019).
- [168] G. Torlai, G. Mazzola, J. Carrasquilla, M. Troyer, R. Melko, G. Carleo, Neural-network quantum state tomography, *Nat. Phys.* **14**, 447–450 (2018).
- [169] Y. Levine, O. Sharir, N. Cohen, A. Shashua, Quantum Entanglement in Deep Learning Architectures, *Phys. Rev. Lett.* **122**(6), 065301 (2019).
- [170] K. Choo, G. Carleo, N. Regnault, T. Neupert, Symmetries and Many-Body Excitations with Neural-Network Quantum States, *Phys. Rev. Lett.* **121**(16), 167204 (2018).
- [171] K. Choo, T. Neupert, G. Carleo, Two-dimensional frustrated J_1 – J_2 model studied with neural network quantum states, *Phys. Rev. B* **100**(12), 125124 (2019).
- [172] F. Ferrari, F. Becca, J. Carrasquilla, Neural Gutzwiller-projected variational wave functions, *Phys. Rev. B* **100**(12), 125131 (2019).
- [173] M. Hibat-Allah, M. Ganahl, L. E. Hayward, R. G. Melko, J. Carrasquilla, Recurrent neural network wave functions, *Phys. Rev. Res.* **2**(2), 023358 (2020).
- [174] K. Choo, A. Mezzacapo, G. Carleo, Fermionic neural-network states for ab-initio electronic structure, *Nat. Commun.* **11**(2368), 1–7 (2020).
- [175] N. Astrakhantsev, T. Westerhout, A. Tiwari, K. Choo, A. Chen, M. H. Fischer, G. Carleo, T. Neupert, Broken-Symmetry Ground States of the Heisenberg Model on the Pyrochlore Lattice, *Phys. Rev. X* **11**(4), 041021 (2021).
- [176] G. Pescia, J. Han, A. Lovato, J. Lu, G. Carleo, Neural-Network Quantum States for Periodic Systems in Continuous Space, arXiv:2112.11957 (2021).

- [177] X. Gao, L.-M. Duan, Efficient representation of quantum many-body states with deep neural networks, *Nat. Commun.* **8**(662), 1–6 (2017).
- [178] L. Bottou, Large-Scale Machine Learning with Stochastic Gradient Descent, in *Proceedings of COMPSTAT'2010* (Physica-Verlag HD, 2010), 177–186.
- [179] S. Ruder, An overview of gradient descent optimization algorithms, [arXiv:1609.04747](https://arxiv.org/abs/1609.04747) (2016).
- [180] D. P. Kingma, J. Ba, Adam: A Method for Stochastic Optimization, [arXiv:1412.6980](https://arxiv.org/abs/1412.6980) (2014).
- [181] K. Sun, Z. Gu, H. Katsura, S. Das Sarma, Nearly Flatbands with Non-trivial Topology, *Phys. Rev. Lett.* **106**(23), 236803 (2011).
- [182] T. Neupert, L. Santos, C. Chamon, C. Mudry, Fractional Quantum Hall States at Zero Magnetic Field, *Phys. Rev. Lett.* **106**(23), 236804 (2011).
- [183] E. Tang, L. Fu, Strain-induced partially flat band, helical snake states and interface superconductivity in topological crystalline insulators, *Nat. Phys.* **10**(12), 964–969 (2014).
- [184] R. Mondaini, G. G. Batrouni, B. Grémaud, Pairing and superconductivity in the flat band: Creutz lattice, *Phys. Rev. B* **98**(15), 155142 (2018).
- [185] O. Derzhko, J. Richter, M. Maksymenko, Strongly correlated flat-band systems: The route from Heisenberg spins to Hubbard electrons, *Int. J. Mod. Phys B* **29**(12), 1530007 (2015).
- [186] S. Flach, D. Leykam, J. D. Bodyfelt, P. Matthies, A. S. Desyatnikov, Detangling flat bands into Fano lattices, *EPL* **105**(3), 30001 (2014).
- [187] W. Maimaiti, A. Andreanov, H. C. Park, O. Gendelman, S. Flach, Compact localized states and flat-band generators in one dimension, *Phys. Rev. B* **95**(11), 115135 (2017).
- [188] T. Zhang, G.-B. Jo, One-dimensional sawtooth and zigzag lattices for ultracold atoms, *Sci. Rep.* **5**(16044), 1–7 (2015).
- [189] V. A. J. Pyykkönen, S. Peotta, P. Fabritius, J. Mohan, T. Esslinger, P. Törmä, Flat-band transport and Josephson effect through a finite-size sawtooth lattice, *Phys. Rev. B* **103**(14), 144519 (2021).
- [190] S. Weimann, L. Morales-Inostroza, B. Real, C. Cantillano, A. Szameit, R. A. Vicencio, Transport in Sawtooth photonic lattices, *Opt. Lett.* **41**(11), 2414–2417 (2016).
- [191] F. A. An, E. J. Meier, B. Gadway, Engineering a Flux-Dependent Mobility Edge in Disordered Zigzag Chains, *Phys. Rev. X* **8**(3), 031045 (2018).
- [192] S. D. Huber, E. Altman, Bose condensation in flat bands, *Phys. Rev. B* **82**(18), 184502 (2010).

- [193] G. Carleo, K. Choo, D. Hofmann, J. E. T. Smith, T. Westerhout, F. Alet, E. J. Davis, S. Efthymiou, I. Glasser, S.-H. Lin, M. Mauri, G. Mazzola, C. B. Mendl, E. van Nieuwenburg, O. O'Reilly, H. Théveniaut, G. Torlai, F. Vicentini, A. Wietek, Netket: A machine learning toolkit for many-body quantum systems, *SoftwareX* 100311 (2019).
- [194] A. Shrestha, A. Mahmood, Review of Deep Learning Algorithms and Architectures, *IEEE Access* **7**, 53040–53065 (2019).
- [195] Y. Zong, S. Xia, L. Tang, D. Song, Y. Hu, Y. Pei, J. Su, Y. Li, Z. Chen, Observation of localized flat-band states in Kagome photonic lattices, *Opt. Express* **24**(8), 8877–8885 (2016).
- [196] C. M. Caves, C. A. Fuchs, Quantum information: How much information in a state vector?, arXiv:9601025v1 (1996).
- [197] R. Orús, A practical introduction to tensor networks: Matrix product states and projected entangled pair states, *Ann. Phys.* **349**, 117–158 (2014).
- [198] P. Degenfeld-Schonburg, M. J. Hartmann, Self-consistent projection operator theory for quantum many-body systems, *Phys. Rev. B* **89**(24), 245108 (2014).
- [199] L. Lehtovaara, J. Toivanen, J. Eloranta, Solution of time-independent Schrödinger equation by the imaginary time propagation method, *J. Comput. Phys.* **221**(1), 148–157 (2007).
- [200] S. McArdle, T. Jones, S. Endo, Y. Li, S. C. Benjamin, X. Yuan, Variational ansatz-based quantum simulation of imaginary time evolution, *npj Quantum Inf.* **5**(75), 1–6 (2019).
- [201] G. E. Hinton, R. R. Salakhutdinov, Reducing the Dimensionality of Data with Neural Networks, *Science* **313**, 504–507 (2006).
- [202] H. J. Kelley, Gradient theory of optimal flight paths, *ARS Journal* **30**(10), 947–954 (1960).
- [203] Hecht-Nielsen, Theory of the backpropagation neural network, in *International 1989 Joint Conference on Neural Networks* (IEEE, 1989), volume 1, 593–605.
- [204] F. Chollet, et al., Keras, <https://github.com/fchollet/keras> (2015).
- [205] R. Perline, Zipf's law, the central limit theorem, and the random division of the unit interval, *Phys. Rev. E* **54**(1), 220–223 (1996).

CURRICULUM VITAE

Name: Giedrius
Surname: Žlabys
Date of birth: 1992-05-18
Place of birth: Vilnius, Lithuania
E-mail: giedrius.zlabys@tfai.vu.lt

Education:

- 2007–2011 Mykolas Biržiška gymnasium, Vilnius.
- 2011–2015 Vilnius University, Faculty of Physics
Bachelor degree.
- 2015–2017 Vilnius University, Faculty of Physics
Master degree, Magna Cum Laude.
- 2017–2021 Vilnius University, Faculty of Physics,
Institute of Theoretical Physics and Astronomy,
Ph.D. studies.

International conferences and workshops:

- 2017 Quantum Optics IX, Poland.
- 2017 Synthetic dimensions in quantum engineered systems, Switzerland.
- 2018 Topological matter in artificial gauge fields, Germany.
- 2018 Les Houches predoc school on Ultracold Fermions, France.
- 2018 European tensor networks, Germany.
- 2019 Young Atom Opticians, Germany.
- 2019 Time Crystals and Related phenomena, Poland.
- 2021 Conference on Time Crystals, virtual.
- 2021 Open Readings 2021, virtual.

Work experience:

- 2013–2018 Technician at Vilnius University, Faculty of Physics,
Institute of Theoretical Physics and Astronomy.
- 2017–2021 Junior assistant in statistical physics course at Vilnius University,
Faculty of Physics, Institute of Theoretical Physics and Astronomy.
- 2018–2021 Junior researcher at Vilnius University, Faculty of Physics,
Institute of Theoretical Physics and Astronomy.

TRUMPOS ŽINIOS APIE AUTORIŲ

Vardas: Giedrius
Pavardė: Žlabys
Gimimo data: 1992-05-18
Gimimo vieta: Vilnius, Lietuva
El. paštas: giedrius.zlabys@tfai.vu.lt

Išsilavinimas:

- 2007–2011 Mykolo Biržiškos gimnazija.
- 2011–2015 Vilniaus universitetas, Fizikos fakultetas
Bakalauro kvalifikacinis laipsnis.
- 2015–2017 Vilniaus universitetas, Fizikos fakultetas
Magistro kvalifikacinis laipsnis, Magna Cum Laude.
- 2017–2021 Vilniaus universitetas, Fizikos fakultetas,
Teorinės fizikos ir astronomijos institutas,
Doktorantūra.

Tarptautinės konferencijos ir mokyklos:

- 2017 Quantum Optics IX, Lenkija.
- 2017 Synthetic dimensions in quantum engineered systems, Šveicarija.
- 2018 Topological matter in artificial gauge fields, Vokietija.
- 2018 Les Houches predoc school on Ultracold Fermions, Prancūzija.
- 2018 European tensor networks, Vokietija.
- 2019 Young Atom Opticians, Vokietija.
- 2019 Time Crystals and Related phenomena, Lenkija.
- 2021 Conference on Time Crystals, virtuali.
- 2021 Open Readings 2021, virtuali.

Profesinė veikla:

- 2013–2018 Technikas, Vilniaus universitetas, Fizikos fakultetas,
Teorinės fizikos ir astronomijos institutas.
- 2017–2021 Jaunesnysis asistentas statistinės fizikos seminaruose,
Vilniaus universitetas, Fizikos fakultetas,
Teorinės fizikos ir astronomijos institutas.
- 2018–2021 Jaunesnysis mokslo darbuotojas, Vilniaus universitetas,
Fizikos fakultetas, Teorinės fizikos ir astronomijos institutas.

NOTES

Vilnius University Press
Saulėtekio av. 9, III bld., LT-10222 Vilnius
e-mail: info@leidykla.vu.lt, www.leidykla.vu.lt
bookshop.vu.lt, journals.vu.lt
Print run copies 11